



저작자표시-비영리-변경금지 2.0 대한민국

이용자는 아래의 조건을 따르는 경우에 한하여 자유롭게

- 이 저작물을 복제, 배포, 전송, 전시, 공연 및 방송할 수 있습니다.

다음과 같은 조건을 따라야 합니다:



저작자표시. 귀하는 원저작자를 표시하여야 합니다.



비영리. 귀하는 이 저작물을 영리 목적으로 이용할 수 없습니다.



변경금지. 귀하는 이 저작물을 개작, 변형 또는 가공할 수 없습니다.

- 귀하는, 이 저작물의 재이용이나 배포의 경우, 이 저작물에 적용된 이용허락조건을 명확하게 나타내어야 합니다.
- 저작권자로부터 별도의 허가를 받으면 이러한 조건들은 적용되지 않습니다.

저작권법에 따른 이용자의 권리는 위의 내용에 의하여 영향을 받지 않습니다.

이것은 [이용허락규약\(Legal Code\)](#)을 이해하기 쉽게 요약한 것입니다.

[Disclaimer](#)

공학박사 학위논문

**Acoustic Waveform Inversion Strategy
with Horizontal Pressure Difference of
Ocean-Bottom Common-Receiver Gather**

해저면 공통 수신기모음의 압력 수평 차분을
활용한 음향파형역산 전략

2020년 8월

서울대학교 대학원
에너지시스템공학부
황 종 하

Acoustic Waveform Inversion Strategy with Horizontal Pressure Difference of Ocean- Bottom Common-Receiver Gather

해저면 공통 수신기 모음의 압력 수평 차분을 활용한
음향파형역산 전략

지도교수 민 동 주

이 논문을 공학박사학위논문으로 제출함
2020년 5월

서울대학교 대학원
공과대학 에너지시스템공학부
황 종 하

황종하의 공학박사학위논문을 인준함
2020년 6월

위 원 장 신 창 수 (인)

부위원장 민 동 주 (인)

위 원 민 기 복 (인)

위 원 김 병 엽 (인)

위 원 오 주 원 (인)

Abstract

Acoustic Waveform Inversion Strategy with Horizontal Pressure Difference of Ocean- Bottom Common-Receiver Gather

Jongha Hwang

Department of Energy Systems Engineering

The Graduate School

Seoul National University

Full waveform inversion is one of the most powerful seismic data processing techniques to image subsurface geological structures. By solving a local optimization problem that matches observed data with modeled data, the FWI reconstructs quantitative subsurface physical models. These days, FWI has been used for the characterization of hydrocarbon reservoirs. However, there are several challenges that make FWI less attractive, such as nonlinearity problem and its huge computational cost.

In this thesis, an acoustic FWI strategy is proposed that matches observed pseudo-Ax data obtained from the common-receiver gathers (CRG) of observed pressure data with modeled pseudo-Ax data obtained from the common-shot gathers (CSG) of modeled pressure data in source-receiver switched geometry. The pseudo-Ax data are the horizontal spatial differentiation of pressure data. Compared to the

classical CSG FWI that requires wave simulations twice the number of sources at each iteration, the proposed CRG-based scheme requires the number of wave simulations as twice the number of receivers at each iteration. Therefore, CRG FWI largely reduces the computational cost when the number of sources largely exceeds the number of receivers, such as ocean-bottom seismic data. In addition, due to the characteristic of weak near-offset PP and PS reflections at pseudo-Ax data, acoustic FWI with pseudo-Ax data focuses on the reconstruction of long-wavelength features of the model, therefore alleviates the nonlinearity problem of FWI.

With the synthetic and real data examples for the Volve oilfield at the North Sea, the performance enhancement of proposed acoustic FWI strategy is demonstrated. Because the number of sources is larger than the number of receivers, both the examples show that the proposed CRG-based scheme lowers the total computational cost of FWI, while resulting in reconstructed velocity model similar to that obtained from the classical CSG FWI. They also show that acoustic FWI with pseudo-Ax data constrains the update of short-wavelength features of given models and converges better to the real P-wave velocity model compared to the conventional acoustic FWI with pressure data.

Keyword: Full waveform inversion (FWI), Acoustic, Ocean-bottom seismic, Common-receiver gather (CRG), Horizontal particle acceleration

Student Number: 2016-21314

Chapter 6. Conclusions	100
References	102
Appendix A. Derivation of gradient in FWI.....	109
Appendix B. Conjugate-gradient method.....	113
Appendix C. Seismic reciprocity theorem.....	117
Appendix D. Local wavenumber of model update.....	119
Appendix E. Utilization of pseudo-Ax data in pressure-based FWI.....	122
Abstract in Korean.....	125

Figures

- Fig. 2-1.** Two-dimensional staggered-grid stencil indicating the locations of the wavefields and model parameters for acoustic and elastic wave simulations. 11
- Fig. 2-2.** (a) Schematic diagram showing the geometry of wave simulation and (b) comparison of seismic traces recorded at the receiver position (indicated by the triangle symbol in (a)): The green line shows the analytic solution and the red line shows the numerical solution with staggered-grid finite difference method (SGFDM). 12
- Fig. 2-3.** Schematic diagram showing both the modeling domain and perfectly matched layer (PML) region. Note that the damping profiles (d_x , d_z) gradually increase as they move farther from the modeling domain. ... 13
- Fig. 2-4.** Workflows showing the process of (a) conjugate-gradient (CG) method and (b) preconditioned conjugate-gradient (PCG) method. 20
- Fig. 2-5.** Schematic diagram showing the ranges of acceptable step-length for the sufficient decrease, curvature and strong Wolfe conditions. The gray solid line indicates the objective function curve and the black dashed-arrow shows the criterion of sufficient decrease condition. The curvature condition is shown with the black solid-arrows. 23
- Fig. 2-6.** Flowchart showing the process of time-frequency-domain FWI at each iteration. 26
- Fig. 3-1.** (a) OBC acquisition geometry with 240 sources (the red stars) and a single receiver (the yellow triangle) overlain on the P-wave velocity of the Marmousi-II model and (c) its source-receiver switched geometry; (b) and (d) are the common-receiver gather obtained in the acquisition geometry of (a) and the common-shot gather obtained in the source-receiver switched geometry of (c), respectively; (e) shows the difference between (b) and (d). 29

Fig. 3-2. Schematic diagrams showing the required common-shot gathers for (a) CSG FWI and (b) CRG FWI: n_s and n_r are the numbers of sources and receivers, respectively.	31
Fig. 3-3. Schematic diagrams showing the ray-paths to compute the gradients in (a) CSG FWI and (b) CRG FWI: The solid-arrows indicate the ray-paths of the incident wavefields and the dashed-arrows denote the ray-paths of the scattered wavefields; i and j denote the original source and receiver nodes, respectively, and k indicates the model perturbation node.	36
Fig. 3-4. Schematic diagrams showing the ray-paths to compute the approximate-Hessian matrices in (a) CSG FWI and (b) CRG FWI: The solid-arrows indicate the ray-paths of the incident wavefields and the dashed-arrows denote the ray-paths of the scattered wavefields; i and j denote the original source and receiver nodes, respectively, and p and q indicate the model perturbation nodes.	37
Fig. 3-5. (a) The P-wave velocity of the Marmousi-II model with 240 sources along the red-dashed line near the water surface and 40 receivers located at the ocean bottom along the yellow dotted-line. (b) A smoothed version of the Marmousi-II velocity model used for an initial model in FWI. ...	38
Fig. 3-6. The first gradients of (a) CSG FWI and (b) CRG FWI.	40
Fig. 3-7. The first approximate-Hessian matrices (only the diagonal components) of (a) CSG FWI and (b) CRG FWI.	41
Fig. 3-8. The first normalized model update directions obtained from the Gauss-Newton method: (a) CSG FWI and (b) CRG FWI.....	42
Fig. 3-9. Schematic diagrams showing the ray-paths to compute the pseudo-Hessian matrices in (a) CSG FWI and (b) CRG FWI: The solid-arrows indicate the ray-paths of the incident wavefields.	43
Fig. 3-10. The first pseudo-Hessian matrices of (a) CSG FWI and (b) CRG FWI.	44

Fig. 3-11. The first model update directions preconditioned by the pseudo-Hessian matrices: (a) CSG FWI and (b) CRG FWI.....	45
Fig. 3-12. Representative (a) common-shot gather (CSG) and (b) common-receiver gather (CRG) obtained with varying source functions for the Marmousi-II model.	48
Fig. 3-13. Inversion results for the Marmousi-II model obtained from (a) CSG FWI and (b) CRG FWI. (c) is the model difference between (a) and (b).....	49
Fig. 4-1. (a) P-wave velocity model and (b) S-wave velocity model estimated from the empirical relationships: The red star indicates the source position and the yellow dotted line shows the receiver line at the ocean-bottom.	56
Fig. 4-2. Acoustic and elastic common-shot gathers of (a) pressure, (b) horizontal and (c) vertical particle acceleration wavefields: PP and PS denote the types of reflections.	57
Fig. 4-3. Schematic diagram showing the ray-paths (the one-sided white arrows) and particle motions (the double-sided blue arrows) of PP reflections. At near offsets, PP reflections cause particle motions in an almost vertical direction.	58
Fig. 4-4. Schematic diagram showing the ray-paths (the one-sided white arrows) and particle motions (the double-sided red arrows) of PS reflections. At near offsets, PS reflections cause particle motions in an almost horizontal direction.	59
Fig. 4-5. Acoustic common-shot gather (CSG) of horizontal particle acceleration (Ax) wavefields (right panel) and elastic CSG of pseudo-Ax wavefields (left panel). Note that PS reflections are weaker at pseudo-Ax data than those at Ax data (refer to Fig. 4-2b).	60
Fig. 4-6. Sensitivity kernels for the acoustic wavefields: (a) pressure, (b) horizontal and (c) vertical particle acceleration wavefields.	63

Fig. 4-7. Sensitivity kernels for the elastic wavefields: (a) pressure, (b) horizontal (Ax) and (c) vertical particle acceleration wavefields. Compared to the case of using acoustic Ax wavefield, additional PS migration isochrone (black arrows) appears. (d) is the sensitivity kernel for pseudo-Ax data, where both the PP and PS migration isochrones appear weak.64

Fig. 4-8. Schematic diagram showing that the horizontal pressure difference with ocean-bottom topography is affected by both the horizontal and vertical particle motions: p_1 , p_3 are the pressure wavefields at the selected receiver positions, (x, z) and $(x + \Delta x, z - \Delta z)$, respectively; p_4 is the pressure wavefield at $(x, z - \Delta z)$67

Fig. 4-9. (a) P-wave velocity model for acoustic wave simulation and common-shot gathers (CSG) of (b) pressure, (c) horizontal particle acceleration and (d) horizontal pressure difference: the red-solid and yellow-dotted lines in (a) indicate the source and receiver lines, respectively; the red star in (a) shows the source position for the representative CSGs in (b, c, and d); the red circles show that near-offset PP reflections are strong at the horizontal pressure difference in the source-receiver geometry of (a).68

Fig. 4-10. Schematic diagram showing that the horizontal pressure difference in source-receiver switched geometry (CRG FWI) comes only from the horizontal particle motion: p_1 , p_3 are the pressure data at the selected receiver positions, (x, z) and $(x + \Delta x, z - \Delta z)$, respectively.69

Fig. 4-11. (a) P-wave velocity model for acoustic wave simulation and common-shot gathers (CSG) of (b) pressure, (c) horizontal particle acceleration and (d) horizontal pressure difference: the red-solid and yellow-dotted lines in (a) indicate the source and receiver lines, respectively; the red star in (a) shows the source position for the representative CSGs in (b, c, and d); the red circles show that near-offset PP reflections are weak at the horizontal pressure difference in the source-receiver geometry of (a).

.....	70
Fig. 4-12. Tomographic velocity models at the Volve oilfield of the North Sea: (a) P-wave velocity model, (b) S-wave velocity model, and (c) smoothed P-wave velocity model as an initial model for FWI; the red-dashed and yellow-dotted lines indicate the source and receiver positions, respectively.....	73
Fig. 4-13. Representative common-shot gathers of (a) pressure, (b) horizontal particle acceleration and (c) pseudo-Ax. Both the PP and PS reflections at near offsets are weak at pseudo-Ax data.	75
Fig. 4-14. The first iteration model update directions obtained from acoustic FWI with (a) pressure, (b) horizontal particle acceleration and (c) pseudo-Ax data.	76
Fig. 4-15. Inversion results obtained from acoustic FWI with (a) pressure, (b) horizontal particle acceleration and (c) pseudo-Ax data. Note that excessive updates of the reflector boundaries are observed particularly near the depth of 3 km in (a) compared to (c).	77
Fig. 4-16. Model error curves for acoustic FWI with pressure and pseudo-Ax data.	78
Fig. 4-17. Radiation pattern analysis with (a) pressure data and (b) second-order horizontal differentiation of pressure data: The black star denotes the source position and white rectangles represent the velocity perturbation points; the widths of black arrows show the relative amplitude of scattered wavefields.	80
Fig. 5-1. The location of Volve oilfield at North Sea.	83
Fig. 5-2. Source-receiver geometries of selected receiver cable of OBC data acquired at Volve oilfield of North Sea. The black line indicates the target receiver cable (No. 40195-1252860) and the gray dots show the plane view of all applied source positions related to this receiver cable.	

For 2D FWI, only the seismic traces whose source positions are located along this receiver cable line are selected and used.84

Fig. 5-3. P-wave velocity model of the survey area obtained from the reflection tomography. Geological information of survey area is given by Jackson and Lewis (2016).85

Fig. 5-4. Representative common-shot gathers of (a) pressure, (b) horizontal particle acceleration and (c) pseudo-Ax data.86

Fig. 5-5. Representative common-receiver gathers of (a) pressure and (b) pseudo-Ax data.87

Fig. 5-6. Model update directions at the first iteration when using (a, d) pressure, (b) horizontal particle acceleration and (c, e) pseudo-Ax data in (a, b, c) CSG FWI and (d, e) CRG FWI.89

Fig. 5-7. Inverted P-wave velocity models obtained from acoustic FWI with (a, d) pressure, (b) horizontal particle acceleration and (c, e) pseudo-Ax data in (a, b, c) CSG FWI and (d, e) CRG FWI.91

Fig. 5-8. Migration images for the P-wave velocity models inverted using (a) pressure data (Fig. 5-7d) and (b) pseudo-Ax data (Fig. 5-7e).96

Fig. 5-9. Inverted P-wave velocity models overlapped with the migration images: (a) pressure data inversion (Fig. 5-7d) and (b) pseudo-Ax data inversion (Fig.5-7e).97

Fig. 5-10. Modeled and observed pressure CSGs for the P-wave velocity models inverted using (a) pressure data (Fig. 5-7d) and (b) pseudo-Ax data (Fig. 5-7e): The red circles indicate that the far-offset PP reflection better matches in case of pseudo-Ax data inversion compared to the case of pressure data inversion; note that modeled CSGs are horizontally flipped.98

Fig. 5-11. Angle-domain common-image gathers (ADCIG) for the P-wave velocity

models inverted using (a) pressure data (Fig. 5-7d) and (b) pseudo-Ax data (Fig. 5-7e): The red arrows show that reflectors appear to be more flattened when using the velocity of pseudo-Ax data inversion compared to those when using the velocity of pressure data inversion.99

Fig. D-1. Schematic diagram showing the geometry of source and receiver wavefields: The red arrows are related to the source wavefields and the orange arrows are related to the receiver wavefields; the blue arrow shows the slowness vector of the gradient.121

Tables

Table 3-1. Modeling parameters for synthetic data for the Marmousi-II model.....	39
Table 3-2. Comparison of computation time per iteration for CSG FWI (T_{CSG}) and CRG FWI (T_{CRG}) in the time-frequency domain for P-wave velocity of Marmousi-II model: ns and nr indicate the number of sources and receivers, respectively.	50
Table 4-1. Modeling parameters for synthetic data for Volve oilfield tomographic velocity models.	74
Table 5-1. Comparison of computational time per iteration for CSG FWI (T_{CSG}) and CRG FWI (T_{CRG}) in the time-frequency domain for real data example of the Volve oilfield: ns and nr indicate the number of sources and receivers, respectively.....	93

Chapter 1. Introduction

1.1. Background of the study

Seismic exploration is one of the key techniques in discovering the oil and gas deposits due to its remarkable ability to describe and map subsurface boundaries. During the seismic exploration, seismic signals generated from source positions are transmitted through subsurface media and recorded at receivers carrying information of subsurface structures and physical properties. Accordingly, various seismic imaging techniques, such as tomography (Wu and Toksoz, 1987; Woodward, 1992), migration (Claerbout and Doherty, 1972; Schneider, 1978; Gazdag, 1978; Stolt, 1978) and inversion, have been developed and applied to extract this subsurface information from recorded seismic traces. Among these techniques, full waveform inversion (FWI; Lailly, 1983; Tarantola; 1984; Pratt et al., 1998; Virieux and Operto, 2009) uses full waveforms of seismic data and solves a local optimization problem of matching observed and modeled seismic data to reconstruct quantitative subsurface physical models with the resolution up to half the local wavelength (Virieux and Operto, 2009). These days, FWI has been an important seismic data processing step in reservoir exploration.

The majority of recent studies on FWI in literature have been devoted to resolving the challenges that make FWI less attractive. One of the main challenges in FWI is the nonlinearity of objective function with respect to the model parameter perturbations. Due to this nonlinearity, FWI often gets stuck into the local minima and fails to reconstruct reliable subsurface physical models. Several methods have been proposed to mitigate this nonlinearity problem of FWI. Bunks et al. (1995) proposed a multiscale strategy that sequentially increases the frequency range of data in FWI. Shin and Cha (2008; 2009) introduced Laplace-

domain and Laplace-Fourier-domain waveform inversion to utilize extremely low-frequency data components in FWI to obtain an appropriate starting model. Xu et al. (2012) and Wu and Alkalifah (2015) applied reflection waveform inversion (RWI) to smoothly update deeper parts of models using the rabbit-ear shaped kernels, and Ramos-Martinez et al. (2016; 2019) used dynamic weighting technique to constrain the update of short-wavelength features related to the migration isochrones. All these methods, however, share the same concept to mitigate the nonlinearity problem. The concept is that long-wavelength, smooth features of the model should be reconstructed in the early iterations of FWI to guide objective function close to the global minimum.

Another challenge of FWI is its excessive computational cost, particularly for large-scale problems. To reduce the computational burden of FWI, the encoded simultaneous-source method (Krebs et al., 2009; Symes 2010; Ben-Hadj-Ali et al., 2011; Jeong et al., 2013), which matches encoded common-shot gathers (CSG) with modeled CSGs from simultaneously encoded source signatures, and plane-wave approach (Vigh and Starr, 2008; Tao and Sen, 2013; Kwon et al., 2015), which matches observed and modeled plane-wave gathers originated from the time-delayed multiple sources, have been proposed. Unlike the classical CSG-based FWI that requires wave simulations as twice the number of utilized sources to compute local descent directions in each iteration (Gauthier et al., 1986), the encoded simultaneous-source and plane-wave approaches reduce the number of wave simulations to the number of encoded source pairs and to the number of ray parameters, respectively, which plays a role in speeding up FWI.

Using the acoustic approximation for FWI of marine seismic data is also a method of alleviating both the challenges. Because the nonlinearity problem becomes severe and the computational cost of wave simulation tends to increase as

more types of physical parameters are considered and the nature of wave propagation becomes complex, acoustic FWI has been widely used in the industry, despite the elastic and anisotropic nature of the Earth. Accordingly, enhancing the performance of acoustic FWI remains to be an important issue and several studies have been recently introduced for this purpose. Agudo et al. (2018; 2020) used the matching filter technique to transform the elastic data into the acoustic data and successfully resulted in better resolved P-wave velocity model by mitigating the elastic effects of the recorded seismic data. However, their approach needs additional elastic wave simulations based on the rough estimate of V_p/V_s ratio, therefore the computational cost increases compared to conventional acoustic FWI. Additionally, Akrami (2017) and Zhong and Liu (2019) proposed vector-acoustic FWI that simultaneously uses all pressure and particle velocity wavefields recorded at the ocean-bottom to use the full directivity and dynamic information contained in data. With synthetic data examples, their method seems to yield inverted velocity models with higher resolution compared to the conventional acoustic FWI. However, because this approach uses all different types of wavefields at the same time, it has limitations to be applied to field data where the qualities of recorded pressure and particle acceleration data might differ and amplitude relationships between those data components could be destroyed during the preprocessing stage (Szydlik et al., 2007).

1.2. Research Objective

In this thesis, an inversion strategy is proposed to enhance the performance of acoustic FWI in the aspects of mitigating the nonlinearity and reducing the computational burden, particularly for ocean-bottom seismic data. These days, in marine seismic exploration, data acquisition at the ocean-bottom through ocean-bottom cable (OBC), ocean-bottom node (OBN) or ocean-bottom seismometer (OBS), has been common due to its several advantages over the conventional streamer system, such as easier acquisition of far-offset data, direct recording of PS reflections and flexibility in designing a survey. However, because increasing the number of airgun sources near the ocean surface is easier and cheaper than increasing the number of deployed receivers at the ocean bottom, ocean-bottom seismic data often contain numerous sources with the limited number of receivers. Due to the large number of sources, the classical CSG-based FWI of ocean-bottom data requires huge computational cost if all recorded seismic traces are used in inversion. Therefore, a strategy to reduce the computational cost of FWI for ocean-bottom seismic data is required.

Based on the seismic reciprocity theorem, an inversion scheme is proposed that matches common-receiver gathers (CRG) of observed data with CSGs of modeled data obtained in the source-receiver switched geometry. This approach is referred to as CRG FWI. Following this approach, the number of wave simulations in each iteration reduces to twice the number of receivers, which is usually much smaller than the number of sources for ocean-bottom seismic data. Because the computational cost of wave simulation takes up most of the computation burden in FWI, this approach has the potential to speed up FWI, proportional to the ratio between the numbers of sources and receivers.

Additionally, to mitigate the nonlinearity problem, an acoustic FWI strategy

that uses horizontal spatial difference of pressure data rather than pressure data themselves is proposed. The horizontal spatial differentiation of pressure data is referred to as the pseudo-Ax data. Because PP and PS reflections at small reflection angles have extremely small amplitudes at pseudo-Ax data compared to those at pressure and horizontal particle acceleration (Ax) data, the acoustic FWI with pseudo-Ax data helps reconstruct long-wavelength features of the given models. Finally, both the approaches for acoustic FWI of ocean-bottom seismic data are combined and enhanced performance of this proposed strategy is demonstrated with synthetic and real data examples.

1.3. Outline

This thesis is organized as follows: In chapter 2, the nature of wave propagation is briefly reviewed and the methods of numerical wave simulation and local optimization for FWI are explained. Then, in chapter 3, the seismic reciprocity theorem and the concept of CRG FWI are discussed. Comparing inversion results and computational time of the proposed CRG FWI to those of the classical CSG FWI, it is demonstrated that CRG FWI reconstructs subsurface velocity models preserving the quality, but with less computational cost. In chapter 4, the acoustic FWI strategy of matching modeled and observed pseudo-Ax data rather than pressure data is proposed. Characteristics of each type of wavefield are analyzed by investigating their CSGs and sensitivity kernels, and the effect of using pseudo-Ax data in acoustic FWI is shown with synthetic data example. Finally, both the approaches are combined to reconstruct long-wavelength features of the velocity model and to achieve computational speed-up in acoustic FWI. In chapter 5, the enhanced performance of proposed strategy is demonstrated with real data set acquired at the Volve oilfield of the North Sea.

Chapter 2. Methodology

2.1. Forward wave simulation

The two-dimensional acoustic wave equation is formulated using the Newton's equation of motion and stress-strain relationship as follows:

$$\rho \mathbf{a}(\mathbf{x}, t) = \nabla P(\mathbf{x}, t) \quad , \quad (1)$$

$$\frac{1}{\rho v_p^2} \frac{\partial^2 P(\mathbf{x}, t)}{\partial t^2} = \nabla \cdot \mathbf{a}(\mathbf{x}, t) \quad , \quad (2)$$

where P is the pressure wavefield and $\mathbf{a} = (a_x, a_z)$ is the particle acceleration wavefield; v_p and ρ are the P-wave velocity and density parameters, respectively; $\mathbf{x} = (x, z)$ and t stand for the location vector and time, respectively.

Similarly, the two-dimensional elastic wave equation is formulated as follows:

$$\begin{cases} \rho a_x(\mathbf{x}, t) = \frac{\partial \tau_{xx}(\mathbf{x}, t)}{\partial x} + \frac{\partial \tau_{xz}(\mathbf{x}, t)}{\partial z} \\ \rho a_z(\mathbf{x}, t) = \frac{\partial \tau_{zz}(\mathbf{x}, t)}{\partial z} + \frac{\partial \tau_{xz}(\mathbf{x}, t)}{\partial x} \end{cases} \quad , \quad (3)$$

$$\begin{cases} \frac{1}{\rho} \frac{\partial^2 \tau_{xx}(\mathbf{x}, t)}{\partial t^2} = v_p^2 \frac{\partial a_x(\mathbf{x}, t)}{\partial x} + (v_p^2 - 2v_s^2) \frac{\partial a_z(\mathbf{x}, t)}{\partial z} \\ \frac{1}{\rho} \frac{\partial^2 \tau_{zz}(\mathbf{x}, t)}{\partial t^2} = v_p^2 \frac{\partial a_z(\mathbf{x}, t)}{\partial z} + (v_p^2 - 2v_s^2) \frac{\partial a_x(\mathbf{x}, t)}{\partial x} \\ \frac{1}{\rho} \frac{\partial^2 \tau_{xz}(\mathbf{x}, t)}{\partial t^2} = v_s^2 \left(\frac{\partial a_x(\mathbf{x}, t)}{\partial z} + \frac{\partial a_z(\mathbf{x}, t)}{\partial x} \right) \end{cases} \quad , \quad (4)$$

where τ_{xx} and τ_{zz} indicate the normal stresses in horizontal and vertical

directions, respectively; and τ_{xz} is the shear stress and v_s is the S-wave velocity. In this thesis, the elastic wave equation is used to synthesize observed elastic wavefields at fluid-solid coupled media and the average of normal stresses at each nodal point corresponds to pressure wavefield.

The staggered-grid finite-difference method (SGFDM; Virieux, 1986; Levander, 1988; Graves, 1996) is employed to numerically simulate the wave propagation. Rather than directly solving a second-order differential wave equation, SGFDM uses the first-order differential wave equations expressed in eqs. (1) to (4). Because the centered finite-difference scheme is used to approximate the differential operators in space, the staggered-grid stencil as shown in Fig. 2-1 is needed. Compared to the conventional finite-difference method (FDM), SGFDM is easy to apply the fourth-order accurate scheme in space, therefore requires a smaller number of grids per wavelength to satisfy the same degree of numerical dispersion (Levander, 1988). In addition, wave propagation through the coupled media is easily simulated with SGFDM because this scheme does not need any additional boundary condition for the fluid-solid interface. Fig. 2-2b shows the comparison of seismic traces, one from the analytic solution of Ewing et al. (1957) and the other from the numerical simulation with SGFDM in the source-receiver geometry of Fig. 2-2a (Choi, 2007). Just by setting the S-wave velocity to be zero for the water layer, the SGFDM properly simulates the wave propagation through the coupled media.

Additionally, an absorbing boundary condition is needed for numerical wave simulation to remove spurious reflections occurring at the outer boundaries of the computational domain. One of the most widely used techniques to suppress these spurious reflections is the perfectly matched layer (PML; Berenger, 1994; Collino and Tsogka, 2001), which gradually damps the wavefields inside the PML region

by stretching the space variable into the complex domain as:

$$\begin{aligned}\tilde{x} &= x - \frac{i}{\omega} \int_0^x d_x(s) ds \\ \tilde{z} &= z - \frac{i}{\omega} \int_0^z d_z(s) ds\end{aligned}, \quad (5)$$

where \tilde{x} and \tilde{z} are the new space variables defined in the complex domain; ω is the angular frequency and d_x and d_z are the damping profiles that have zero values inside the modeling domain and gradually increase inside the PML region as shown in Fig. 2-3. In case of 1D harmonic wave with this new space variable,

$$A \exp\left(-i\left(k_x \tilde{x} - \omega t\right)\right) = A \exp\left(-i\left(k_x x - \omega t\right)\right) \exp\left(-\frac{k_x}{\omega} \int d_x(s) ds\right), \quad (6)$$

it is noticed that the complex part of the space variable plays a role in decaying the wavefields. To implement the PML boundary condition, the space differential operator is changed as:

$$\frac{\partial}{\partial \tilde{x}} = \frac{i\omega}{i\omega + d_x} \frac{\partial}{\partial x} = \frac{1}{s_x} \frac{\partial}{\partial x}. \quad (7)$$

Eq. (7) notated in the frequency domain is changed into the time domain as follows:

$$\frac{\partial}{\partial \tilde{x}} = F^{-1} \left(\frac{1}{s_x} \right) * \frac{\partial}{\partial x} = \frac{\partial}{\partial x} - d_x H(t) \exp(-d_x t) * \frac{\partial}{\partial x} = \frac{\partial}{\partial x} + \varphi_x, \quad (8)$$

where H is the Heaviside unit step function and $*$ stands for the convolution operator in time. Following Komatitsch and Martin (2007), there is a recursive relationship for φ_x as:

$$\varphi_x^{n+1} = \exp(-d_x \Delta t) \varphi_x^n + (\exp(-d_x \Delta t) - 1) \left(\frac{\partial}{\partial x} \right)^{n+1/2}. \quad (9)$$

Therefore, PML is easily implemented along with time-domain SGFDM just by changing the spatial differential operator as in eq. (8) and introducing a memory variable for φ_x to be updated by eq. (9) at each time step.

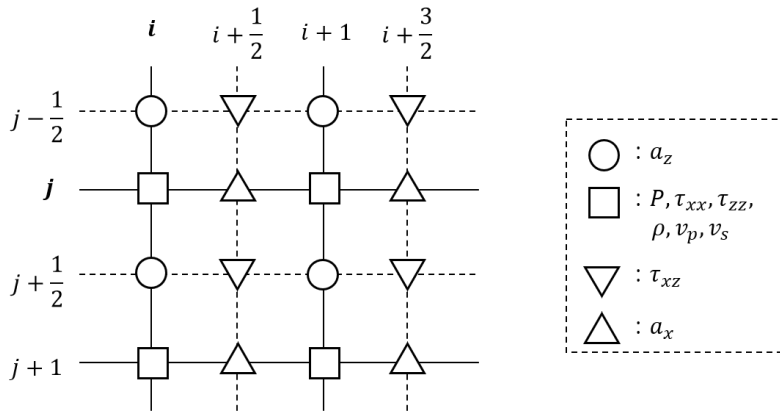


Fig. 2-1. Two-dimensional staggered-grid stencil indicating the locations of the wavefields and model parameters for acoustic and elastic wave simulations.

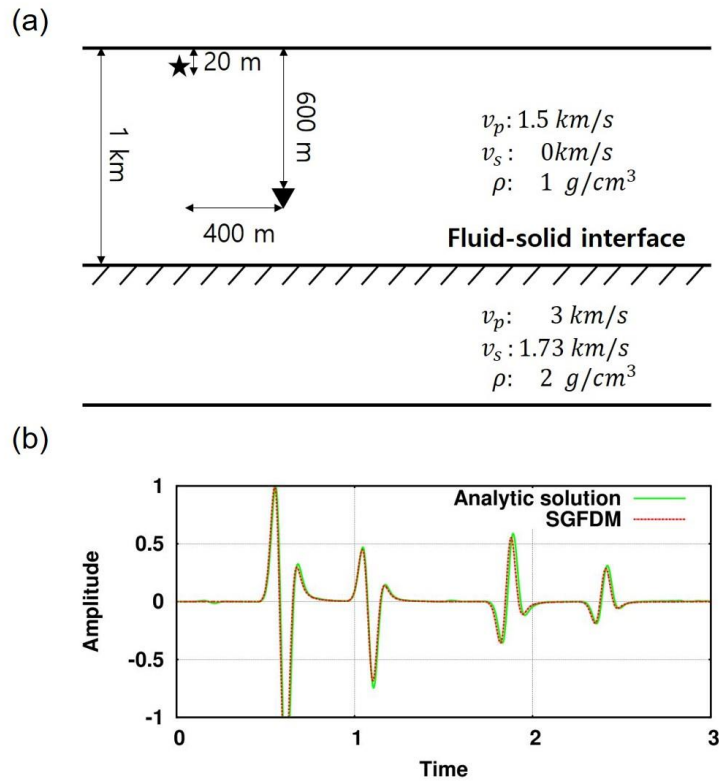


Fig. 2-2. (a) Schematic diagram showing the geometry of wave simulation and (b) comparison of seismic traces recorded at the receiver position (indicated by the triangle symbol in (a)): The green line shows the analytic solution and the red line shows the numerical solution with staggered-grid finite difference method (SGFDM).

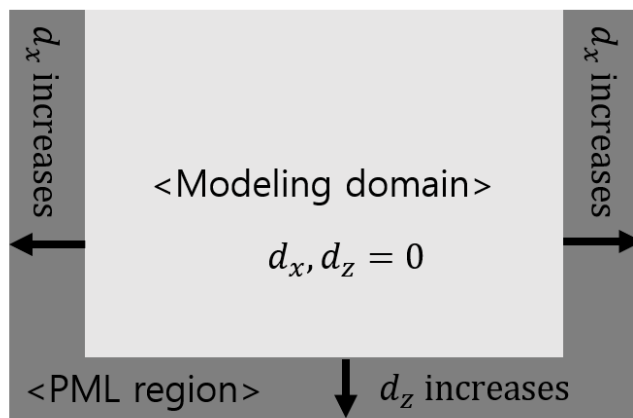


Fig. 2-3. Schematic diagram showing both the modeling domain and perfectly matched layer (PML) region. Note that the damping profiles (d_x , d_z) gradually increase as they move farther from the modeling domain.

2.2. Inverse problem

FWI solves a local optimization problem of matching modeled and observed data to reconstruct reliable subsurface physical models. Therefore, for FWI, we first need to define an objective function to be minimized. One of the most widely used objective functions is based on the least-squares (l_2) norm of data residual (Tarantola, 1984; Pratt et al., 1998) as:

$$E_{L2} = \sum_{i=1}^{ns} \sum_{j=1}^{nr} \frac{1}{2} \left\| \mathbf{p}_u(\mathbf{x}_j; \mathbf{x}_i) - \mathbf{p}_d(\mathbf{x}_j; \mathbf{x}_i) \right\|_2^2, \quad (10)$$

where \mathbf{p}_u and \mathbf{p}_d indicate the time-series of modeled and observed wavefields, respectively; \mathbf{x}_i and \mathbf{x}_j are the source and receiver location vectors, respectively; ns and nr indicate the number of sources and receivers, respectively. By taking the partial derivative with respect to the model parameter vector (\mathbf{m}) at the k^{th} nodal point, local ascent direction of the objective function is calculated as:

$$\nabla_{m_k} E_{L2} = \sum_{i=1}^{ns} \sum_{j=1}^{nr} \frac{\partial \mathbf{p}_u(\mathbf{x}_j; \mathbf{x}_i)}{\partial m_k} \cdot \left(\mathbf{p}_u(\mathbf{x}_j; \mathbf{x}_i) - \mathbf{p}_d(\mathbf{x}_j; \mathbf{x}_i) \right). \quad (11)$$

However, because the explicit calculation of partial derivative wavefield ($\partial \mathbf{p}_u / \partial \mathbf{m}_k$) is computationally heavy, the adjoint-state method is commonly used (Lailly, 1983; Tarantola, 1984; Plessix, 2006). Following the adjoint-state method, eq. (11) is rearranged as:

$$\nabla_{m_k} E_{L2} = \sum_{i=1}^{ns} \sum_{j=1}^{nr} \frac{\partial S_{kk}}{\partial m_k} \mathbf{p}_u(\mathbf{x}_k; \mathbf{x}_i) \cdot \boldsymbol{\lambda}^-(\mathbf{x}_k; \mathbf{x}_i), \quad (12)$$

where \mathbf{S} is the modeling operator matrix, λ indicates the time-series of adjoint wavefield, and the superscript $-$ indicates the sequence of array backward in time. The adjoint wavefield is calculated from the following adjoint-state equation (refer to Appendix A):

$$\left(\frac{1}{\rho v_p^2} \frac{\partial^2}{\partial t^2} - \nabla \cdot \frac{1}{\rho} \nabla \right) \lambda(\mathbf{x}, t) = \sum_{j=1}^{nr} \left(p_u(\mathbf{x}_j, T-t; \mathbf{x}_i) - p_d(\mathbf{x}_j, T-t; \mathbf{x}_i) \right), \quad (13)$$

where T indicates the total recording time. Then, with this local gradient direction, model parameters are iteratively updated to minimize the objective function following the steepest-descent method.

However, because the least-squares norm matches both the amplitudes and phases of modeled and observed waveforms, highly accurate information of source signature is essential. To avoid estimating accurate source signatures during FWI, different types of objective functions have been proposed. One of them is the global-correlation-norm objective function (Routh et al., 2011; Choi and Alkhalifah, 2012), which is defined as:

$$E_{GC} = \sum_{i=1}^{ns} \sum_{j=1}^{nr} \hat{\mathbf{p}}_u(\mathbf{x}_j; \mathbf{x}_i) \hat{\mathbf{p}}_d(\mathbf{x}_j; \mathbf{x}_i), \quad (14)$$

where the hat notation indicates the normalized vector as $\hat{\mathbf{p}} = \mathbf{p} / \|\mathbf{p}\|$. By taking the partial derivative with respect to the model parameter, eq. (14) is written as:

$$\nabla_{m_k} E_{GC} = \sum_{i=1}^{ns} \sum_{j=1}^{nr} \frac{\partial \hat{\mathbf{p}}_u(\mathbf{x}_j; \mathbf{x}_i)}{\partial m_k} \cdot \frac{B \hat{\mathbf{p}}_u(\mathbf{x}_j; \mathbf{x}_i) - \hat{\mathbf{p}}_d(\mathbf{x}_j; \mathbf{x}_i)}{\|\hat{\mathbf{p}}_u(\mathbf{x}_j; \mathbf{x}_i)\|}, \quad (15)$$

where $B = \hat{\mathbf{p}}_u(\mathbf{x}_j; \mathbf{x}_i) \cdot \hat{\mathbf{p}}_d(\mathbf{x}_j; \mathbf{x}_i)$. Compared to the gradient of least-squares

objective function in eq. (11), the only difference occurs in the residual term. Therefore, just by changing the data residual term as in eq. (15) during the calculation of adjoint wavefields, FWI with the global-correlation-norm objective function is easily performed. As addressed by Choi and Alkhalifah (2012), this global-correlation norm is theoretically the same as the least-squares norm of the normalized wavefields. Accordingly, FWI with the global-correlation norm is insensitive to the source amplitude difference between the modeled and observed data and thus behaves similar to the phase inversion.

2.3. Conjugate-gradient method

Several local optimization methods, such as the Gauss-Newton, Quasi-Newton and conjugate-gradient methods, are used rather than the steepest-descent method to enhance the convergence of FWI. Throughout the thesis, the preconditioned conjugate gradient (PCG) method with the pseudo-Hessian matrix (Shin et al., 2001a) preconditioner is used as a local optimization method of FWI.

The conjugate gradient (CG) method is a type of conjugate direction method (Nocedal and Wright, 1999) that was originally developed to solve a large linear system of equations. Because the CG method automatically generates a linearly independent set of solution vectors, n-dimensional linear system can be solved in at most n iterations. These days, the CG method is also used to solve the nonlinear optimization problem, such as FWI, following the work of Fletcher and Reeves (1964). In this chapter, I only focus on the application of CG method in FWI and a detailed explanation of the CG method is shown in Appendix B.

The purpose of FWI is to seek the model parameters that minimize the objective function, and therefore, mathematically expressed as:

$$\min_{\mathbf{m}} E(\mathbf{m}) . \quad (16)$$

Using the second-order Taylor series, the objective function is written as:

$$\begin{aligned} E(\mathbf{m}) &= E(\mathbf{m}_0 + \Delta\mathbf{m}) \\ &\cong E(\mathbf{m}_0) + \nabla_{\mathbf{m}} E(\mathbf{m}_0)^T \Delta\mathbf{m} + \frac{1}{2} \Delta\mathbf{m}^T \mathbf{H} \Delta\mathbf{m} , \end{aligned} \quad (17)$$

where \mathbf{m} and \mathbf{m}_0 indicate the true and initial model parameter vectors, respectively; $\mathbf{H} = \nabla_{\mathbf{m}} (\nabla_{\mathbf{m}} E(\mathbf{m}_0))$ is the Hessian matrix and $\mathbf{m} - \mathbf{m}_0 =$

$\Delta \mathbf{m} = \sum_{i=1}^{niter} \alpha_i \Delta \mathbf{m}_i$ is the model update vector where α_i and $\Delta \mathbf{m}_i$ are the step-length and model update direction at each iteration, respectively; *niter* denotes the total number of iterations. Notice that this approximation makes sense only when the initial model is sufficiently close to the true model (local optimization). Because the objective function has the minimum value at the true model, the minimization problem in eq. (16) is changed into a linear system as follows:

$$\nabla_{\mathbf{m}} E(\mathbf{m}) = 0 = \nabla_{\mathbf{m}} E(\mathbf{m}_0) + \mathbf{H}(\mathbf{m} - \mathbf{m}_0) , \quad (18)$$

$$\mathbf{Hm} = \mathbf{Hm}_0 - \nabla_{\mathbf{m}} E(\mathbf{m}_0) = \mathbf{b} . \quad (19)$$

To solve eq. (19) with the CG method (refer to Appendix B), the model update directions at each iteration are defined as a linear combination of the previous model update direction and the current residue vector as:

$$\Delta \mathbf{m}_k = \mathbf{r}_k + \beta_k \Delta \mathbf{m}_{k-1} , \quad (20)$$

where $\mathbf{r}_k = \mathbf{b} - \mathbf{Hm}_k$ is the residue vector of current iteration and

$\beta_k = \frac{(\mathbf{r}_k - \mathbf{r}_{k-1})^T \mathbf{r}_k}{\mathbf{r}_{k-1}^T \mathbf{r}_{k-1}}$ following the study of Polak and Ribiere (1969). Due to the

following relationship between the gradient and Hessian matrix,

$$-\nabla_{\mathbf{m}} E(\mathbf{m}_k) = \mathbf{H}(\mathbf{m} - \mathbf{m}_k) = \mathbf{b} - \mathbf{Hm}_k , \quad (21)$$

it is noticed that the residue vector corresponds to the local descent direction. In FWI, the CG method is applied just by linearly combining the previous and current local descent directions with an appropriate coefficient. Fig. 2-4a shows the workflow of computing the model update directions using the CG method. To accelerate the convergence of the CG method, preconditioners whose inverse are a

rough estimate of the Hessian matrix are often used. This is referred to as the PCG method and Fig. 2-4b shows the workflow of the PCG method. For FWI with PCG method, either the inverse of pseudo-Hessian (Shin et al., 2001a) matrix or the inverse of approximate-Hessian (Shin et al., 2001b) matrix is often used as a preconditioner.

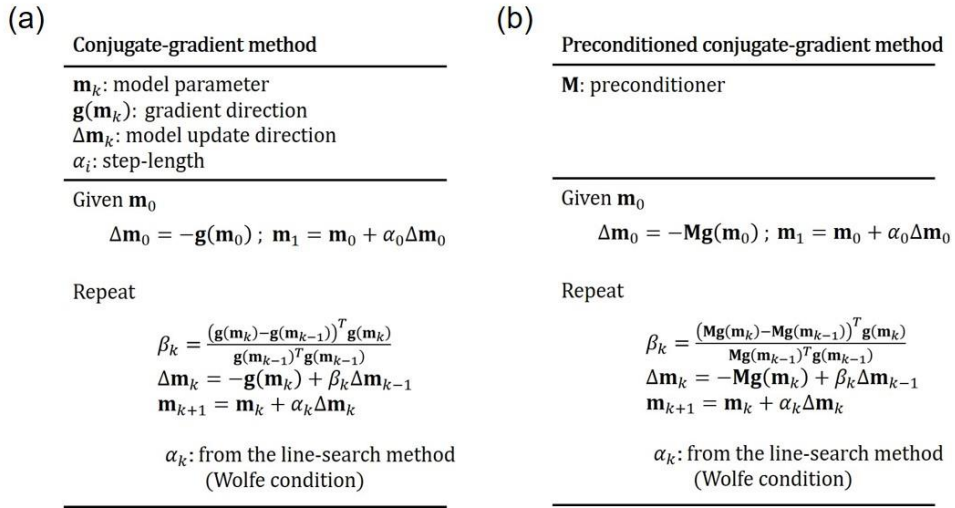


Fig. 2-4. Workflows showing the process of (a) conjugate-gradient (CG) method and (b) preconditioned conjugate-gradient (PCG) method.

2.4. Step-length calculation

Until now, the method to obtain the model update direction that minimizes the objective function is explained. For a proper update of the model parameters, a step-length which determines how much the model parameters are updated should be decided. Among the various conditions used for the determination of step-length, the strong Wolfe condition that consists of the sufficient decrease and curvature conditions (Nocedal and Wright, 1999) is employed.

The sufficient decrease condition is written as follows:

$$E(\mathbf{m}_k + \alpha_k \Delta \mathbf{m}_k) \leq E(\mathbf{m}_k) - c_1 \alpha_k \nabla_{\mathbf{m}} E(\mathbf{m}_k) \cdot \Delta \mathbf{m}_k \quad , \quad (22)$$

meaning that the step-length should be determined to satisfy a sufficiently smaller objective function value compared to the previous one. c_1 is an arbitrary coefficient in the range from 0 to 1 and the term $\nabla_{\mathbf{m}} E(\mathbf{m}_k) \cdot \Delta \mathbf{m}_k$ indicates the slope of the objective function at \mathbf{m}_k . With this condition, the optimization process will iteratively make reasonable progress. However, only with this condition, all sufficiently small α_k are accepted as a step-length and FWI may require a large number of iterations until it meets the convergence criterion. To exclude extremely small step-length, the strong Wolfe condition contains a curvature condition written as:

$$|\nabla_{\mathbf{m}} E(\mathbf{m}_k + \alpha_k \Delta \mathbf{m}_k) \cdot \Delta \mathbf{m}_k| \leq c_2 |\nabla_{\mathbf{m}} E(\mathbf{m}_k) \cdot \Delta \mathbf{m}_k| \quad , \quad (23)$$

where c_2 is also an arbitrary coefficient in the range from 0 to 1. Schematic diagram of Fig. 2-5 shows the ranges of acceptable step-length of the sufficient decrease, curvature and strong Wolfe conditions.

To determine the step-length with the strong Wolfe condition, the total range of possible step-length needs to be set as $(\alpha_{\min}, \alpha_{\max})$. Then, the trial step-length is the median value in this range as $\alpha^* = (\alpha_{\max} - \alpha_{\min})/2$ and four different cases would exist for this trial step-length.

- (i) The strong Wolfe condition is satisfied.
- (ii) The sufficient decrease condition is violated.
- (iii) The curvature condition is violated when the slope at trial step-length is positive.
- (iv) The curvature condition is violated when the slope at trial step-length is negative.

If the strong Wolfe condition is satisfied (i), then the trial step-length is used as the current iteration step-length. If the sufficient decrease condition is violated (ii) or the curvature condition is violated with positive slope (iii), step-length is recalculated within the range of $(\alpha_{\min}, \alpha^*)$. If the curvature condition is violated with negative slope (iv), step-length is recalculated within the range of $(\alpha^*, \alpha_{\max})$. Additionally, FWI terminates when the calculated step-length becomes smaller than a given threshold.

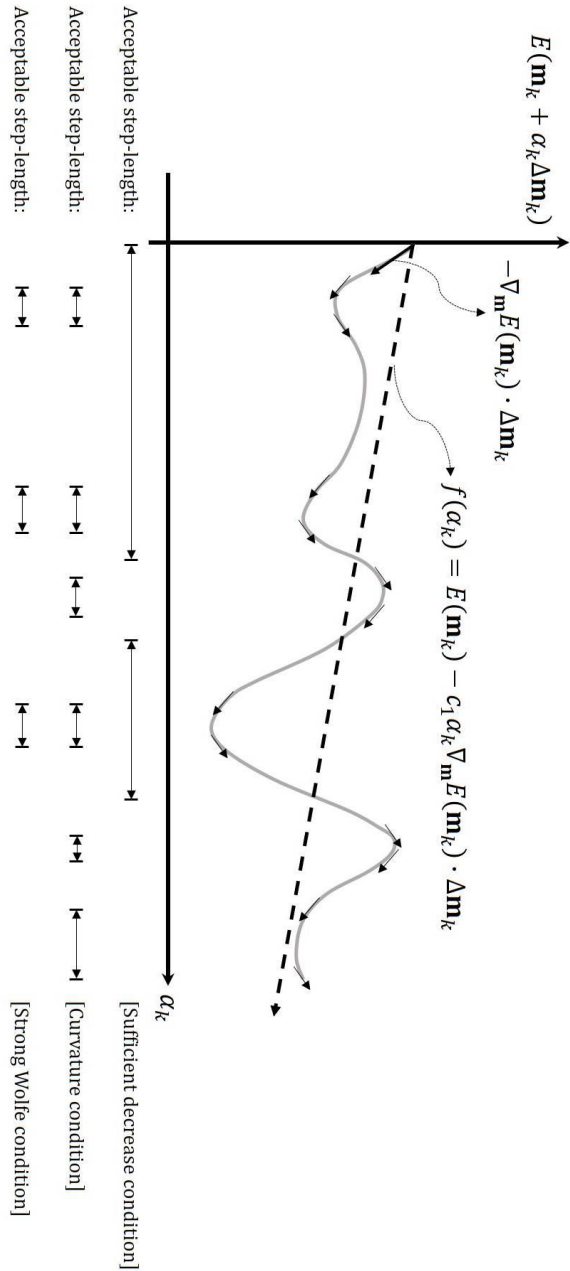


Fig. 2-5. Schematic diagram showing the ranges of acceptable step-length for the sufficient decrease, curvature and strong Wolfe conditions. The gray solid line indicates the objective function curve and the black dashed-arrow shows the criterion of sufficient decrease condition. The curvature condition is shown with the black solid-arrows.

2.5. Time-frequency-domain FWI

In seismic exploration, the early studies on FWI have been mainly performed in the time domain due to its computational convenience of wave simulations (Lailly, 1983; Tarantola, 1984; Gauthier et al., 1986; Mora, 1987; Pica et al., 1990). However, to perform convolution between the source and adjoint wavefields for the calculation of gradient, massive computer memory is required to store full information of source wavefields at each time step. The boundary saving technique (Gauthier et al., 1986) has been proposed to avoid this massive storage of wavefields, but its computational cost increases due to the reconstruction of wavefields from the boundaries.

In the 1990s, frequency-domain FWI using the direct matrix solver has been proposed by Pratt and his colleagues (Pratt, 1990; Pratt & Worthington, 1990; Pratt et al., 1998; Pratt, 1999). Because only the wavefields at selected frequencies are used for the calculation of gradients, smaller storage space is needed to store wavefields. In addition, by storing the LU factors of modeling operator matrix, frequency-domain FWI requires only a single matrix decomposition for the whole source position and greatly enhances the computational efficiency of FWI. However, for large-scale problems, frequency-domain FWI using the direct solver appears to be challenging because it requires too much memory to store the LU factors of the modeling operator matrix (Operto et al., 2007; Plessix, 2009).

In this study, to avoid the drawbacks of time- and frequency-domain FWI, time-frequency-domain FWI is performed, where wave simulations are conducted in the time domain and the gradients are calculated in the frequency domain by extracting certain frequency components of the wavefields with the discrete Laplace-Fourier-transform (Sirgue et al., 2008; Jun, 2014; Butzer, 2015; Oh and

Alkhalifah, 2018; Oh and Alkhalifah, 2019). Due to the time-domain wave simulation, which uses smaller computer memory than frequency-domain wave simulation, time-frequency-domain FWI can handle large-scale problems. Additionally, because the gradients are calculated in the frequency domain, only the selected frequency components of the wavefields need to be stored in time-frequency-domain FWI. Moreover, because the gradients at each frequency are explicitly obtained in time-frequency-domain FWI, the frequency-marching approach (Bunks et al., 1995) is easily implemented. Fig. 2-6 shows the process of time-frequency-domain FWI at each iteration.

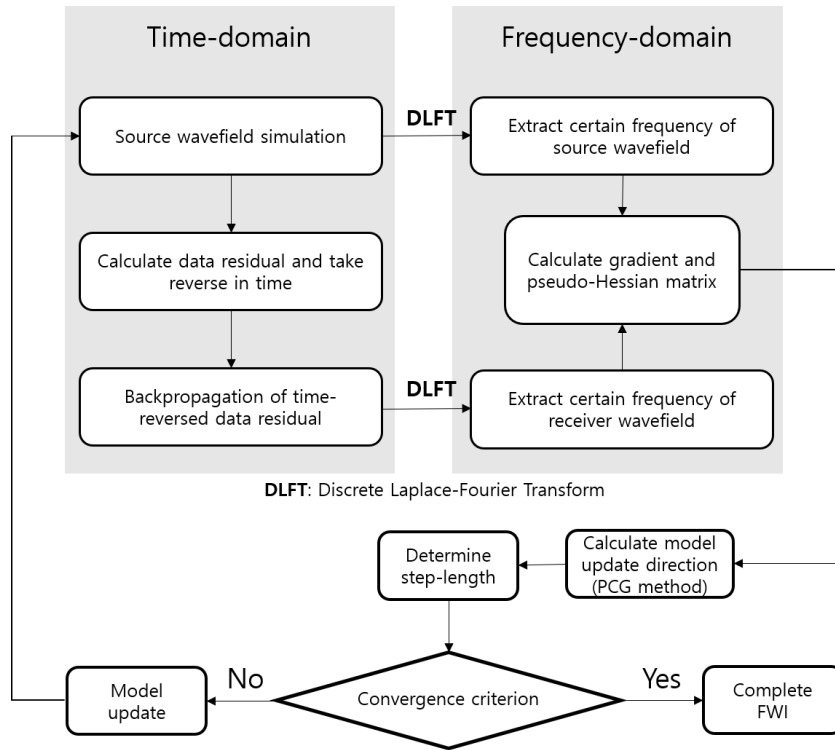


Fig. 2-6. Flowchart showing the process of time-frequency-domain FWI at each iteration.

Chapter 3. CRG-based FWI

CRG-based FWI was described in the study of Hwang et al. (2020a). In this chapter, I explain the concept of CRG FWI and prove that CRG FWI and classical CSG FWI share the same inversion results when using the Gauss-Newton method. Additionally, even in the case of using the pseudo-Hessian matrices as the preconditioners, the inversion results obtained from CRG-based scheme have small difference with those obtained from the classical CSG FWI, while greatly reducing the computational cost. This is demonstrated by implementing both the CSG FWI and CRG FWI for synthetic data for the Marmousi-II model.

3.1. The concept of CRG FWI

According to the seismic reciprocity theorem, interchange of source and receiver locations does not alter the recorded seismic traces (Knopoff and Gangi 1959; Ikelle and Amundsen 2005). This is easily shown using the Helmholtz-type acoustic wave equation (refer to Appendix C). Here, the equivalence of seismic wavefields between the CRG and CSG of source-receiver switched geometry is shown. Based on the Marmousi-II model (Martin et al. 2002), Fig. 3-1a shows a simplified geometry for OBC survey, where sources are located near the water surface and a single receiver is located in the middle of the ocean-bottom. By applying the same source signature at the whole source position, a CRG as shown in Fig. 3-1b is obtained. Figs. 3-1c and 3-1d show the source-receiver switched geometry and a CSG obtained in this switched geometry, respectively. Comparison of Figs. 3-1b and 3-1d demonstrates that CRGs of OBC survey data can be regarded as CSGs in the source-receiver switched geometry (refer to Fig. 3-1e).

Based on this observation, a CRG-based scheme, which matches observed CRG of OBC data with the modeled CSG in source-receiver switched geometry, is proposed. Compared to the classical CSG-based scheme, the number of wave simulations needed to compute the gradients at each iteration reduces to twice the number of receivers in CRG FWI. For instance, assuming a seismic survey whose numbers of sources and receivers are n_s and n_r , respectively, the classical CSG-based scheme needs CSGs with the number of n_s (each CSG consists of n_r traces) while the proposed CRG-based scheme needs CSGs with the number of n_r (each CSG consists of n_s traces) in source-receiver switched geometry (refer to Fig. 3-2). This contributes to greatly reducing the computational cost of FWI, particularly for ocean-bottom seismic data where the number of receivers is much smaller than the number of sources. It is expected that the computational speed-up of CRG FWI to CSG FWI would be n_s/n_r .

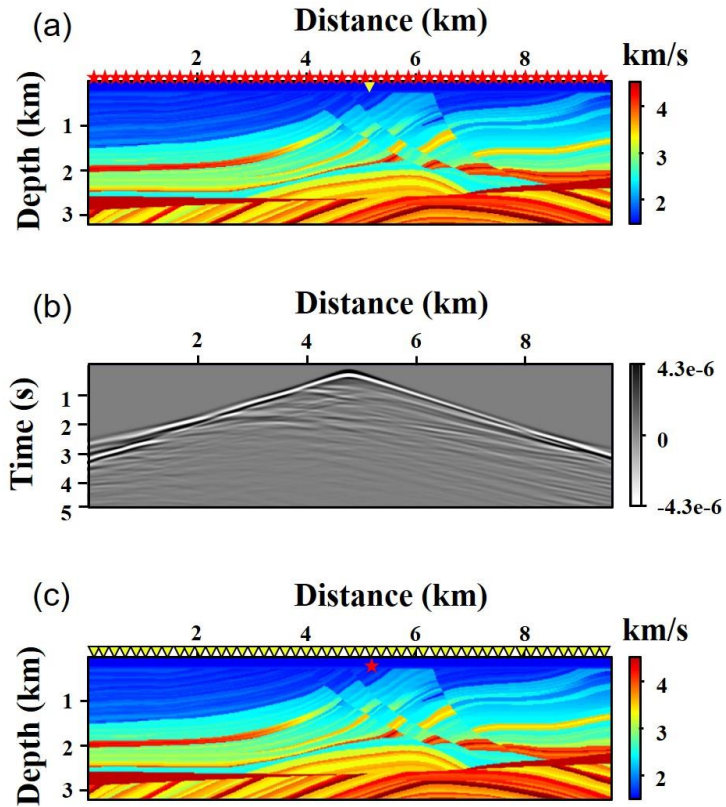


Fig. 3-1. (a) OBC acquisition geometry with 240 sources (the red stars) and a single receiver (the yellow triangle) overlain on the P-wave velocity of the Marmousi-II model and (c) its source-receiver switched geometry; (b) and (d) are the common-receiver gather obtained in the acquisition geometry of (a) and the common-shot gather obtained in the source-receiver switched geometry of (c), respectively; (e) shows the difference between (b) and (d).

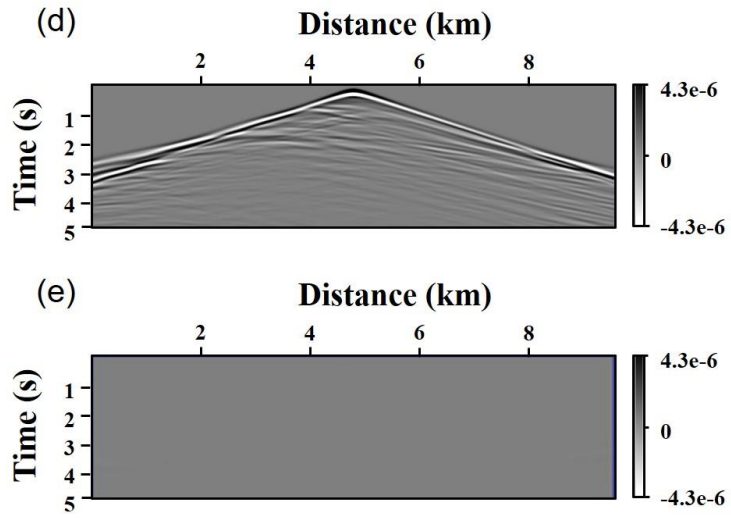


Fig. 3-1. (Continued)

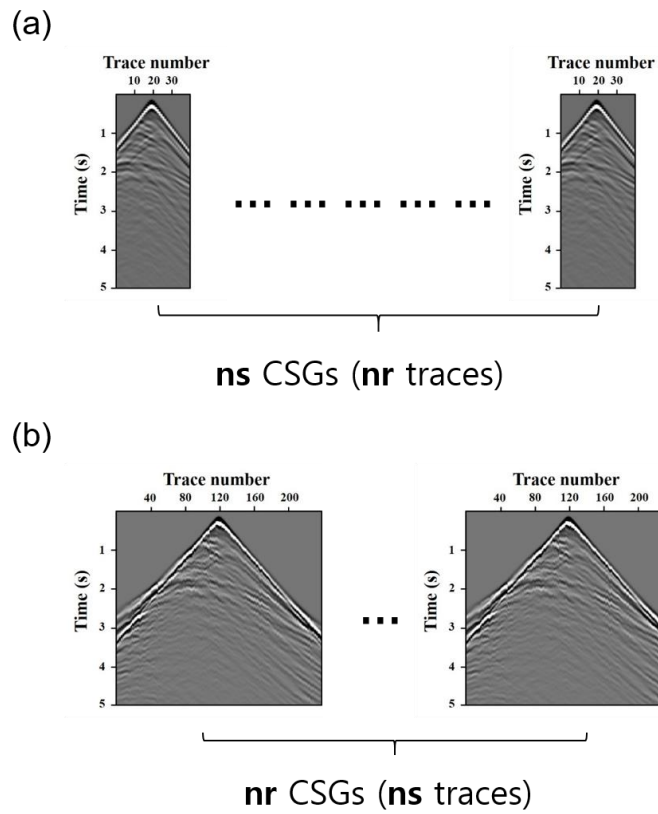


Fig. 3-2. Schematic diagrams showing the required common-shot gathers for (a) CSG FWI and (b) CRG FWI: ns and nr are the numbers of sources and receivers, respectively.

3.2. Comparison of CRG FWI with CSG FWI

Before using the CRG-based scheme in FWI, it is important to know whether this scheme offers similar inversion result to that obtained from the classical CSG-based FWI. The local gradient of the least-squares objective function with respect to a single model perturbation at the k^{th} nodal point has been derived in eq. (11) with the classical CSG-based scheme. The term $\mathbf{p}_d(\mathbf{x}_j; \mathbf{x}_i)$ for the whole receiver position (\mathbf{x}_j) denotes the observed CSG for the i^{th} source and $\frac{\partial \mathbf{p}_u(\mathbf{x}_j; \mathbf{x}_i)}{\partial m_k}$ indicates the partial derivative wavefield propagated from the i^{th} source to the j^{th} receiver due to the model parameter perturbation at the k^{th} nodal point as shown in Fig. 3-3a.

On the other hand, because observed CRG is matched with modeled CSG of the source-receiver switched geometry in CRG FWI, the gradient is calculated as follows:

$$\nabla_{m_k} E_{L2}^{CRG} = \sum_{j=1}^{nr} \sum_{i=1}^{ns} \frac{\partial \mathbf{p}_u(\mathbf{x}_i; \mathbf{x}_j)}{\partial m_k} \cdot (\mathbf{p}_u(\mathbf{x}_i; \mathbf{x}_j) - \mathbf{p}_d(\mathbf{x}_j; \mathbf{x}_i)) . \quad (24)$$

Therefore, observed seismic traces are sorted to form CRG and sources are applied at the original receiver positions during the forward wave simulation. $\frac{\partial \mathbf{p}_u(\mathbf{x}_i; \mathbf{x}_j)}{\partial m_k}$

is the partial derivative wavefield in the source-receiver switched geometry that propagates from the j^{th} source to the i^{th} receiver due to the model parameter perturbation at the k^{th} nodal point as shown in Fig. 3-3b. According to the

seismic reciprocity theorem, $\mathbf{p}_u(\mathbf{x}_i; \mathbf{x}_j) = \mathbf{p}_u(\mathbf{x}_j; \mathbf{x}_i)$ and $\frac{\partial \mathbf{p}_u(\mathbf{x}_i; \mathbf{x}_j)}{\partial m_k} = \frac{\partial \mathbf{p}_u(\mathbf{x}_j; \mathbf{x}_i)}{\partial m_k}$ when the same source signature is used for wave simulation.

Therefore, eq. (24) becomes identical to eq. (11). Furthermore, the approximate-Hessian matrices in each scheme are written as follows:

$$(\mathbf{H}_a)_{p,q}^{\text{CSG}} = \sum_{i=1}^{ns} \sum_{j=1}^{nr} \frac{\partial \mathbf{p}_u(\mathbf{x}_j; \mathbf{x}_i)}{\partial \mathbf{m}_p} \cdot \frac{\partial \mathbf{p}_u(\mathbf{x}_j; \mathbf{x}_i)}{\partial \mathbf{m}_q}, \quad (25)$$

$$(\mathbf{H}_a)_{p,q}^{\text{CRG}} = \sum_{j=1}^{nr} \sum_{i=1}^{ns} \frac{\partial \mathbf{p}_u(\mathbf{x}_i; \mathbf{x}_j)}{\partial \mathbf{m}_p} \cdot \frac{\partial \mathbf{p}_u(\mathbf{x}_i; \mathbf{x}_j)}{\partial \mathbf{m}_q}. \quad (26)$$

Fig. 3-4 describes the full ray-paths of approximate-Hessian matrices in both the CSG FWI and CRG FWI. For both the schemes, it is noticed that they share the same ray-path, therefore they are the same.

Fig. 3-5 shows the P-wave velocity of the Marmousi-II model and the initial velocity model used for the inversion test of CRG FWI. Modeling parameters used to synthesize the acoustic pressure data are shown in Table 3-1. Figs. 3-6, 3-7 and 3-8 are the gradients, diagonal components of the approximate-Hessian matrices and model update directions calculated at the first iteration, respectively. Because the gradients and approximate-Hessian matrices of CRG FWI and CSG FWI are identical, respectively, the model update directions calculated from the gradients and approximate-Hessian matrices will also be the same for both the schemes. However, when using the approximate-Hessian matrices as the preconditioners, the total computational costs of CRG FWI and CSG FWI are identical because additional number of wave simulations, which is twice the number of receivers (for CRG FWI, twice the number of sources), is needed during the calculation of

approximate-Hessian matrices (Shin et al., 2001b).

To reduce this cost, the pseudo-Hessian matrix (Shin et al., 2001a) is used as a preconditioner. However, in case of using the pseudo-Hessian matrix as a preconditioner, the resulting model update directions of CSG FWI and CRG FWI are different from each other. This is because only the virtual source term, which is related to the incident wavefield from the source to the perturbation point (Fig. 3-9), is considered during the calculation of the pseudo-Hessian matrix. This means that the virtual sources in CSG FWI and CRG FWI represent the incident and scattered wavefields (i.e., incident wavefields in the source-receiver switched geometry), respectively. Accordingly, the pseudo-Hessian matrices in CSG FWI and CRG FWI approximate the approximate-Hessian matrix in different ways. As shown in Figs. 3-10 and 3-11, the pseudo-Hessian matrix and the gradient preconditioned with the pseudo-Hessian matrix in CSG FWI are different from those of CRG FWI. Comparing Figs. 3-11a and 3-11b with Figs. 3-8a and 3-8b, it is observed that the model update direction preconditioned by the pseudo-Hessian matrix in CRG FWI (Fig. 3-11b) looks more similar to the directions preconditioned by the approximate-Hessian matrix (Figs. 3-8a or 3-8b) compared to the direction preconditioned by the pseudo-Hessian matrix in CSG FWI (Fig. 3-11a). This is attributed to the common geometry of OBC survey whose receivers are deployed covering a limited area compared to sources. Based on this geometry, the approximate-Hessian matrices that account for the whole raypath from source to receiver show large value near the receivers due to the dense raypath around the receivers (Figs. 3-7a and 3-7b) and become more similar to the pseudo-Hessian matrix in CRG FWI (Fig. 3-10b) that also has large value near the receivers. Note that this does not mean that the pseudo-Hessian matrix of CRG FWI is a more accurate approximation of the approximate-Hessian matrix than that of CSG FWI. However, these results support that the pseudo-Hessian matrix in CRG FWI is still

a reasonable approximation of the Hessian matrix, therefore CRG FWI would result in a reconstructed velocity model whose quality is as good as the classical CSG FWI even if the pseudo-Hessian matrix is used as a preconditioner.

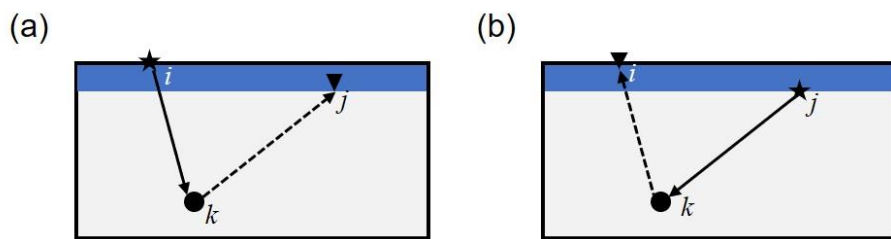


Fig. 3-3. Schematic diagrams showing the ray-paths to compute the gradients in (a) CSG FWI and (b) CRG FWI: The solid-arrows indicate the ray-paths of the incident wavefields and the dashed-arrows denote the ray-paths of the scattered wavefields; i and j denote the original source and receiver nodes, respectively, and k indicates the model perturbation node.

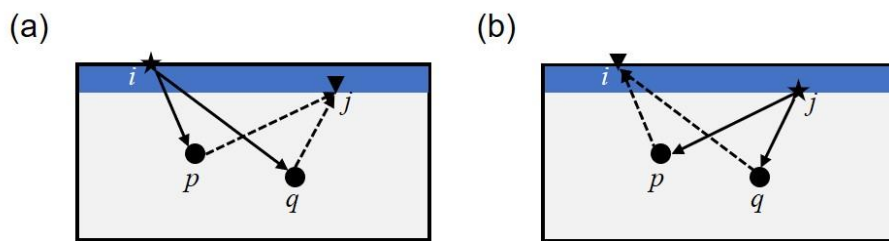


Fig. 3-4. Schematic diagrams showing the ray-paths to compute the approximate-Hessian matrices in (a) CSG FWI and (b) CRG FWI: The solid-arrows indicate the ray-paths of the incident wavefields and the dashed-arrows denote the ray-paths of the scattered wavefields; i and j denote the original source and receiver nodes, respectively, and p and q indicate the model perturbation nodes.

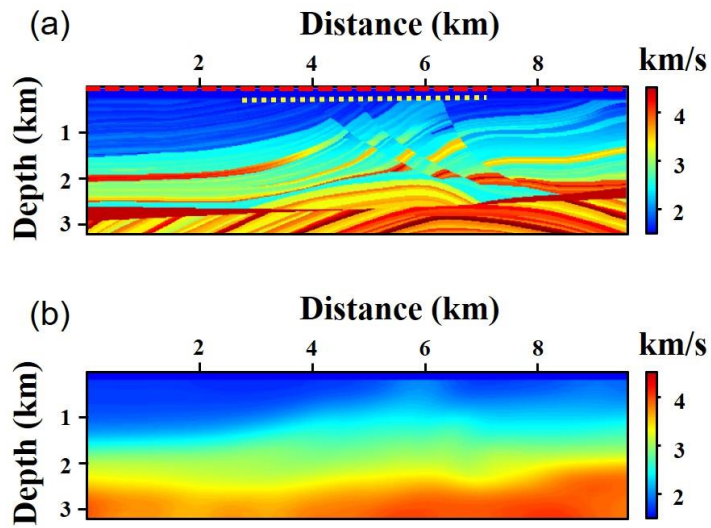


Fig. 3-5. (a) The P-wave velocity of the Marmousi-II model with 240 sources along the red-dashed line near the water surface and 40 receivers located at the ocean bottom along the yellow dotted-line. (b) A smoothed version of the Marmousi-II velocity model used for an initial model in FWI.

Table 3-1. Modeling parameters for synthetic data for the Marmousi-II model.

Model	
Size	9.6 km x 3.2 km
Grid interval	0.02 km
Source	
Wavelet	The first derivative of Gaussian function (maximum frequency of 12 Hz)
Total number	240
Interval	0.04 km
Receiver	
Total number	40
Interval	0.1 km
Depth	0.18 km

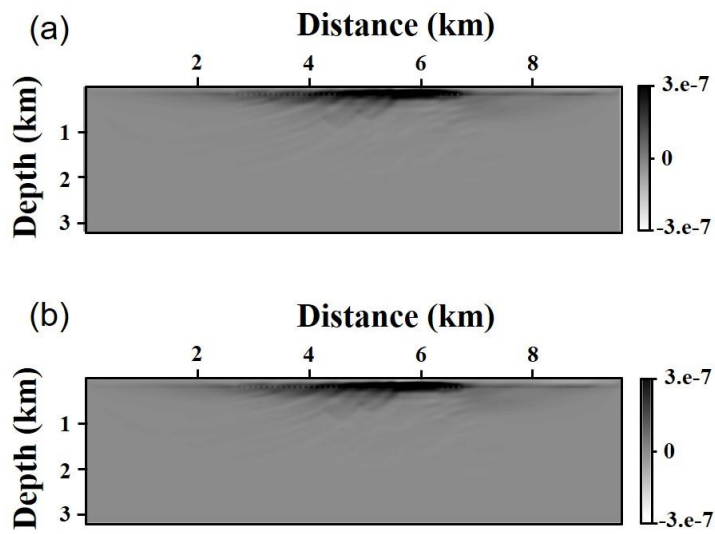


Fig. 3-6. The first gradients of (a) CSG FWI and (b) CRG FWI.

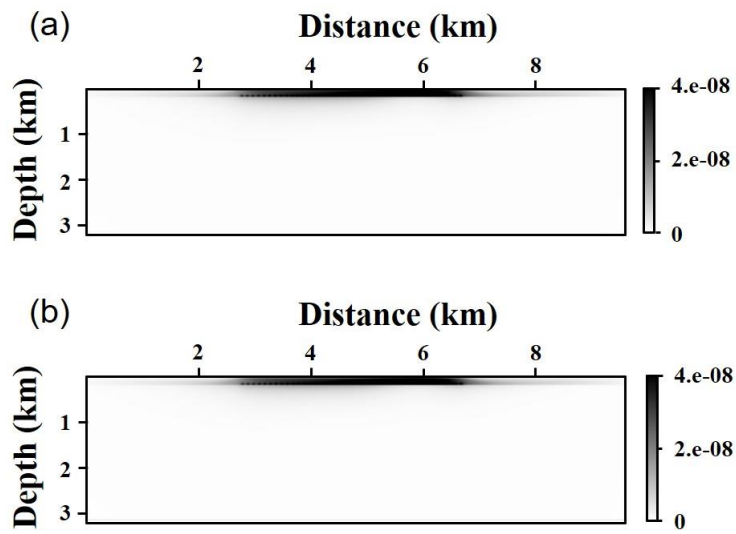


Fig. 3-7. The first approximate-Hessian matrices (only the diagonal components) of (a) CSG FWI and (b) CRG FWI.

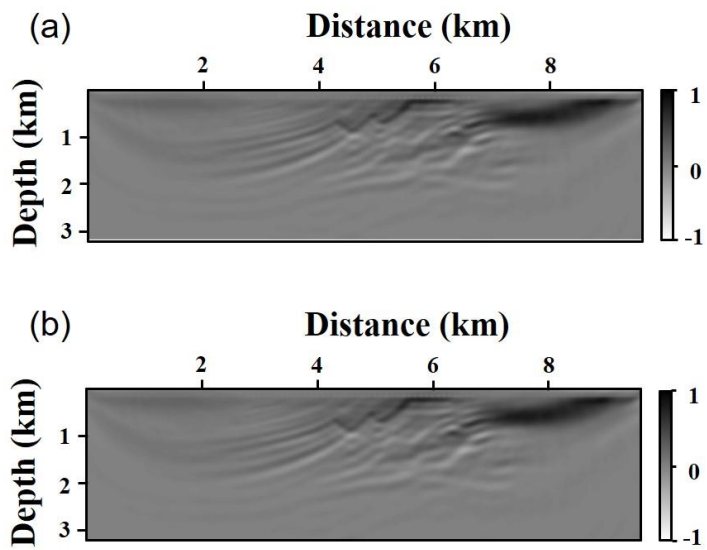


Fig. 3-8. The first normalized model update directions obtained from the Gauss-Newton method: (a) CSG FWI and (b) CRG FWI.

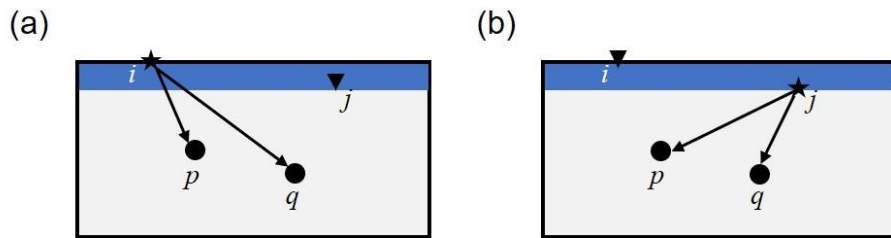


Fig. 3-9. Schematic diagrams showing the ray-paths to compute the pseudo-Hessian matrices in (a) CSG FWI and (b) CRG FWI: The solid-arrows indicate the ray-paths of the incident wavefields.

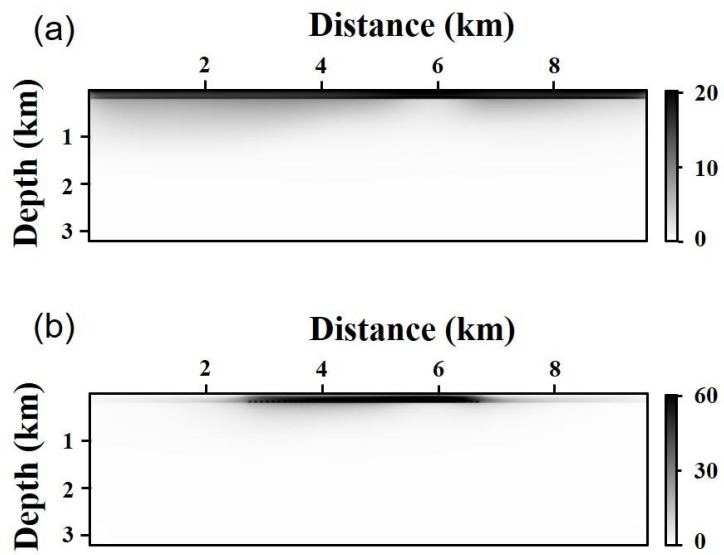


Fig. 3-10. The first pseudo-Hessian matrices of (a) CSG FWI and (b) CRG FWI.

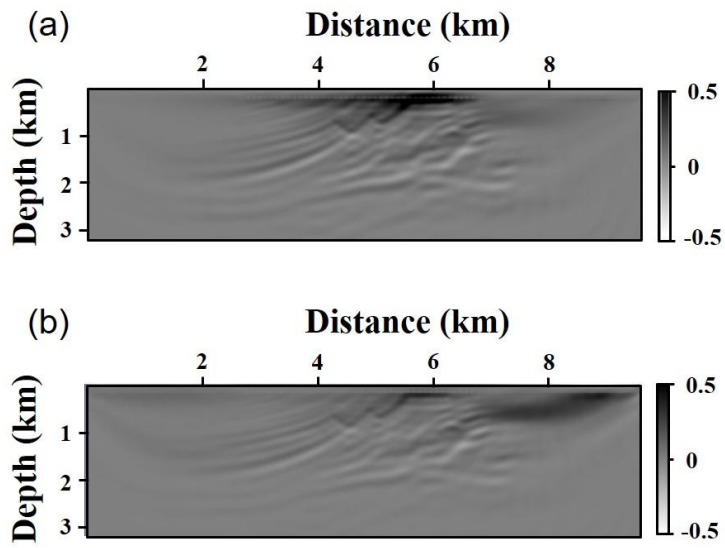


Fig. 3-11. The first model update directions preconditioned by the pseudo-Hessian matrices: (a) CSG FWI and (b) CRG FWI.

3.3. Synthetic data example: Marmousi-II model

For further investigation of CRG FWI, the synthetic pressure data obtained by assuming the OBC acquisition geometry for the P-wave velocity of the Marmousi-II model (refer to source and receiver positions in Fig. 3-5a and modeling parameters in Table 3-1) are used. Unlike the previous examples of comparing the gradients, approximate-Hessian matrices and pseudo-Hessian matrices of CSG FWI and CRG FWI, slightly different source wavelets over the source positions are applied. This is because the phase and amplitude of source wavelet may slightly change over the source positions during the seismic acquisition (Badiéy et al., 2002). Accordingly, the first derivative of Gaussian function, whose amplitude and maximum frequency change from 0.2 to 1 and 12 Hz to 14 Hz, respectively, is used for source wavelets. A representative CSG and CRG are displayed in Fig. 3-12. Due to the differences in source wavelets from one source position to another, the representative CRG in Fig. 3-12b shows some discontinuity from trace to trace unlike the CSG in Fig. 3-12a.

For time-frequency-domain FWI, the data components at frequencies from 2 Hz to 8.8 Hz with an interval of 0.4 Hz are used. Fig. 3-13 shows inversion results obtained from CSG FWI and CRG FWI. Comparing these inversion results, it is observed that some differences exist at the sides of the model (i.e., the part beyond the receiver locations). This is attributed to the differences in the pseudo-Hessian matrices used in CSG FWI and CRG FWI. However, by focusing within the horizontal range where the receivers cover, the inversion results obtained by CSG FWI and CRG FWI seem to show similar inverted structures (refer to Fig. 3-13c). Additionally, Table 3-2 shows the comparison of computational time between CSG FWI and CRG FWI when a single CPU is used to conduct a single iteration. Because the wave simulations are the most computationally intensive process

during FWI, CSG FWI that requires the number of wave simulations as twice the number of sources would require more computational time than CRG FWI, proportional to the ratio between the number of sources and receivers. Therefore, for ocean-bottom seismic data where the number of sources is commonly larger than the number of receivers, it is noticed that the CRG-based FWI achieves enhanced computational efficiency and similar inversion result compared to the classical CSG-based scheme.

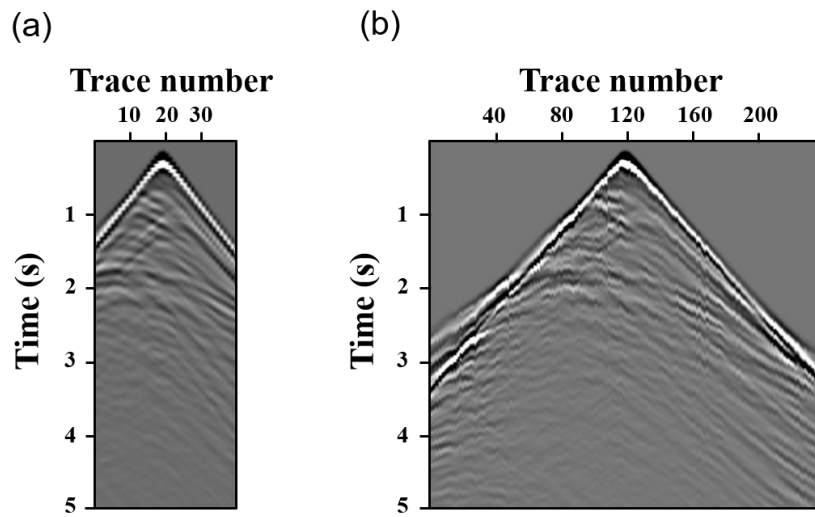


Fig. 3-12. Representative (a) common-shot gather (CSG) and (b) common-receiver gather (CRG) obtained with varying source functions for the Marmousi-II model.

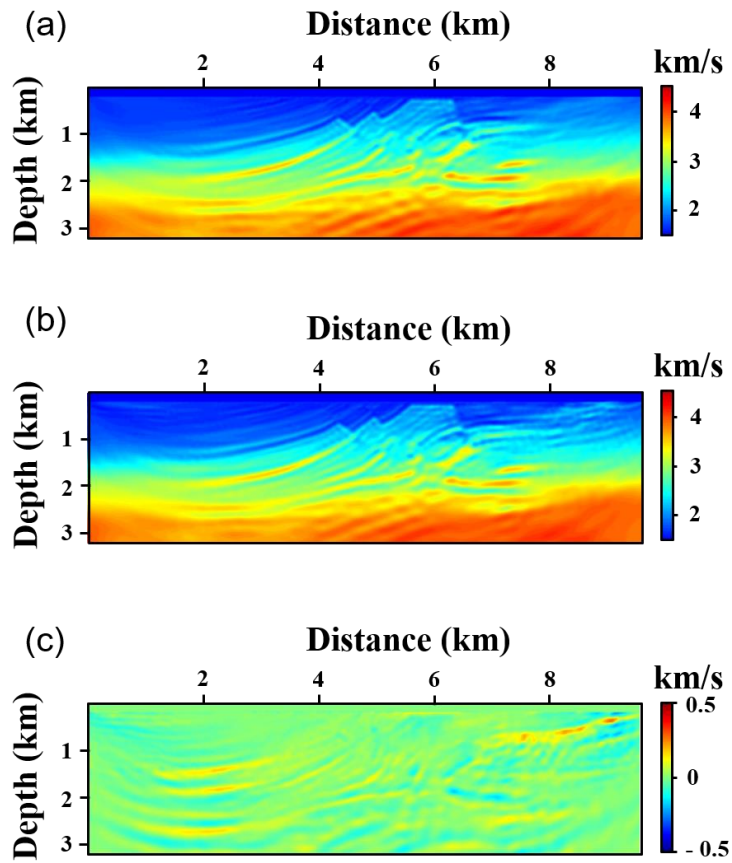


Fig. 3-13. Inversion results for the Marmousi-II model obtained from (a) CSG FWI and (b) CRG FWI. (c) is the model difference between (a) and (b).

Table 3-2. Comparison of computation time per iteration for CSG FWI (T_{CSG}) and CRG FWI (T_{CRG}) in the time-frequency domain for P-wave velocity of Marmousi-II model: ns and nr indicate the number of sources and receivers, respectively.

T_{CSG} (sec)	T_{CRG} (sec)	$T_{\text{CSG}} / T_{\text{CRG}}$	$\frac{ns}{nr}$
68542.5	11309.6	6.06	6

3.4. Discussions

In this thesis, the CSG FWI is compared with the CRG FWI only in the time-frequency domain, but the proposed CRG-based scheme can also speed up FWI in the frequency domain when using the direct solver (Hwang et al., 2020a). Although the frequency-domain FWI with the direct solver requires only a single matrix decomposition for all source positions, the forward and backward substitutions by twice the number of sources and frequencies are still needed to calculate the gradients at each iteration of CSG FWI. Therefore, using CRG as the observed data can speed up FWI even in the frequency domain due to the reduced number of forward and backward substitutions. For the same case, frequency-domain CRG FWI was about 4 times faster (less than the time reduction ratio of time-frequency-domain FWI) than frequency-domain CSG FWI.

In the synthetic inversion test, the model update directions are preconditioned with the pseudo-Hessian matrices, which are one of the simplest ways to compensate for the geometrical spreading effects. However, the model update directions preconditioned with the pseudo-Hessian matrices in CSG FWI and CRG FWI are slightly different due to the differences in approximating the Hessian matrix. Therefore, if some different methods that enable better approximation of the Hessian matrix are used, such as the L-BFGS, the preconditioned model update directions and final inversion results of CSG FWI and CRG FWI would be more similar to each other.

Additionally, the inversion test was performed only for 2D case. However, the ratio between the number of sources and receivers becomes much larger in 3D cases. For instance, the 3D OBC data acquired at the Volve oilfield of the North Sea has 37,603 airgun sources at the ocean surface and 3,840 receivers at the

ocean-bottom. Another OBC data set acquired at the Valhall oilfield, which has been popularly used in the studies of seismic inversion and migration, comprises 49954 airgun sources and 2302 receivers (Operto et al., 2015). Therefore, under the assumption that all traces of those two OBC survey data are used, the reduction ratios of computational cost by using CRG FWI instead of CSG FWI would be about 9.8 for the Volve data and 21.7 for the Valhall data, respectively. As a result, it is expected that the proposed CRG-based inversion scheme will be even more effective in the case of 3D FWI of ocean-bottom seismic data.

Chapter 4. Acoustic FWI with pseudo-Ax data

In acoustic FWI, pressure data are commonly used to reconstruct the P-wave velocity model. In this chapter, an acoustic FWI strategy is proposed that uses horizontal spatial differentiation of pressure data. These data are referred to as the pseudo-Ax data. Because narrow-angle PP and PS reflections at the pseudo-Ax data have smaller amplitudes than those at the pressure and horizontal particle acceleration (Ax) data, it is expected that the acoustic FWI with pseudo-Ax data would focus on reconstructing long-wavelength features of the models and constrain the update of short-wavelength features related to the narrow-angle reflections.

4.1. Characteristics of each data component

4.1.1. Comparison of common-shot gathers

To observe the characteristics of each data component, acoustic and elastic wave simulations are performed with the P- and S-wave velocity models given in Fig. 4-1. The P-wave velocity model in Fig. 4-1a consists of water layer, linearly increasing velocity layer and consolidated high-velocity layer. Fig. 4-1b shows the S-wave velocity model estimated from the P-wave velocity model using the empirical relationships proposed by Castagna et al. (1985) and Christensen (1996):

$$v_s = \begin{cases} 0 & \text{for } v_p \leq 1.5 \\ (v_p - 1.36)/1.16 & \text{for } 1.5 < v_p \leq 3.5 \\ 0.53v_p & \text{for } 3.5 < v_p \end{cases} \quad (27)$$

In Fig. 4-2, CSGs of pressure, Ax and vertical particle acceleration (Az) data

obtained from acoustic and elastic wave simulations are compared with each other. Note that the elastic CSGs are horizontally flipped in this figure.

First, by comparing the acoustic CSGs (right panels of Fig. 4-2) of pressure, A_x and A_z , it is noticed that the A_x data show strong amplitudes of the direct and diving waves but weak amplitudes of the PP reflections, particularly at near offsets, compared to the pressure data. These near-offset PP reflections strongly appear at the A_z data. This is attributed to the ray-paths of PP reflections as shown in Fig. 4-3. PP reflections at near offsets enter receivers in an almost vertical direction and their particle motions are parallel to this propagation direction (i.e., vertical direction). Therefore, near-offset PP reflections cause strong vertical particle motions at the receivers and distinctly recorded at A_z data rather than at A_x data.

Then, by investigating the elastic CSGs (left panels of Fig. 4-2) of pressure, A_x and A_z , it is noticed that the A_x data contain strong PS reflections at near offsets compared to the pressure and A_z data. Similar to the case of PP reflections, the near-offset PS reflections enter receivers in an almost vertical direction and result in particle motion normal to this propagation direction (i.e., horizontal direction; refer to Fig. 4-4). Therefore, narrow-angle PS reflections cause strong horizontal particle motions at the receivers and distinctly recorded at the A_x data. However, because these PS reflections need to be converted into P-wave to be recorded at the pressure data, the amplitudes of these PS reflections are weak at the pressure data. Sears et al. (2008) also observed these characteristics of data components and used elastic A_x data in the final stage of elastic FWI to reconstruct short-wavelength features of the S-wave velocity model.

To focus on the reconstruction of long-wavelength features of the velocity model, it is important to suppress the updates of short-wavelength features related to the near-offset PP and PS reflections. For this purpose, the horizontal spatial

differentiation of recorded pressure data, which is referred to as pseudo-Ax data, is used in FWI. As shown in Fig. 4-5, the pseudo-Ax data maintain the characteristic of acoustic Ax data in the aspect of strong direct and diving waves and weak near-offset PP reflections. In addition, because the PS reflections are weak at pressure data, this pseudo-Ax data that originate from pressure data also show weak near-offset PS reflections.

Following the studies of Wu and Toksoz (1987) and Woodward (1992), there is a relationship between the local wavenumber of model update direction and opening angle as follows (refer to Appendix D):

$$\mathbf{k} = \frac{2\omega}{v} \cos\left(\frac{\theta}{2}\right) \mathbf{n} , \quad (28)$$

where \mathbf{k} is the local wavenumber (i.e., inverse of wavelength) vector; ω , v , θ denote the angular frequency, velocity of the local media, opening angle between the source and receiver wavefields, respectively; \mathbf{n} is the unit vector showing the direction of slowness (Virieux and Operto, 2009; Alkhalifah, 2015). From eq. (28), it is noticed that the narrow-angle reflections are related to the reconstruction of short-wavelength features of the models. Therefore, acoustic FWI with pseudo-Ax data, which are free from the narrow-angle reflections, would help primarily reconstruct long-wavelength features of the given models.

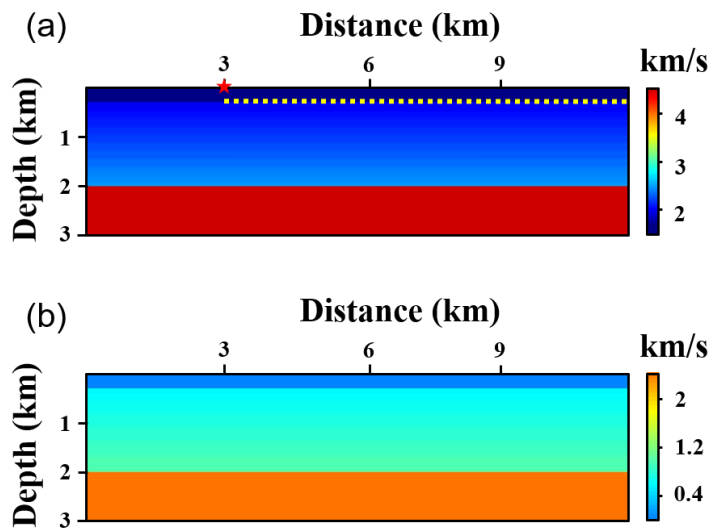


Fig. 4-1. (a) P-wave velocity model and (b) S-wave velocity model estimated from the empirical relationships: The red star indicates the source position and the yellow dotted line shows the receiver line at the ocean-bottom.

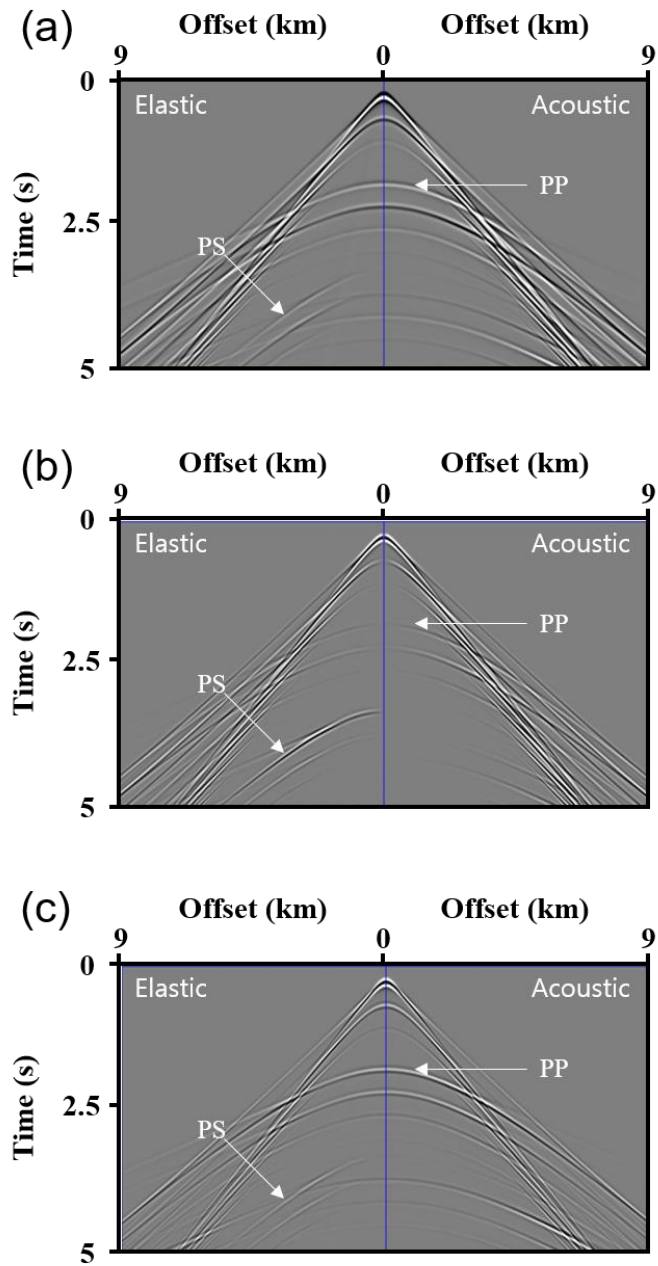


Fig. 4-2. Acoustic and elastic common-shot gathers of (a) pressure, (b) horizontal and (c) vertical particle acceleration wavefields: PP and PS denote the types of reflections.

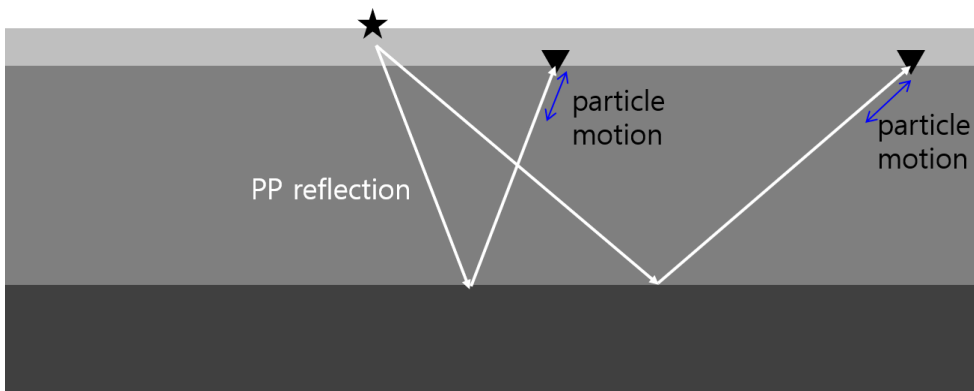


Fig. 4-3. Schematic diagram showing the ray-paths (the one-sided white arrows) and particle motions (the double-sided blue arrows) of PP reflections. At near offsets, PP reflections cause particle motions in an almost vertical direction.

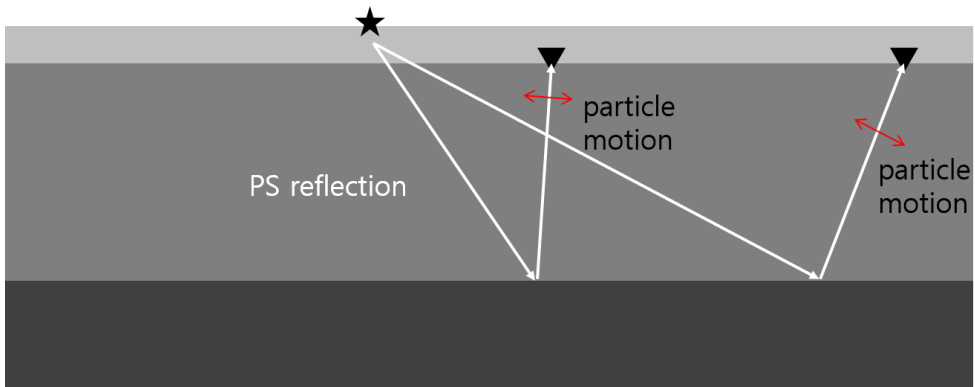


Fig. 4-4. Schematic diagram showing the ray-paths (the one-sided white arrows) and particle motions (the double-sided red arrows) of PS reflections. At near offsets, PS reflections cause particle motions in an almost horizontal direction.

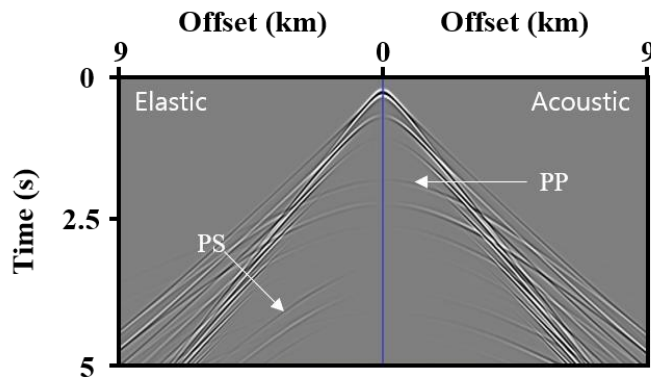


Fig. 4-5. Acoustic common-shot gather (CSG) of horizontal particle acceleration (Ax) wavefields (right panel) and elastic CSG of pseudo-Ax wavefields (left panel). Note that PS reflections are weaker at pseudo-Ax data than those at Ax data (refer to Fig. 4-2b).

4.1.2. Sensitivity kernel analysis

To visually observe the effect of using the pressure, A_x , A_z and pseudo- A_x data in acoustic FWI, sensitivity kernel analysis, which computes a single shot-receiver gradient, is performed. Fig. 4-6 shows the sensitivity kernels when using the acoustic pressure, A_x and A_z data at an offset of 1 km. For this near-offset case, sensitivity kernel with the A_x data (Fig. 4-6b) shows weak PP migration isochrone compared to that of pressure (Fig. 4-6a) due to the weak near-offset PP reflections of A_x data. This migration isochrone distinctly appears at the sensitivity kernel of A_z data (Fig. 4-6c). This means that the FWI with the acoustic A_x data limits the reconstruction of short-wavelength features of the models. However, for sensitivity kernel with elastic A_x data, additional migration isochrone (black arrows in Fig. 4-7b) appears. Because the strong PS reflections at elastic A_x data are regarded as acoustic wavefields during the back-propagation of recorded data in acoustic FWI and because these PS reflections are recorded at later time than PP reflections, the convolution between the source and receiver wavefields generates outer PS migration isochrone. Therefore, for acoustic FWI with elastic A_x data, it is expected that short-wavelength features related to the near-offset PS reflections would appear and degrade the quality of reconstructed P-wave velocity model. On the other hand, in case of using pseudo- A_x data (Fig. 4-7d), which show small amplitudes of both near-offset PP and PS reflections, the resulting sensitivity kernel no longer shows both the PP and PS migration isochrones and only the smooth kernel remains.

Until now, it is shown that acoustic FWI with pseudo- A_x data would focus on reconstructing the long-wavelength features of the models. However, because direct and diving waves are much stronger than the far-offset PP reflections at pseudo- A_x data (refer to Fig. 4-5), FWI with pseudo- A_x data mainly focuses on

reconstructing the shallow part of a given model up to the depth that diving waves reach. Therefore, additional preconditioning is needed to strengthen the update of deeper part of the model when using the pseudo-Ax data in acoustic FWI. Here, a depth-related damping term is applied to the pseudo-Hessian matrix as follows:

$$\bar{\mathbf{H}}_p(x, z) = \mathbf{H}_p(x, z) \frac{1}{(z)^c}, \quad (29)$$

where \mathbf{H}_p is the original pseudo-Hessian matrix calculated at the whole nodal point; z is the depth and c is an arbitrary coefficient used to determine the order of damping. Due to this damping term, the pseudo-Hessian matrix becomes smaller as the depth increases, therefore the preconditioned model update direction becomes larger with depth and enhances the update of deeper part of the model.

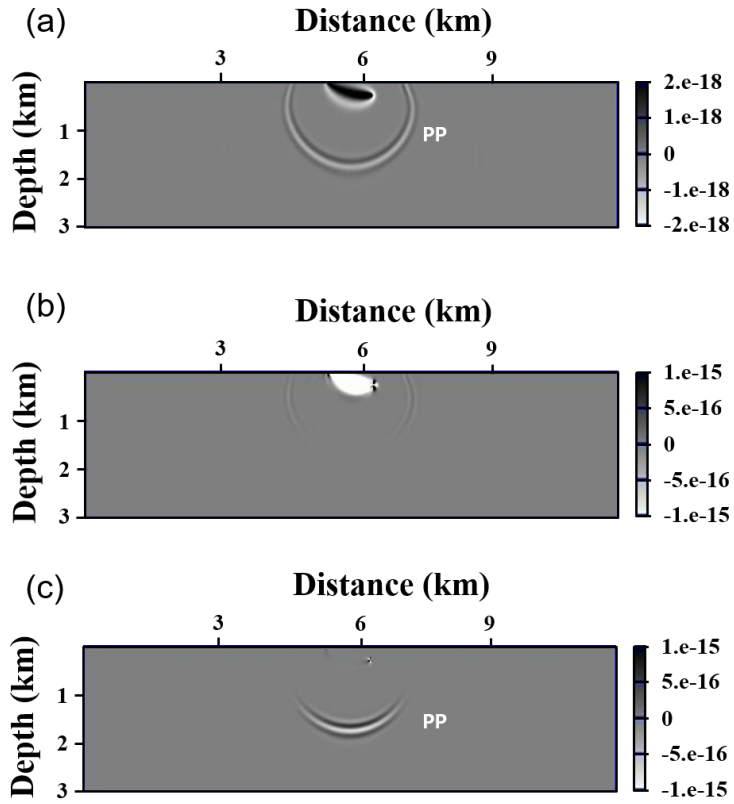


Fig. 4-6. Sensitivity kernels for the acoustic wavefields: (a) pressure, (b) horizontal and (c) vertical particle acceleration wavefields.

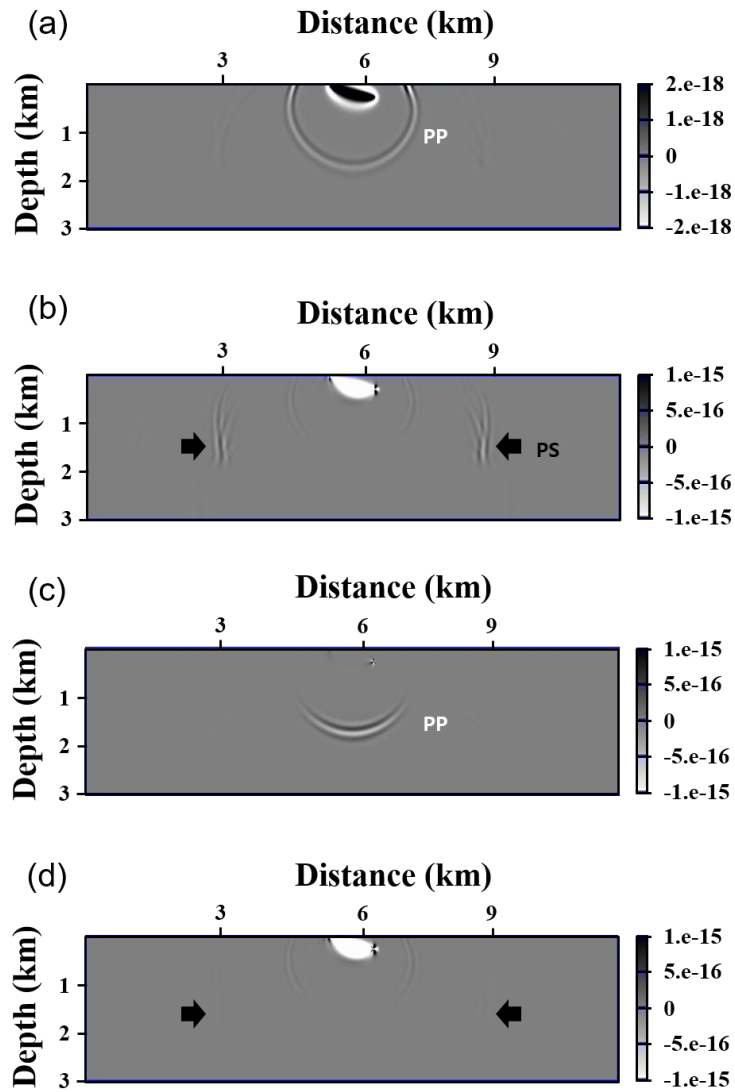


Fig. 4-7. Sensitivity kernels for the elastic wavefields: (a) pressure, (b) horizontal (Ax) and (c) vertical particle acceleration wavefields. Compared to the case of using acoustic Ax wavefield, additional PS migration isochrone (black arrows) appears. (d) is the sensitivity kernel for pseudo-Ax data, where both the PP and PS migration isochrones appear weak.

4.2. Usage of pseudo-Ax data in CRG FWI

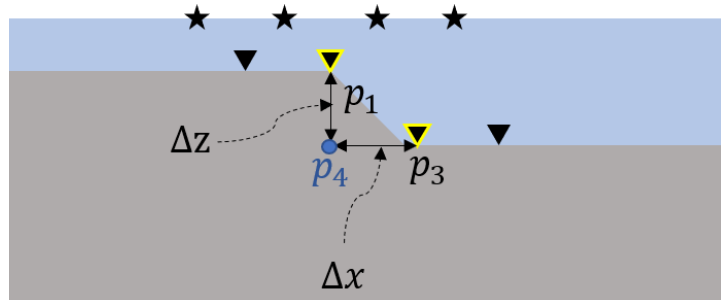
To constrain short-wavelength features in the gradients, acoustic FWI that uses pseudo-Ax data rather than pressure data is proposed. Because it is noticed that both the CSG FWI and CRG FWI result in the same gradients for acoustic FWI with pressure data (chapter 3), using the pseudo-Ax data instead of pressure data can also be done with CRG-based scheme. In other words, observed pseudo-Ax data is obtained from the observed pressure CRGs and is matched with the modeled pseudo-Ax data in source-receiver switched geometry. It should be noted that CRG FWI with pseudo-Ax data results in different gradient with that from CSG FWI with pseudo-Ax data, because the seismic reciprocity theorem is no longer satisfied for pseudo-Ax data.

An advantage of using pseudo-Ax data in CRG-based scheme is that the difficulty of calculating observed pseudo-Ax data at fluctuating ocean-bottom surface is resolved. Because the pseudo-Ax data are the horizontal spatial differentiations of pressure data, the whole pressure wavefield should be recorded at the same depth (assuming flat ocean-bottom surface) to properly obtain pseudo-Ax data. If the pressure data are recorded at the fluctuating ocean-bottom surface, therefore the depth of receivers largely varies, proper processing techniques to adjust the depth of receivers must be employed before the calculation of pseudo-Ax data.

One may ignore the ocean-bottom topography and just take the pressure difference between the horizontally adjacent receiver positions as shown in Fig. 4-8, but the calculated pressure difference would not guarantee the characteristic of pseudo-Ax data, such as extremely weak near-offset PP reflections. Fig. 4-9 shows the case of dipping ocean-bottom surface. By performing an acoustic wave

simulation for the P-wave velocity model shown in Fig. 4-9a, pressure and Ax CSGs are obtained as in Figs. 4-9b and 4-9c. Despite the dipping ocean-bottom surface, it is noticed that Ax CSG would show weak near-offset PP reflections. However, ignoring the ocean-bottom topography, horizontal pressure difference from the pressure CSG is calculated as in Fig. 4-9d and shows quite strong near-offset PP reflections. This is because particle motions in the vertical direction would also be included in the calculated pressure difference. Therefore, CSG FWI with this pressure difference would show short-wavelength features in the gradients.

On the other hand, because the depths of source positions are quite constant for ocean-bottom seismic data, pseudo-Ax data inversion with CRG-based scheme properly calculates pseudo-Ax data, resolving the issue of ocean-bottom topography (refer to Fig. 4-10). Because CRG FWI assumes source-receiver switched geometry for recorded pressure data (Fig. 4-11a), the observed pseudo-Ax data are computed following the ocean surface and represent the pressure difference only due to the horizontal change of receiver positions (original source positions in the acquisition geometry of Fig. 4-9a). Therefore, as shown in Fig. 4-11d, calculated horizontal pressure difference would show weak short-angle PP reflections. Additionally, the computation cost of FWI of ocean-bottom seismic data would be reduced due to the smaller number of wave simulations in CRG FWI.



$$\begin{aligned}
 \mathbf{a}_{x,pseudo} &= (p_3 - p_1)/\Delta x \\
 &= (p_3 - p_4)/\Delta x + (p_4 - p_1)/\Delta x \\
 &= \mathbf{a}_x + (\Delta z/\Delta x)\mathbf{a}_z
 \end{aligned}$$

Fig. 4-8. Schematic diagram showing that the horizontal pressure difference with ocean-bottom topography is affected by both the horizontal and vertical particle motions: p_1 , p_3 are the pressure wavefields at the selected receiver positions, (x, z) and $(x + \Delta x, z - \Delta z)$, respectively; p_4 is the pressure wavefield at $(x, z - \Delta z)$.

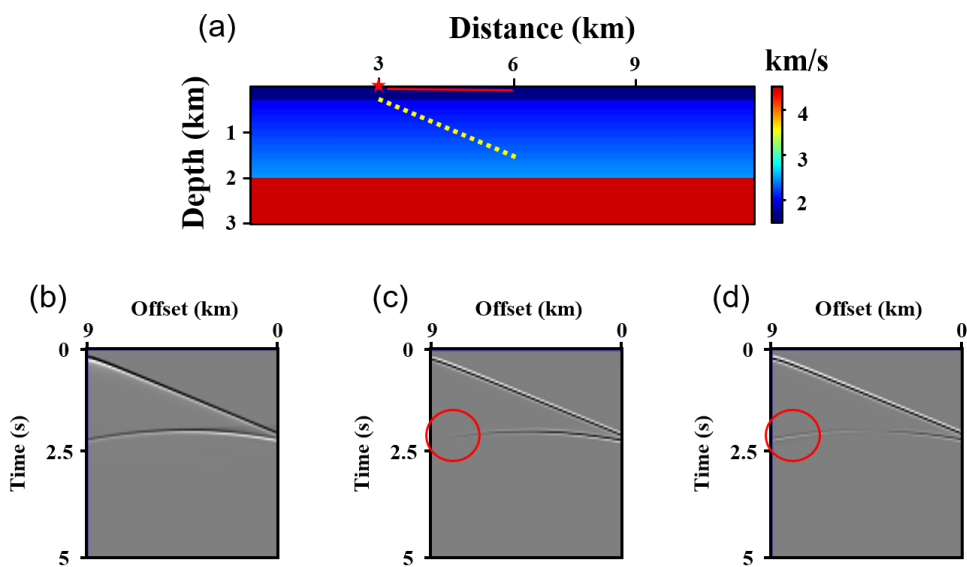
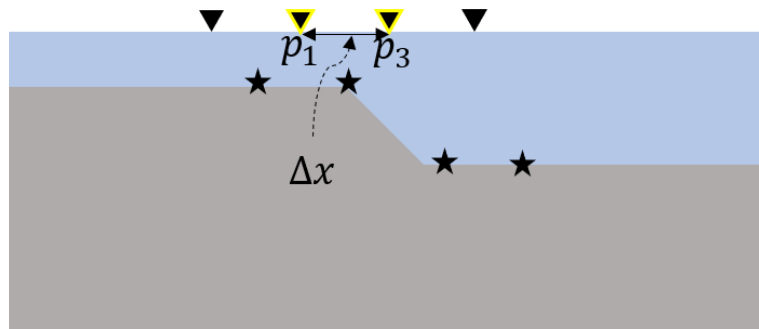


Fig. 4-9. (a) P-wave velocity model for acoustic wave simulation and common-shot gathers (CSG) of (b) pressure, (c) horizontal particle acceleration and (d) horizontal pressure difference: the red-solid and yellow-dotted lines in (a) indicate the source and receiver lines, respectively; the red star in (a) shows the source position for the representative CSGs in (b, c, and d); the red circles show that near-offset PP reflections are strong at the horizontal pressure difference in the source-receiver geometry of (a).



$$\begin{aligned} \mathbf{a}_{x,pseudo} &= (p_3 - p_1) / \Delta x \\ &= \mathbf{a}_x \end{aligned}$$

Fig. 4-10. Schematic diagram showing that the horizontal pressure difference in source-receiver switched geometry (CRG FWI) comes only from the horizontal particle motion: p_1 , p_3 are the pressure data at the selected receiver positions, (x, z) and $(x + \Delta x, z - \Delta z)$, respectively.

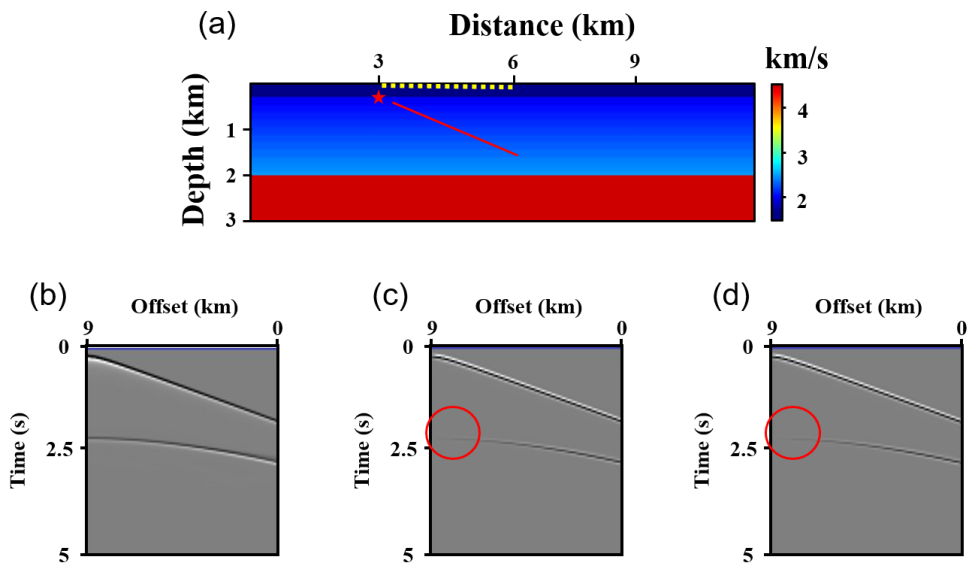


Fig. 4-11. (a) P-wave velocity model for acoustic wave simulation and common-shot gathers (CSG) of (b) pressure, (c) horizontal particle acceleration and (d) horizontal pressure difference: the red-solid and yellow-dotted lines in (a) indicate the source and receiver lines, respectively; the red star in (a) shows the source position for the representative CSGs in (b, c, and d); the red circles show that near-offset PP reflections are weak at the horizontal pressure difference in the source-receiver geometry of (a).

4.3. Synthetic data example: Volve tomography model

To demonstrate the effect of using pseudo-Ax data in acoustic FWI, observed pressure data are obtained with P- and S-wave velocity models shown in Fig. 4-12. These P- and S-wave velocity models are obtained from reflection tomography and released along with the OBC data of the Volve oilfield. Modeling parameters are listed in Table 4-1. Ricker wavelet with the maximum frequency of 18 Hz was used as a source signature. To avoid the numerical dispersion of S-waves during the elastic wave simulation, a grid interval of 6.25 m is employed to synthesize the observed data. Fig. 4-13 shows the representative CSGs of pressure, Ax and pseudo-Ax data. As expected, the CSG of pseudo-Ax data shows smaller amplitudes of PP and PS reflections at near offsets compared to those of pressure and Ax data.

Then, employing a grid interval of 25 m in acoustic FWI, the model update directions are calculated at the first iteration and are displayed in Fig. 4-14. Frequencies ranging from 3 Hz to 10 Hz with an interval of 0.4 Hz are used and the classical CSG-based scheme is employed for FWI. From Figs. 4-14a and 4-14c, it is noticed that the first model update direction obtained from pseudo-Ax data inversion shows smoother update of P-wave velocity model than that obtained from the pressure data inversion. On the other hand, the model update direction obtained from Ax data (Fig. 4-14b) shows additional short-wavelength features, which are irrelevant to the true P-wave velocity structures. Final inversion results for the P-wave velocity are shown in Fig. 4-15. In this figure, it is shown that the acoustic FWI with elastic Ax data (Fig. 4-15b) degrades the quality of inverted P-wave velocity due to the effect of strong PS reflections of the observed Ax data (Fig. 4-13b). Additionally in Fig. 4-15a, it is observed that short-wavelength features of the velocity model are excessively updated when using the pressure data

in acoustic FWI (particularly at the boundaries of distinct reflector near the depth of 3 km). This is attributed to the effect of strong PP reflections at the observed pressure data (Fig. 4-13a).

Fig. 4-16 shows the relative model misfit curves for inversion results obtained from pressure and pseudo-Ax data inversion, which are calculated from

$$\text{model misfit} = \sqrt{\frac{1}{N} \left(\frac{\mathbf{m}_{\text{inv}} - \mathbf{m}_{\text{true}}}{\mathbf{m}_{\text{true}}} \right)^2}, \quad (30)$$

where \mathbf{m}_{inv} and \mathbf{m}_{true} indicate the inverted and true P-wave velocity parameter vectors, respectively; N is the total number of nodal points (Prieux et al., 2013; Jeong et al., 2017; Zhong and Liu, 2019). For pressure data inversion, short-wavelength structures, such as reflector surfaces, are over-estimated to primarily match the strong PP reflections at near offsets, therefore the model misfit increases at later iterations. On the other hand, due to the characteristic of long-wavelength structure update, the model misfit tends to stably converge in case of pseudo-Ax data inversion.

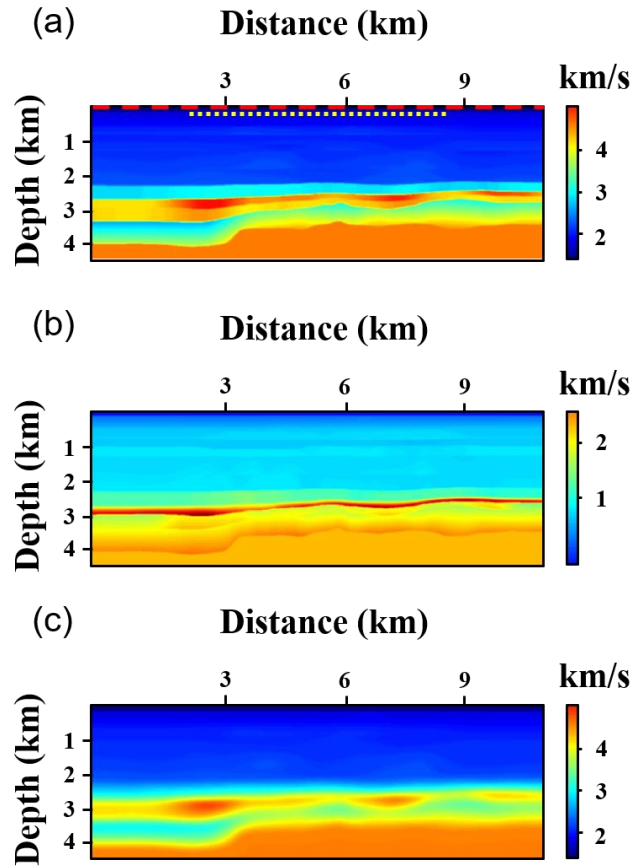


Fig. 4-12. Tomographic velocity models at the Volve oilfield of the North Sea: (a) P-wave velocity model, (b) S-wave velocity model, and (c) smoothed P-wave velocity model as an initial model for FWI; the red-dashed and yellow-dotted lines indicate the source and receiver positions, respectively.

Table 4-1. Modeling parameters for synthetic data for Volve oilfield tomographic velocity models.

Model	
Size	11.25 km x 4.525 km
Grid interval	0.00625 km
Source	
Wavelet	The first derivative of Gaussian function (maximum frequency of 18 Hz)
Total number	443
Interval	0.025 km
Receiver	
Total number	235
Interval	0.025 km
Depth	0.1 km

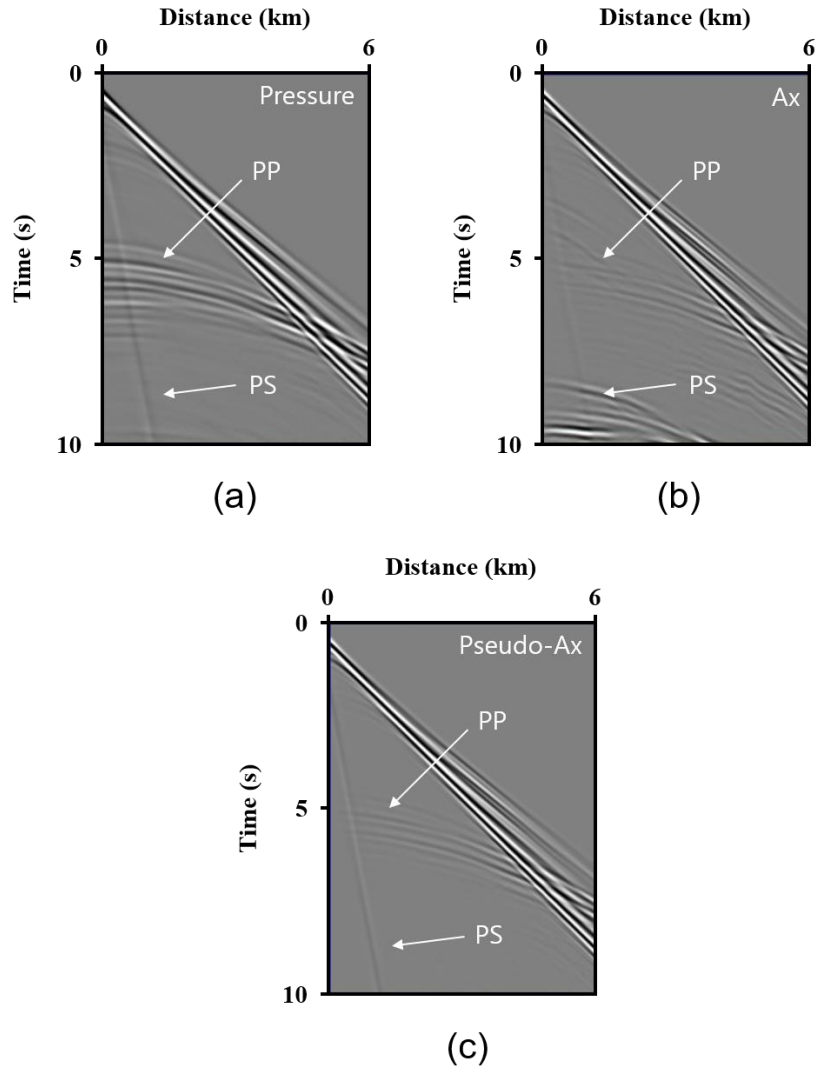


Fig. 4-13. Representative common-shot gathers of (a) pressure, (b) horizontal particle acceleration and (c) pseudo-Ax. Both the PP and PS reflections at near offsets are weak at pseudo-Ax data.

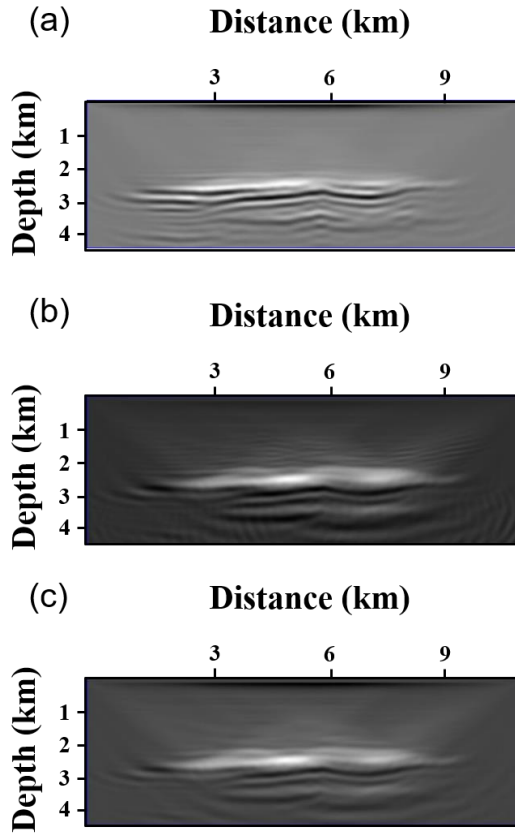


Fig. 4-14. The first iteration model update directions obtained from acoustic FWI with (a) pressure, (b) horizontal particle acceleration and (c) pseudo-Ax data.

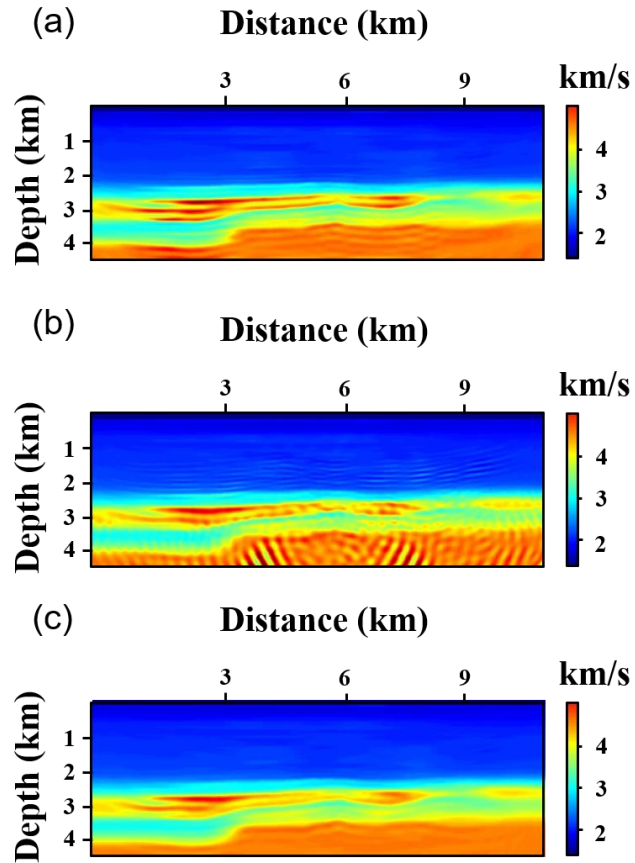


Fig. 4-15. Inversion results obtained from acoustic FWI with (a) pressure, (b) horizontal particle acceleration and (c) pseudo-Ax data. Note that excessive updates of the reflector boundaries are observed particularly near the depth of 3 km in (a) compared to (c).

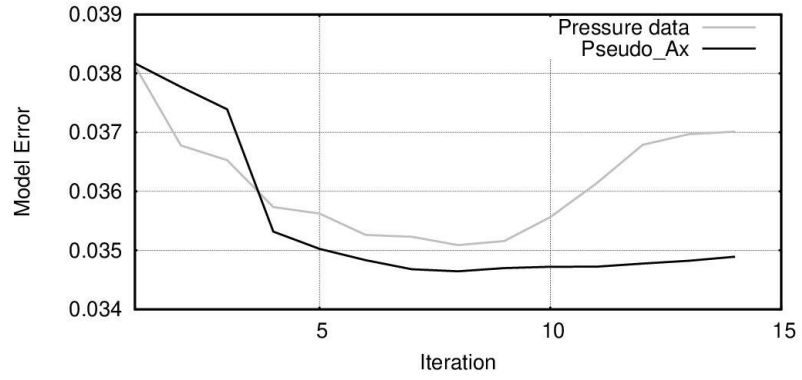


Fig. 4-16. Model error curves for acoustic FWI with pressure and pseudo-Ax data.

4.4. Discussion

In this chapter, acoustic FWI strategy that matches modeled and observed pseudo-Ax data is proposed to focus on the reconstruction of long-wavelength structures of the velocity models. However, in mathematical point of view, this approach is the same as taking the second-order horizontal spatial derivative to the pressure data residuals (refer to Appendix E). To further investigate the meaning of acoustic FWI with pseudo-Ax data, the radiation pattern of the second-order horizontal differentiation of pressure data with respect to the velocity perturbation is investigated.

With respect to the velocity perturbation, the partial derivative pressure wavefield $(\partial p_u / \partial \mathbf{m})$ shows an isotropic pattern as shown in Fig. 4-17a. This means that regardless of the opening angle between the source, perturbation point and receiver, scattered pressure wavefields propagate to receivers with the same amplitude. On the other hand, the partial derivative of second-order horizontal differentiation of pressure wavefield, $\partial(\partial^2 p_u / \partial x^2) / \partial \mathbf{m}$, shows an anisotropic radiation pattern as shown in Fig. 4-17b. From this figure, it is observed that the scattered wavefields with large opening angles would be stronger than those with small opening angles. Therefore, it is demonstrated that the acoustic FWI with pseudo-Ax data would enhance the reconstruction of long-wavelength features of the models.

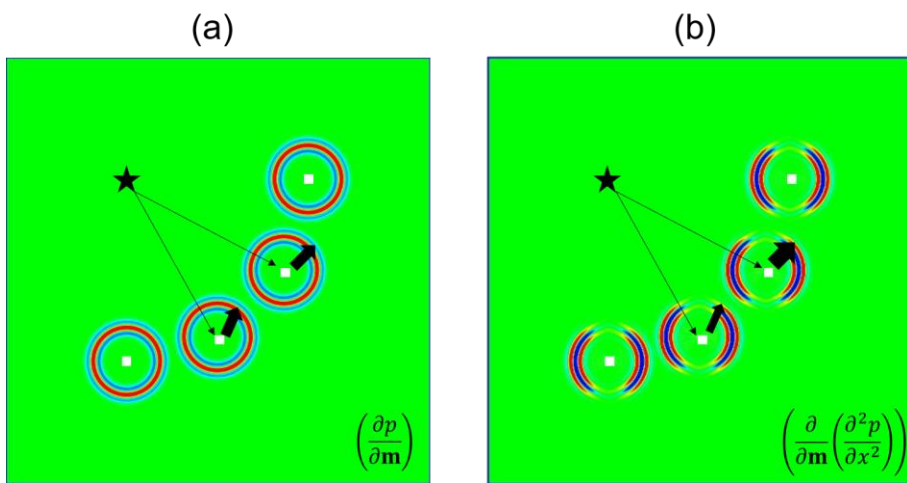


Fig. 4-17. Radiation pattern analysis with (a) pressure data and (b) second-order horizontal differentiation of pressure data: The black star denotes the source position and white rectangles represent the velocity perturbation points; the widths of black arrows show the relative amplitude of scattered wavefields.

Chapter 5. Real data example: Volve oilfield data in the North Sea

5.1. Data preprocessing

To mitigate the nonlinearity problem and to reduce the computational cost of acoustic FWI of ocean-bottom seismic data, the acoustic FWI strategy with pseudo-Ax data obtained from the pressure CRGs is proposed. For further demonstration of this inversion strategy, ocean-bottom 3D seismic data set acquired at Volve oilfield of North Sea (refer to Fig. 5-1) is used. This 3D data set was acquired with 16 ocean-bottom cables in 2010, and has officially been released by Equinor and its former Volve license partners since Oct. 2018. Total numbers of airgun sources and 4-component receivers per cable are 37,603 and 240, respectively. For 2D FWI, data recorded through a single receiver cable (No. 40195-1252860) with sources positioned along the same line (refer to Fig. 5-2) are selected. The total number of selected sources is 443 and the average depth of sea bottom is about 100 m. For preprocessing, several steps are carried out, such as trace-editing and trace-interpolation (which relocates all the receivers on the modeling nodes with the grid interval of 25 m for both the horizontal and vertical directions). The total number of relocated receivers is 235. Several additional preprocessing steps are conducted, such as 3D-to-2D conversion (Cruse et al. 1990; Huang and Schuster 2018) and convolving the synthetic source wavelet to recorded seismic traces to remove high-frequency data components (which is important to avoid numerical dispersion during the backpropagation of the residual wavefields). The P-wave velocity model obtained from reflection tomography has also been released along with the 3D OBC data set (shown in Fig. 4-12a). As shown in Fig. 5-3, geological information of survey area is denoted along with the tomographic

P-wave velocity model (Jackson and Lewis, 2016), and a smoothed version of this model (refer to Fig. 4-10c) is used for an initial guess of the P-wave velocity model. The source and receiver locations are the same as the synthetic inversion example in chapter 4.

In Fig. 5-4, the representative CSGs of pressure, Ax and pseudo-Ax after the preprocessing stage are displayed. Similar to the synthetic CSGs in Fig. 4-13, distinct PP reflections at pressure CSG, distinct PS reflections at Ax CSG (indicated with the white arrows) and smaller amplitude of both PP and PS reflections, particularly at near offsets, at pseudo-Ax CSG are observed. To implement CRG FWI, pressure data traces are sorted into CRG as shown in Fig. 5-5a. Pseudo-Ax data obtained from this representative pressure CRG is shown in Fig. 5-5b.

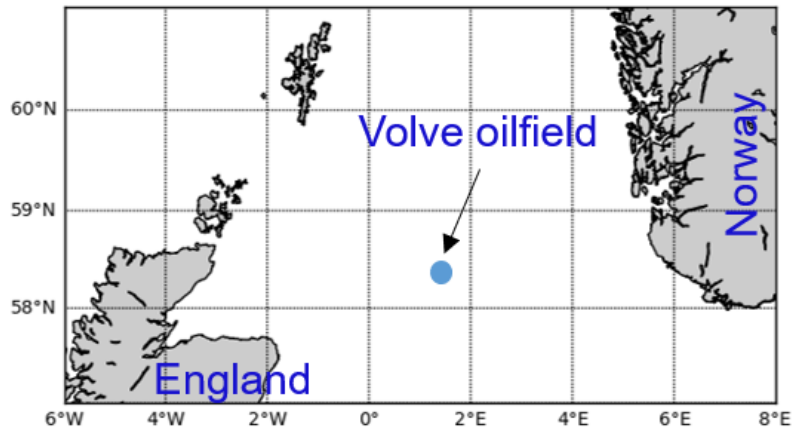


Fig. 5-1. The location of Volve oilfield at North Sea.

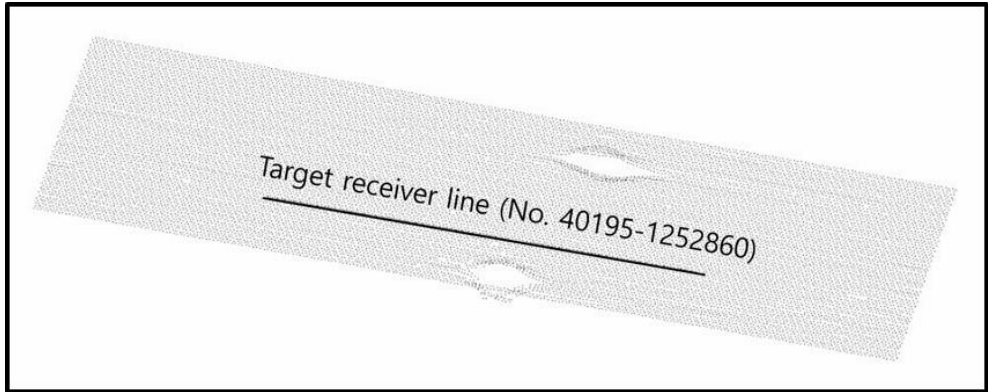


Fig. 5-2. Source-receiver geometries of selected receiver cable of OBC data acquired at Volve oilfield of North Sea. The black line indicates the target receiver cable (No. 40195-1252860) and the gray dots show the plane view of all applied source positions related to this receiver cable. For 2D FWI, only the seismic traces whose source positions are located along this receiver cable line are selected and used.

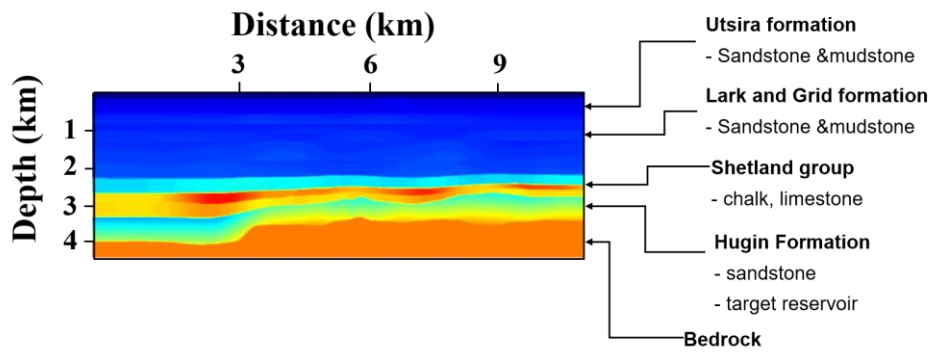


Fig. 5-3. P-wave velocity model of the survey area obtained from the reflection tomography. Geological information of survey area is given by Jackson and Lewis (2016).

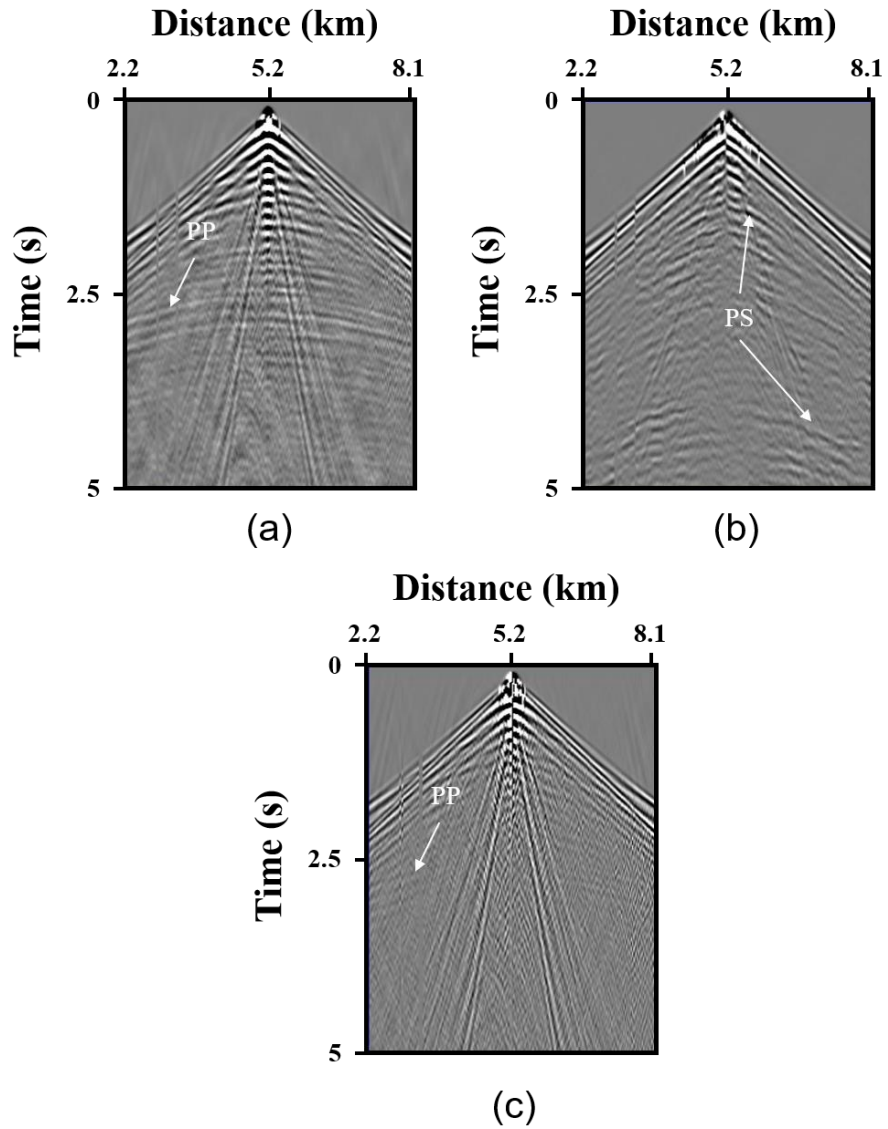


Fig. 5-4. Representative common-shot gathers of (a) pressure, (b) horizontal particle acceleration and (c) pseudo-Ax data.

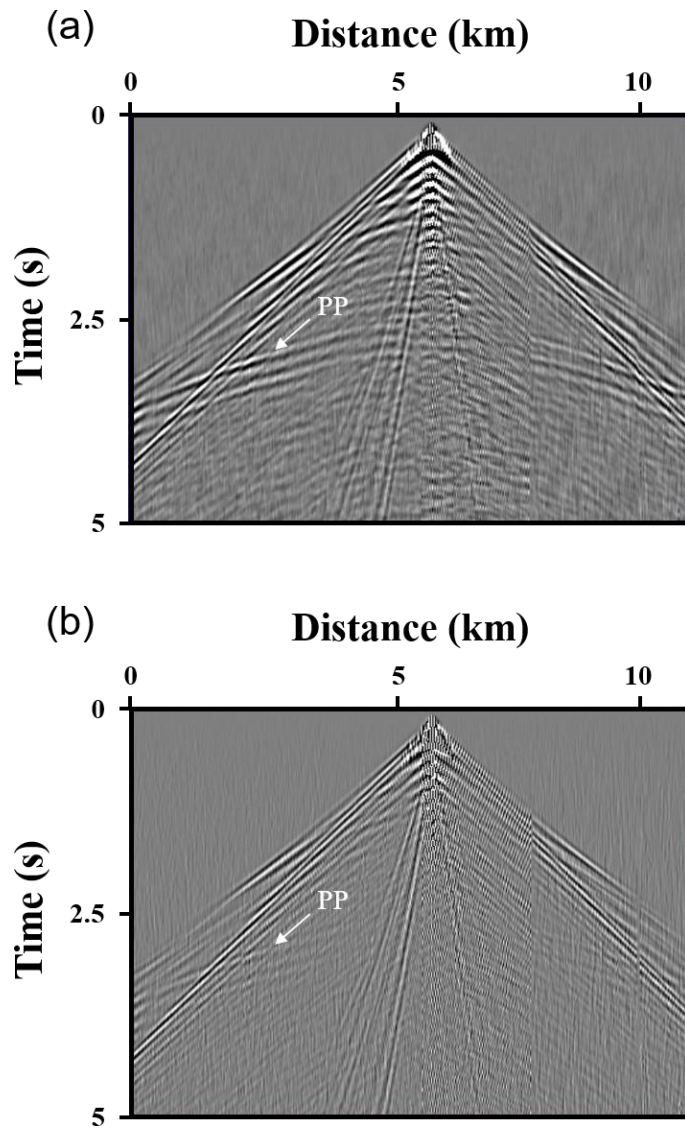


Fig. 5-5. Representative common-receiver gathers of (a) pressure and (b) pseudo-Ax data.

5.2. Inversion results

The model update directions at the first iteration and the final inversion results using the CSG- and CRG-based schemes are shown in Figs. 5-4 and 5-5. For acoustic FWI, frequencies in the range of 3.4 Hz to 10 Hz with an interval of 0.4 Hz are used. As in the synthetic example of chapter 3, some differences between the CSG FWI and CRG FWI with pressure data are observed due to the differences of pseudo-Hessian matrices (Figs. 5-7a and 5-7d). However, the difference of pseudo-Hessian matrices only affect the scaling of the gradients, therefore overall updated structures seem to be similar to each other.

For acoustic FWI with pseudo-Ax data, both the CSG- and CRG-based schemes seem to offer similar inversion results (Figs. 5-7c and 5-7e), but note that the gradients of each scheme is not the same. Both the CSG FWI and CRG FWI with pseudo-Ax data seem to be successful for this Volve oilfield data, but this is because the ocean-bottom surface of survey area is quite flat. If the ocean-bottom surface largely fluctuates, inversion results of each scheme with pseudo-Ax data would be quite different and CRG FWI with pseudo-Ax data would show smoother inverted P-wave velocity model compared to that from CSG FWI with pseudo-Ax data.

The comparison of required computational time between CSG FWI and CRG FWI is shown in Table 5-1, for both the pressure and pseudo-Ax data inversion. Because the computational cost in time-frequency-domain FWI is proportional to the number of used sources, it is observed that the computational speedup between CSG FWI and CRG FWI is about the same as the ratio of the number of sources to the number of receivers.

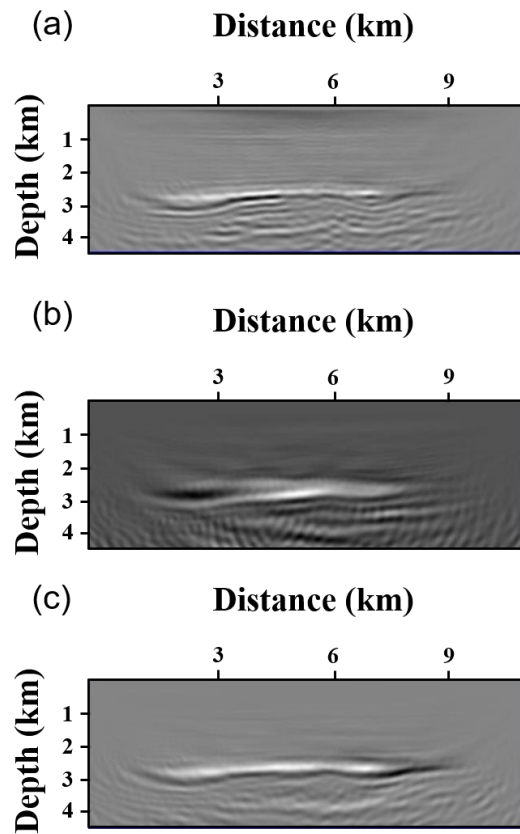


Fig. 5-6. Model update directions at the first iteration when using (a, d) pressure, (b) horizontal particle acceleration and (c, e) pseudo- A_x data in (a, b, c) CSG FWI and (d, e) CRG FWI.

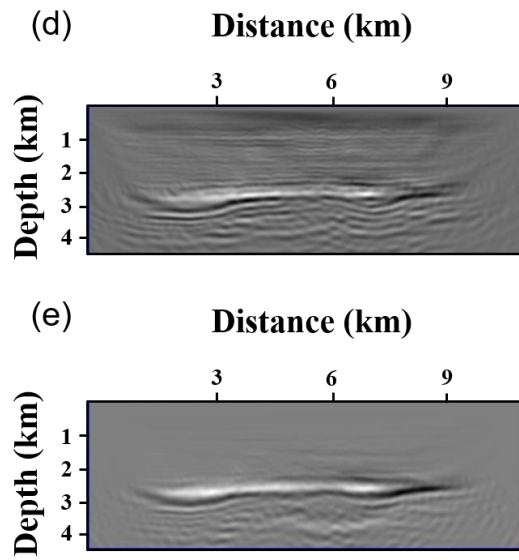


Fig. 5-6. (Continued)

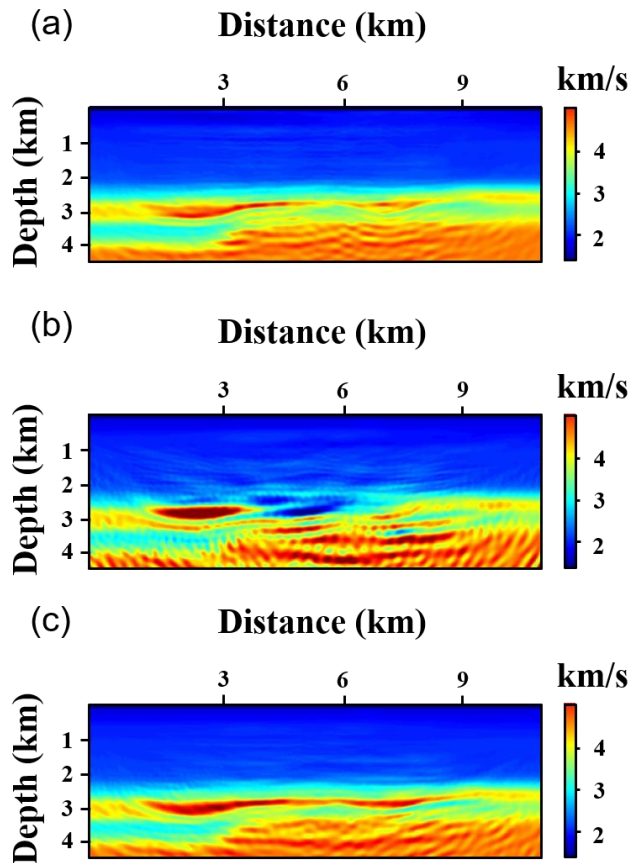


Fig. 5-7. Inverted P-wave velocity models obtained from acoustic FWI with (a, d) pressure, (b) horizontal particle acceleration and (c, e) pseudo-Ax data in (a, b, c) CSG FWI and (d, e) CRG FWI.

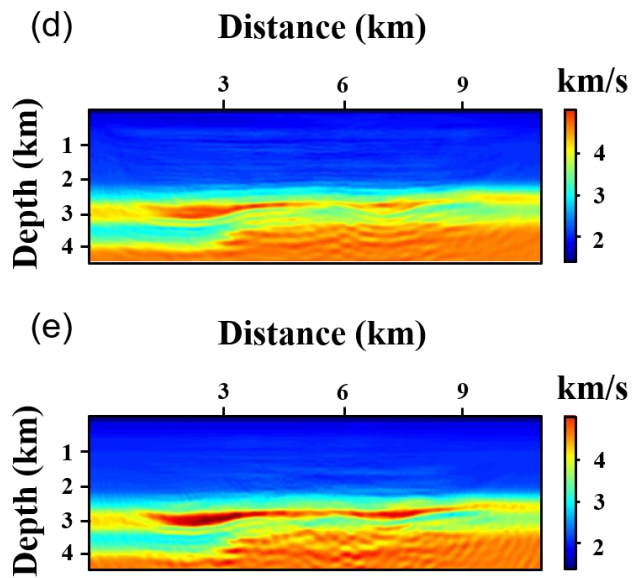


Fig. 5-7. (Continued)

Table 5-1. Comparison of computational time per iteration for CSG FWI (T_{CSG}) and CRG FWI (T_{CRG}) in the time-frequency domain for real data example of the Volve oilfield: ns and nr indicate the number of sources and receivers, respectively.

	T_{CSG} (sec)	T_{CRG} (sec)	$T_{\text{CSG}}/T_{\text{CRG}}$	$\frac{ns}{nr}$
Pressure	10314.382	5392.954	1.913	1.885
Pseudo-Ax	10320.218	5399.369	1.911	1.885

5.3. Quality Control

Comparing the results of pressure, Ax and pseudo-Ax data inversion, it is noticed that acoustic FWI with Ax data shows short-wavelength structure updates that seem to be due to the strong PS reflections and fails to reconstruct reasonable P-wave velocity model. On the other hand, acoustic FWI with pressure data or pseudo-Ax data converges to reliable velocity models and shows distinct reflector at the depth of around 3 km. However, unlike the pseudo-Ax data inversion, acoustic FWI with pressure data is mainly focused on the update of reflector boundaries (i.e., short-wavelength features of the model) and the distinct reflector appear to be discontinuous.

Fig. 5-8 shows the migration images obtained from the velocity model of pressure data inversion (Fig. 5-7d) and that of pseudo-Ax data inversion (Fig. 5-7e). Note that both the images show the distinct-continuous reflectors at the depth of around 3 km. In this Volve oilfield, the target oil reservoir is known to be located beneath the carbonate caprock, which is at the depth of around 3 km (refer to Fig. 5-3). With this a-priori information of caprock, result of pseudo-Ax data inversion, which clearly delineates the caprock of the reservoir, seems to be more reasonable compared to the result of pressure data inversion. Fig. 5-9 shows the velocity models of each data inversion (pressure data inversion and pseudo-Ax data inversion) overlapped with the corresponding migration images.

Additionally, several methods are used for further investigation of the quality of each reconstructed velocity model. The first method is to compare the modeled CSG of inverted velocity model with the observed CSG used in FWI. Fig. 5-10 shows the modeled and observed pressure CSGs with the P-wave velocity models shown in Figs. 5-7d and 5-7e. Both the modeled CSGs show the distinct reflection

hyperbola at around 3 seconds as observed CSG. However, for far-offset PP reflections, the modeled CSG using the inverted velocity model of Fig. 5-7e (the result of pseudo-Ax data inversion) fits well with the observed CSG compared to that using the inverted velocity model of Fig. 5-7d (the result of pressure data inversion). This is attributed to the characteristic of pseudo-Ax data. Because only the far-offset PP reflections distinctly appear at pseudo-Ax data, acoustic FWI with pseudo-Ax data preferentially matches the traveltime of far-offset PP reflections rather than that of near-offset PP reflections.

Secondly, the angle-domain common-image gathers (ADCIG) are obtained to investigate the quality of inverted P-wave velocity models. Because ADCIGs are computed at certain horizontal locations by extending the aperture between the source and receiver wavefields, correct velocity model would result in flattened reflectors at each gather (Sava and Fomel, 2003). Comparing the ADCIGs shown in Fig. 5-11, it is observed that the reflectors (indicated with red arrows) in Fig. 5-11b (obtained from the reconstructed velocity of pseudo-Ax data inversion; Fig. 5-7e) are more flattened than those in Fig. 5-11a (obtained from the reconstructed velocity of pressure data inversion; Fig. 5-7d). These observations show that the acoustic FWI with pseudo-Ax data gives more reliable P-wave velocity model than that with pressure data.

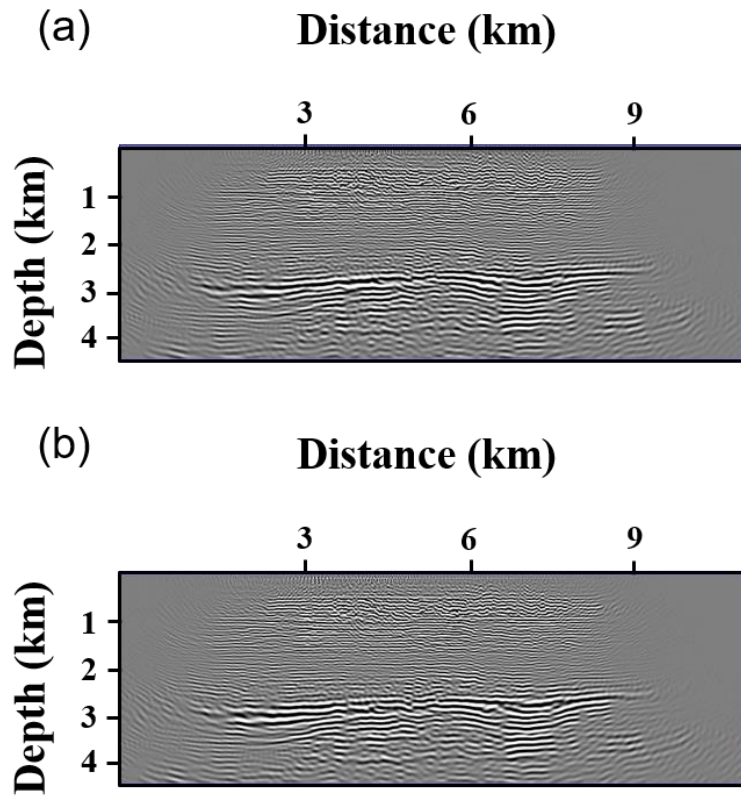


Fig. 5-8. Migration images for the P-wave velocity models inverted using (a) pressure data (Fig. 5-7d) and (b) pseudo-Ax data (Fig. 5-7e).

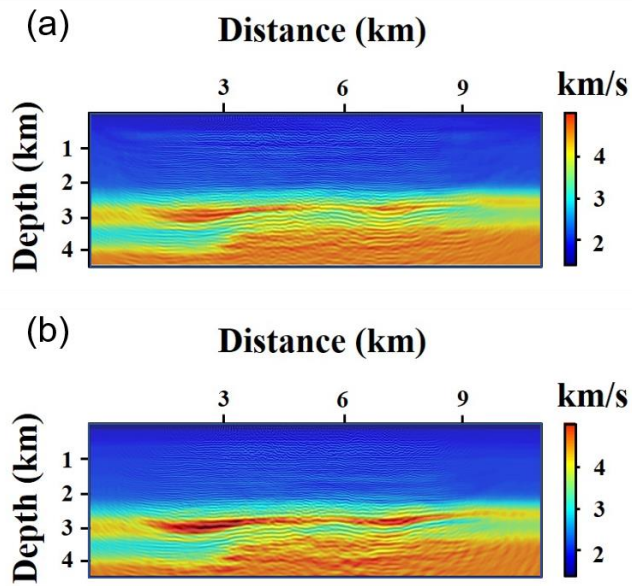


Fig. 5-9. Inverted P-wave velocity models overlapped with the migration images:
(a) pressure data inversion (Fig. 5-7d) and (b) pseudo-Ax data inversion (Fig.5-7e).

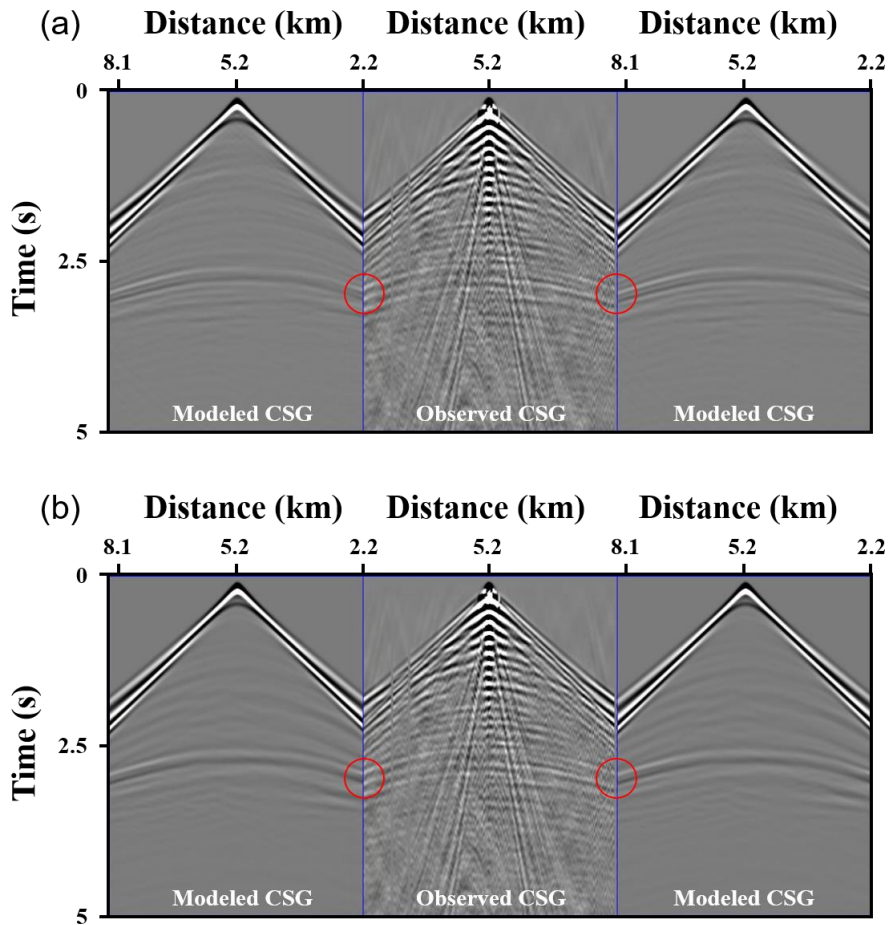


Fig. 5-10. Modeled and observed pressure CSGs for the P-wave velocity models inverted using (a) pressure data (Fig. 5-7d) and (b) pseudo-Ax data (Fig. 5-7e): The red circles indicate that the far-offset PP reflection better matches in case of pseudo-Ax data inversion compared to the case of pressure data inversion; note that modeled CSGs are horizontally flipped.

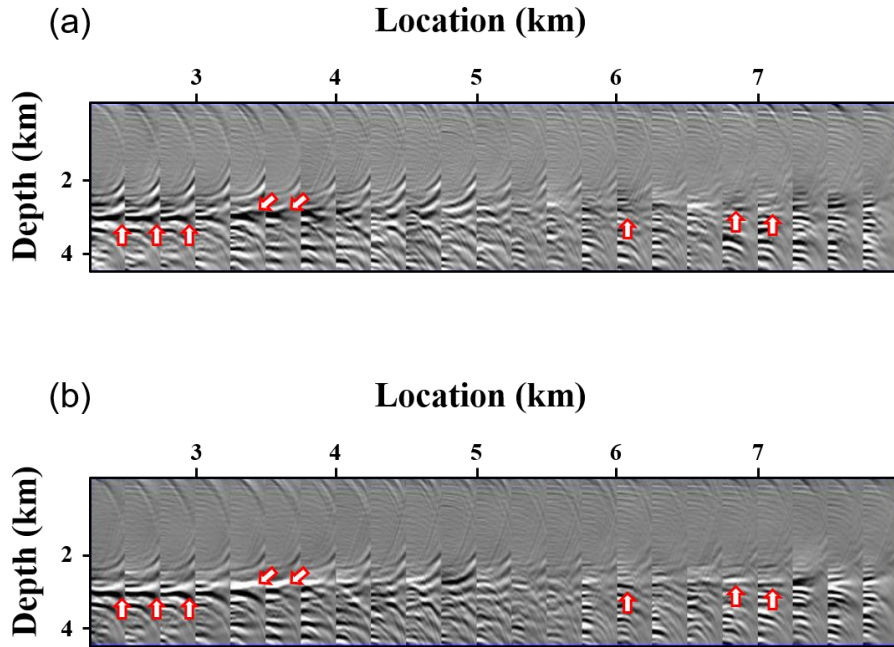


Fig. 5-11. Angle-domain common-image gathers (ADCIG) for the P-wave velocity models inverted using (a) pressure data (Fig. 5-7d) and (b) pseudo-Ax data (Fig. 5-7e): The red arrows show that reflectors appear to be more flattened when using the velocity of pseudo-Ax data inversion compared to those when using the velocity of pressure data inversion.

Chapter 6. Conclusions

These days, studies on FWI consider more complex nature of the Earth, such as elasticity, anisotropy and attenuation, for more sophisticated simulation of seismic wave propagation. However, acoustic FWI based on the simple acoustic wave equation is still widely used in the industry due to its small computational cost and less suffering from the local minima problem. In this thesis, I proposed an acoustic FWI strategy using pseudo-Ax data that are obtained from the pressure CRG to enhance the performance of acoustic FWI of ocean-bottom seismic data.

Because ocean-bottom seismic data commonly contain numerous sources and limited number of receivers, the classical CSG-based FWI requires huge computational cost. To reduce the computational burden of FWI for ocean-bottom seismic data, I tried to reduce the required number of wave simulations in FWI and proposed to match observed CRG with modeled CSG in source-receiver switched geometry when the number of sources largely exceeds the number of receivers. Thanks to the seismic reciprocity theorem, CRG FWI shares the same gradients and approximate-Hessian matrices as CSG FWI. However, because there is no computational speed-up for CRG FWI with Gauss-Newton method, the pseudo-Hessian matrix is used as a preconditioner of the gradient. For synthetic example of the Marmousi-II model, the CRG FWI resulted in similar inverted velocity model to that obtained from the CSG FWI, but with reduced computational burden.

In addition, the method of using pseudo-Ax data, which are the horizontal spatial differentiation of pressure data, rather than pressure data themselves in acoustic FWI was proposed. From the CSGs of pressure, Ax, Az and pseudo-Ax data, it was observed that the pseudo-Ax data show relatively weak PP and PS reflections at near offsets. Due to this characteristic of pseudo-Ax data, the

sensitivity kernel with pseudo-Ax data showed only the smooth kernel and the gradient of pseudo-Ax data inversion was smoother than those of pressure and Ax data inversion. As a result, acoustic FWI with pseudo-Ax data helped alleviate the nonlinearity problem of FWI.

In this thesis, the CRG-based scheme was combined with the pseudo-Ax data inversion. In other words, observed pseudo-Ax data are calculated from the pressure CRGs and matched with modeled pseudo-Ax data that are simulated in source-receiver switched geometry. Through this strategy, the difficulty of obtaining pseudo-Ax data for uneven ocean-bottom surface is resolved. With real OBC data set acquired at the Volve oilfield of North Sea, I demonstrated that the proposed strategy reduces total computational cost of FWI by reducing the number of wave simulations. Additionally, modeled CSGs and ADCIGs with inverted velocity models showed that the velocity model from pseudo-Ax data inversion is more reliable than that from conventional pressure data inversion.

References

- Agudo, O. C., da Silva, N. V., Warner, M. and Morgan, J., 2018, Acoustic full-waveform inversion in an elastic world, *Geophysics*, **83(3)**, R257-R271.
- Agudo, O. C., da Silva, N. V., Stronge, G. and Warner, M., 2020, Mitigating elastic effects in marine 3D full-waveform inversion, *Geophysical Journal international*, 2089-2104.
- Akrami, S. M., 2017, An algorithm for full waveform inversion of vector acoustic data, *PhD. Thesis: Memorial University of Newfoundland*.
- Alkhalifha, T., 2015, Scattering-angle based filtering of the waveform inversion gradients, *Geophysical Journal International*, **200**, 363-373.
- Badiey, M., Mu, Y. and Lynch, J., 2002, Temporal and azimuthal dependence of sound propagation in shallow water with internal waves, *IEEE Journal of Oceanic Engineering*, **27(1)**, 117-129.
- Ben-Hadj-Ali, H., Operto, S. and Virieux, J., 2011, An efficient frequency-domain full waveform inversion method using simultaneous encoded sources, *Geophysics*, **76(4)**, R109-R124.
- Berenger, J.-P., 1994, A perfectly matched layer for the absorption of electromagnetic waves, *Journal of Computational Physics*, **114**, 185-200.
- Bunks, C., Saleck, F. M., Zaleski, S. and Chavent, G., 1995, Multiscale seismic waveform inversion, *Geophysics*, **60(5)**, 1457-1473.
- Butzer, S., 2015, 3D elastic time-frequency full-waveform inversion, *PhD. Thesis: Karlsruhe Institut für Technologie (KIT)*.
- Castagna, J. P., Batzle, M. L. and Eastwood, R. L., 1985, Relationships between compressional-wave and shear-wave velocities in clastic silicate rocks, *Geophysics*, **50(4)**, 571-581.
- Choi, Y., 2007, Frequency-domain waveform inversion using elastic and acoustic-elastic coupled finite-element modeling technique, *PhD. Thesis: Seoul National University*.

- Choi, Y. and Alkhalifah, T., 2012, Application of multi-source waveform inversion to marine streamer data using the global correlation norm, *Geophysical Prospecting*, **60**, 748-758.
- Christensen, N. I., 1996, Poisson's ratio and crustal seismology, *Journal of Geophysical Research*, **101**, 3139-3156.
- Claerbout, J. F. and Doherty, S. M., 1972, Downward continuation of moveout-corrected seismograms, *Geophysics*, **37(5)**, 741-768.
- Collino, F. and Tsogka, C., 2001, Application of the perfectly matched absorbing layer model to the linear elastodynamic problem in anisotropic heterogeneous media, *Geophysics*, **66(1)**, 294-307.
- Crase, E., Pica, A., Noble, M., McDonald, J. and Tarantola, A., 1990, Robust elastic nonlinear waveform inversion: Application to real data, *Geophysics*, **55(5)**, 527-538.
- Ewing, W. M., Jardetzky, W. S. and Press, F., 1957, *Elastic waves in layered media*, Graw-Hill Book Company, Inc.
- Fletcher, R. and Reeves, C. M., 1964, Function minimization by conjugate gradients, *The Computer Journal*, **7(2)**, 149-154.
- Gauthier, O., Virieux, J. and Tarantola, A., 1986, Two-dimensional nonlinear inversion of seismic waveforms: Numerical results, *Geophysics*, **51(7)**, 1387-1403.
- Gazdag, J., 1978, Wave equation migration with the phase-shift method, *Geophysics*, **43(7)**, 1342-1351.
- Graves, R. W., 1996, Simulating seismic wave propagation in 3D elastic media using staggered-grid finite differences, *Bulletin of the Seismological Society of America*, **86(4)**, 1091-1106.
- Hestenes, M. R. and Stiefel, E., 1952, Methods of conjugate gradients for solving linear systems, *Journal of research of the national bureau of standards*, **49(6)**, 409-436.
- Huang, Y. and Schuster, G. T., 2018, Full-waveform inversion with multisource

- frequency selection of marine streamer data, *Geophysical Prospecting*, **66**, 1243-1257.
- Hwang, J., Oh, J. W., Kim, D. and Min, D.-J., 2020, Common-receiver gather FWI for ocean bottom cable data, *Pure and Applied Geophysics*, (under review).
- Ikelle, L. T. and Amundsen, L., 2005, Introduction to petroleum seismology: Society of Exploration Geophysicists, USA.
- Jackson, C. A.-L. and Lewis, M. M., 2016, Structural style and evolution of a salt-influenced rift basin margin; the impact of variations in salt composition and the role of polyphase extension, *Basin Research*, **28**, 81-102.
- Jeong, G., Hwang, J. and Min, D.-J., 2017, Comparison of weighting techniques for acoustic full waveform inversion, *Journal of Applied Geophysics*, **147**, 16-27.
- Jeong, W., Pyun, S., Son W. and Min D.-J., 2013, A numerical study of simultaneous-source full waveform inversion with l_1 -norm, *Geophysical Journal International*, **194**, 1727-1737.
- Jun, H., 2014, Laplace-Fourier domain elastic full waveform inversion using time-domain modeling, *Master thesis: Seoul National University*.
- Knopoff, L. and Gangi, A. F., 1959, Seismic reciprocity, *Geophysics*, **24(4)**, 681-691.
- Komatitsch, D. and Martin, R., 2007, An unsplit convolutional perfectly matched layer improved at grazing incidence for the seismic wave equation, *Geophysics*, **72(5)**, SM155-SM167.
- Krebs, J. R., Anderson, J. E., Hinkley, D., Neelamani, R., Lee, S., Baumstein, A. and Lacasse, M.-D., 2009, Fast full-wavefield seismic inversion using encoded sources, *Geophysics*, **74(6)**, WCC177-WCC188.
- Kwon, T., Seol, S. J. and Byun, J., 2015, Efficient full-waveform inversion with normalized plane-wave data, *Geophysical Journal International*, **201**, 53-60.
- Lailly, P., 1983, The seismic inverse problem as a sequence of before stack

migrations: Conference on Inverse Scattering, Theory and Application, Society of Industrial and Applied Mathematics, Expanded Abstracts, 206-220.

Levander, A. R., 1988, Fourth-order finite-difference P-SV seismograms, *Geophysics*, **53(11)**, 1425-1436.

Martin, G. S. and Marfurt, K., J., 2002, Marmousi-2: an updated model for the investigation of AVO in structurally complex areas, 72nd International Annual Meeting, SEG, Expanded Abstracts.

Mora, P., 1987, Nonlinear two-dimensional elastic inversion of multioffset seismic data, *Geophysics*, **52(9)**, 1211-1228.

Nocedal, J. and Wright, S. J., 1999, Numerical optimization, Springer-Verlag New York, Inc.

Oh, J.-W. and Alkhalifha, T., 2018, Full waveform inversion using envelope-based global correlation norm, *Geophysical Journal International*, **213**, 815-823.

Oh, J.-W. and Alkhalifah, T., 2019, Study on the full-waveform inversion strategy for 3D elastic orthorhombic anisotropic media: application to ocean bottom cable data, *Geophysical Prospecting*, **67**, 1219-1242.

Operto, S., Miniussi, A., Brossier, R., Combe, L., Haller, N., Kjos, E., Métivier, L., Milne, R., Ribodetti, A., Song, Z. and Virieux, J., 2015, Efficient 3D frequency-domain full-waveform inversion of ocean-bottom cable data- Application to Valhall in the Visco-ac, 77th Conference and Exhibition, EAGE, Expanded Abstracts.

Operto, S., Virieux, J., Amestoy, P., L'Excellent, J.-Y., Giraud, L. and Ben-Hadj-Ali, H., 2007, 3D finite-difference frequency-domain modeling of visco-acoustic wave propagation using a massively parallel direct solver: A feasibility study, *Geophysics*, **72(5)**, SM195-SM211.

Pica, A., Diet, J. P. and Tarantola, A., 1990, Nonlinear inversion of seismic reflection data in a laterally invariant medium, *Geophysics*, **55(3)**, 284-292.

Plessix, R.-E., 2006, A review of the adjoint-state method for computing the gradient of a functional with geophysical applications, *Geophysical*

Journal International, **167(2)**, 495-503.

- Plessix, R.-E., 2009, Three-dimensional frequency-domain full-waveform inversion with an iterative solver, *Geophysics*, **74(6)**, WCC149-WCC157.
- Polak, E. and Ribiere, G., 1969, Note sur la convergence de méthodes de directions conjuguées, *Revue Française D'informatique et de Recherche Opérationnelle. Série Rouge*, **3(16)**, 35–43.
- Pratt, R. G., 1990, Inverse theory applied to multi-source cross-hole tomography. Part 2: Elastic wave-equation method, *Geophysical Prospecting*, **38**, 311-329.
- Pratt, R. G., 1999, Seismic waveform inversion in the frequency domain, Part 1: Theory and verification in a physical scale model, *Geophysics*, **64(3)**, 888-901.
- Pratt, R. G., Shin, C. and Hick, G. J., 1998, Gauss-Newton and full Newton methods in frequency-space seismic waveform inversion, *Geophysical Journal International*, **133(2)**, 341-362.
- Pratt, R. G. and Worthington, M. H., 1990, Inverse theory applied to multi-source cross-hole tomography. Part 1: Acoustic wave-equation method, *Geophysical Prospecting*, **38**, 287-310.
- Prieux, V., Brossier, R., Operto, S. and Virieux, J., 2013, Multiparameter full waveform inversion of multicomponent ocean-bottom-cable data from the Vallhall field. Part1: Imaging compressional wave speed, density and attenuation, *Geophysical Journal International*, **194**, 1640-1664.
- Ramos-Martínez, J., Crawley, S., Zou, Z., Valenciano, A., Klochikhina, E. and Chemingui, N., 2016, A robust FWI gradient for high-resolution velocity model building, 86th Annual International Meeting, SEG, Expanded Abstracts.
- Ramos-Martínez, J., Qiu, L., Valenciano, A. A., Jiang, X. and Chemingui, N., 2019, Long-wavelength FWI updates in the presence of cycle skipping, *The Leading Edge*, 193-196.
- Routh, P., Krebs, J., Lazaratos, S., Baumstein, A., Chikichev, I., Downey, N., Lee,

- S., Hinkley, D. and Anderson, J., 2011, Full-wavefield inversion of marine streamer data with the encoded simultaneous source method, 73rd Conference and Exhibition, EAGE, Expanded Abstracts.
- Sava, P. C. and Fomel, S., 2003, Angle-domain common-image gathers by wavefield continuation methods, *Geophysics*, **68(3)**, 1065-1074.
- Schneider, W. A., 1978, Integral formulation for migration in two and three dimensions, *Geophysics*, **43(1)**, 49-76.
- Sears, T. J., Singh, S. C. and Barton, P. J., 2008, Elastic full waveform inversion of multi-component OBC seismic data, *Geophysical Prospecting*, **56**, 843-862.
- Shin, C. and Cha, Y. H., 2008, Waveform inversion in the Laplace domain, *Geophysical Journal International*, **173**, 922-931.
- Shin, C. and Cha, Y. H., 2009, Waveform inversion in the Laplace-Fourier domain, *Geophysical Journal International*, **177**, 1067-1079.
- Shin, C., Jang, S. and Min, D.-J., 2001a, Improved amplitude preservation for prestack depth migration by inverse scattering theory, *Geophysical Prospecting*, **49**, 592-606.
- Shin, C., Yoon, K., Marfurt, K. J., Park, K., Yang, D., Lim, H. Y., Chung, S. and Shin, S., 2001b, Efficient calculation of a partial derivative wavefield using reciprocity for seismic imaging and inversion, *Geophysics*, **66(6)**, 1856-1863.
- Sirgue, L., Etgen, J. T. and Albertin, U., 2008, 3D frequency domain waveform inversion using time-domain finite difference methods, 70th Conference and Exhibition, EAGE, Expanded Abstracts.
- Stolt, R. H., 1978, Migration by Fourier transform, *Geophysics*, **43(1)**, 23-48.
- Symes, W., 2010, Source synthesis for waveform inversion, 80th Annual International Meeting, SEG, Expanded Abstracts.
- Szydluk, T., Smith, P., Way, S., Aamodt, L. and Friedrich, C., 2007, 3D PP/PS prestack depth migration on the Volve field, *First Break*, **25**, 43-47.
- Tao, Y. and Sen, M. K., 2013, Frequency-domain full waveform inversion with

- plane-wave data, *Geophysics*, **78(1)**, R13-R23.
- Tarantola, A., 1984, Inversion of seismic reflection data in the acoustic approximation, *Geophysics*, **49**, 1259-1266.
- Vigh, D. and Starr, E. W., 2008, 3D prestack plane-wave, full-waveform inversion, *Geophysics*, **73(5)**, VE135-VE144.
- Virieux, J., 1986, P-SV wave propagation in heterogeneous media: Velocity-stress finite difference method, *Geophysics*, **51(4)**, 889-901.
- Virieux, J. and Operto, S., An overview of full-waveform inversion in exploration geophysics, *Geophysics*, **74(6)**, WCC127-WCC152.
- Woodward, M. J., 1992, Wave-equation tomography, *Geophysics*, **57(1)**, 15-26.
- Wu, Z. and Alkhalifah, T., 2015, Simultaneous inversion of the background velocity and the perturbation in full-waveform inversion, *Geophysics*, **80(6)**, R317-R329.
- Wu, R.-S. and Toksöz, M. N., 1987, Diffraction tomography and multisource holography applied to seismic imaging, *Geophysics*, **52(1)**, 11-25.
- Xu, S., Wang, D., Chen, F., Lambare, G. and Zhang, Y., 2012, Inversion on reflected seismic wave, 82th Annual International Meeting, SEG, Expanded Abstracts.
- Zhong, Y. and Liu, Y., 2019, Source-independent time-domain vector-acoustic full-waveform inversion, *Geophysics*, **84(4)**, R489-R505.

Appendix A. Derivation of gradient in FWI

The second-order acoustic wave equation with pressure source is written as:

$$\frac{1}{\rho v_p^2} \frac{\partial^2 P(\mathbf{x}, t)}{\partial t^2} = \nabla \cdot \left(\frac{1}{\rho} \nabla P(\mathbf{x}, t) \right) + f_p$$

$$\begin{cases} P(\mathbf{x}, 0) = 0 \\ \left. \frac{\partial P(\mathbf{x}, t)}{\partial t} \right|_{t=0} = 0 \\ \lim_{\mathbf{x} \rightarrow \infty} P(\mathbf{x}, t) = 0 \end{cases}, \quad (\text{A-1})$$

where f_p represents the pressure source and additional equations represent the initial and radiation boundary conditions. Then, add an additional term to least-squares norm objective function as:

$$E_{L2} = \frac{1}{2} \iint [P_u(\mathbf{x}, t) - P_d(\mathbf{x}, t)] \sum_{j=1}^{nr} \delta(\mathbf{x} - \mathbf{x}_j) dV dt$$

$$- \iint q(\mathbf{x}, t) \left(\frac{1}{\rho v_p^2} \frac{\partial^2 P_u(\mathbf{x}, t)}{\partial t^2} - \nabla \cdot \left(\frac{1}{\rho} \nabla P_u(\mathbf{x}, t) \right) - f_p \right) dV dt. \quad (\text{A-2})$$

Because the second term at the right-hand-side of eq. (A-2) is always zero for any wavefield q , the objective function is exactly the same as that of eq. (10). Then, each part of the second term is rearranged using the integration by parts and Gauss divergence theorem as follows:

$$\begin{aligned}
& \iint q(\mathbf{x},t) \left(\frac{1}{\rho v_p^2} \frac{\partial^2 P_u(\mathbf{x},t)}{\partial t^2} \right) dV dt \\
&= \int \left\{ q(\mathbf{x},t) \frac{1}{\rho v_p^2} \frac{\partial P_u(\mathbf{x},t)}{\partial t} \Big|_0^T - \int \frac{\partial q(\mathbf{x},t)}{\partial t} \frac{1}{\rho v_p^2} \frac{\partial P_u(\mathbf{x},t)}{\partial t} dt \right\} dV \\
&= \int - \left\{ \frac{\partial q(\mathbf{x},t)}{\partial t} \frac{1}{\rho v_p^2} \frac{\partial P_u(\mathbf{x},t)}{\partial t} \Big|_0^T + \int \frac{\partial^2 q(\mathbf{x},t)}{\partial t^2} \frac{1}{\rho v_p^2} P_u(\mathbf{x},t) dt \right\} dV \\
&= \iint \frac{\partial^2 q(\mathbf{x},t)}{\partial t^2} \frac{1}{\rho v_p^2} P_u(\mathbf{x},t) dV dt
\end{aligned} \tag{A-3}$$

is satisfied if a termination condition for q is applied as follows:

$$\begin{cases} q(\mathbf{x},T) = 0 \\ \left. \frac{\partial q(\mathbf{x},t)}{\partial t} \right|_{t=T} = 0 \end{cases} , \tag{A-4}$$

where T is the total recording time. Moreover,

$$\begin{aligned}
& \iint q(\mathbf{x},t) \nabla \cdot \left(\frac{1}{\rho} \nabla P_u(\mathbf{x},t) \right) dV dt \\
&= \iint \nabla \cdot \left(q(\mathbf{x},t) \frac{1}{\rho} \nabla P_u(\mathbf{x},t) \right) - \nabla q(\mathbf{x},t) \frac{1}{\rho} \nabla P_u(\mathbf{x},t) dV dt , \tag{A-5} \\
&= \iint -\nabla q(\mathbf{x},t) \frac{1}{\rho} \nabla P_u(\mathbf{x},t) dV dt
\end{aligned}$$

by imposing the radiation boundary condition as:

$$\lim_{x \rightarrow \infty} q(\mathbf{x},t) = 0 . \tag{A-6}$$

Therefore, eq. (A-2) is rearranged as:

$$\begin{aligned}
E_{L2} = & \frac{1}{2} \iint [P_u(\mathbf{x}, t) - P_d(\mathbf{x}, t)] \sum_{j=1}^{nr} \delta(\mathbf{x} - \mathbf{x}_j) dV dt \\
& - \iint \left(P_u(\mathbf{x}, t) \frac{1}{\rho v_p^2} \frac{\partial^2 q(\mathbf{x}, t)}{\partial t^2} \right) dV dt \quad . \quad (A-7) \\
& - \iint \left(\nabla q(\mathbf{x}, t) \cdot \left(\frac{1}{\rho} \nabla P_u(\mathbf{x}, t) \right) \right) dV dt + \iint f_p q(\mathbf{x}, t) dV dt
\end{aligned}$$

Eq. (A-7) is then rearranged by taking the variance operator as follows:

$$\begin{aligned}
\delta E_{L2} = & \iint \delta P_u(\mathbf{x}, t) [P_u(\mathbf{x}, t) - P_d(\mathbf{x}, t)] \sum_{j=1}^{nr} \delta(\mathbf{x} - \mathbf{x}_j) dV dt \\
& - \iint \delta P_u(\mathbf{x}, t) \frac{1}{\rho v_p^2} \frac{\partial^2 q(\mathbf{x}, t)}{\partial t^2} dV dt \\
& + \iint \delta P_u(\mathbf{x}, t) \nabla \cdot \left(\frac{1}{\rho} \nabla q(\mathbf{x}, t) \right) dV dt \quad . (A-8) \\
& + \iint \delta \rho \left(P_u(\mathbf{x}, t) \frac{1}{\rho^2 v_p^2} \frac{\partial^2 q(\mathbf{x}, t)}{\partial t^2} + \left(\frac{1}{\rho^2} \nabla q(\mathbf{x}, t) \cdot \nabla P_u(\mathbf{x}, t) \right) \right) dV dt \\
& + \iint \delta v_p \left(P_u(\mathbf{x}, t) \frac{2}{\rho v_p^3} \frac{\partial^2 q(\mathbf{x}, t)}{\partial t^2} \right) dV dt
\end{aligned}$$

The adjoint-wavefield is then defined as:

$$\lambda(\mathbf{x}, t) = q(\mathbf{x}, T - t) \quad . \quad (A-9)$$

In conclusion, if the adjoint wavefield satisfies the following relation:

$$\begin{aligned}
& \frac{1}{\rho v_p^2} \frac{\partial^2 \lambda(\mathbf{x}, t)}{\partial t^2} - \nabla \cdot \left(\frac{1}{\rho} \nabla \lambda(\mathbf{x}, t) \right) \\
& = [P_u(\mathbf{x}, T - t) - P_d(\mathbf{x}, T - t)] \sum_{j=1}^{nr} \delta(\mathbf{x} - \mathbf{x}_j) \quad , \quad (A-10) \\
& \left\{ \begin{array}{l} \lambda(\mathbf{x}, 0) = 0 \\ \frac{\partial \lambda(\mathbf{x}, t)}{\partial t} \Big|_{t=0} = 0 \\ \lim_{\mathbf{x} \rightarrow \infty} \lambda(\mathbf{x}, t) = 0 \end{array} \right.
\end{aligned}$$

the partial derivative of objective function with respect to each model parameter (ρ or v_p) is written as:

$$\begin{aligned} \frac{\partial E_{L2}}{\partial \rho} = & \iint P_u(\mathbf{x}, t) \frac{1}{\rho^2 v_p^2} \frac{\partial^2 \lambda(\mathbf{x}, T-t)}{\partial t^2} dV dt, \\ & + \iint \frac{1}{\rho^2} \nabla \lambda(\mathbf{x}, T-t) \cdot \nabla P_u(\mathbf{x}, t) dV dt \end{aligned} \quad (\text{A-11})$$

$$\frac{\partial E_{L2}}{\partial v_p} = \iint P_u(\mathbf{x}, t) \frac{2}{\rho v_p^3} \frac{\partial^2 \lambda(\mathbf{x}, T-t)}{\partial t^2} dV dt, \quad (\text{A-12})$$

because the terms $\frac{\partial P_u(\mathbf{x}, t)}{\partial \rho}$ and $\frac{\partial P_u(\mathbf{x}, t)}{\partial v_p}$ are ignored. By comparing the eq.

(A-12) with eq. (12), it is noticed that the partial derivative of modeling operator

corresponds to the term $\frac{2}{\rho v_p^3} \frac{\partial^2}{\partial t^2}$ and $\frac{1}{\rho^2 v_p^2} \frac{\partial^2}{\partial t^2} + \frac{1}{\rho^2} \nabla \cdot \nabla$ for velocity and

density parameters, respectively. Also, because $\iint P_u(\mathbf{x}, t) \lambda(\mathbf{x}, T-t) dV dt$ is the convolution of wavefields in the time domain, gradients are calculated in time-frequency-domain FWI just by multiplying the extracted frequency components of wavefields.

Appendix B. Conjugate-gradient method

The conjugate direction method is a technique to iteratively solve a large linear problem, such as:

$$\mathbf{Ax} = \mathbf{b} \quad . \quad (\text{B-1})$$

The key idea of this method is to construct a pair of vectors in \mathbf{A} -conjugate relation, because these vectors are linearly independent (Nocedal and Wright, 1999). \mathbf{A} -conjugate set of vectors (\mathbf{p}_i) are defined as:

$$\mathbf{p}_l^T \mathbf{A} \mathbf{p}_m = 0 \quad \text{if } l \neq m \quad . \quad (\text{B-2})$$

Due to this linearly independent characteristic of vectors in \mathbf{A} -conjugate relation, for the n-dimensional matrix \mathbf{A} , at most n iterations are needed to obtain the solution of this linear system. Conjugate gradient (CG) method is a modified version of the conjugate direction method and determines the \mathbf{A} -conjugate pair of vectors as follows:

$$\begin{aligned} \mathbf{r}_0 &= \mathbf{b} - \mathbf{A}x_0 = \mathbf{p}_0 \\ \mathbf{x}_k &= \mathbf{x}_{k-1} + \alpha_{k-1} \mathbf{p}_{k-1} \\ \alpha_{k-1} &= \frac{\mathbf{p}_{k-1}^T \mathbf{r}_{k-1}}{\mathbf{p}_{k-1}^T \mathbf{A} \mathbf{p}_{k-1}} \quad , \\ \mathbf{r}_k &= \mathbf{b} - \mathbf{A} \mathbf{x}_k \\ \mathbf{p}_k &= \mathbf{r}_k + \beta_k \mathbf{p}_{k-1} \\ \beta_k &= -\frac{\mathbf{p}_{k-1}^T \mathbf{A} \mathbf{r}_k}{\mathbf{p}_{k-1}^T \mathbf{A} \mathbf{p}_{k-1}} \end{aligned} \quad (\text{B-3})$$

where \mathbf{x}_k is the solution of current iteration; \mathbf{r}_k is referred to as the residue vector. Then, it is noticed that

$$\begin{aligned}
\mathbf{p}_k^T \mathbf{A} \mathbf{p}_{k-1} &= (\mathbf{r}_k + \beta_k \mathbf{p}_{k-1})^T \mathbf{A} \mathbf{p}_{k-1} \\
&= \mathbf{r}_k^T \mathbf{A} \mathbf{p}_{k-1} - \left(\frac{\mathbf{p}_{k-1}^T \mathbf{A} \mathbf{r}_k}{\mathbf{p}_{k-1}^T \mathbf{A} \mathbf{p}_{k-1}} \right)^T \mathbf{p}_{k-1}^T \mathbf{A} \mathbf{p}_{k-1} = 0, \quad (\text{B-4})
\end{aligned}$$

meaning that current and previous \mathbf{p} vectors are in \mathbf{A} -conjugate relation. Also, for \mathbf{p}_k and \mathbf{p}_{k-2} ,

$$\begin{aligned}
\mathbf{p}_k^T \mathbf{A} \mathbf{p}_{k-2} &= (\mathbf{r}_k + \beta_k \mathbf{p}_{k-1})^T \mathbf{A} \mathbf{p}_{k-2} \\
&= (\mathbf{r}_{k-1} - \alpha_{k-1} \mathbf{A} \mathbf{p}_{k-1} + \beta_k \mathbf{p}_{k-1})^T \mathbf{A} \mathbf{p}_{k-2} \\
&= \mathbf{r}_{k-1}^T \mathbf{A} \mathbf{p}_{k-2} - (\alpha_{k-1} \mathbf{A} \mathbf{p}_{k-1})^T \mathbf{A} \mathbf{p}_{k-2} + \beta_k \mathbf{p}_{k-1}^T \mathbf{A} \mathbf{p}_{k-2} \quad . \quad (\text{B-5}) \\
&= \mathbf{r}_{k-1}^T \mathbf{A} \mathbf{p}_{k-2} - \left(\frac{\mathbf{p}_{k-1}^T \mathbf{r}_{k-1}}{\mathbf{p}_{k-1}^T \mathbf{A} \mathbf{p}_{k-1}} \mathbf{A} \mathbf{p}_{k-1} \right)^T \mathbf{A} \mathbf{p}_{k-2} \\
&= 0
\end{aligned}$$

This \mathbf{A} -conjugate relation can be expanded to \mathbf{p}_0 , meaning that all \mathbf{p} vectors are naturally in \mathbf{A} -conjugate relations and become linearly independent to each other.

However, for extremely large linear problem, such as FWI, the matrix \mathbf{A} is not available during the calculation of step-length (α) and combination coefficient (β). Accordingly, to avoid the usage of matrix \mathbf{A} during the step-length calculation, line search method is employed as explained in chapter 2.4. Also, several methods have been proposed to calculate β without using the matrix \mathbf{A} as:

$$\beta_k = - \frac{(\mathbf{r}_k - \mathbf{r}_{k-1})^T \mathbf{r}_k}{(\mathbf{r}_k - \mathbf{r}_{k-1})^T \mathbf{r}_{k-1}} \quad (\text{Hestenes and Stiefel, 1952}), \quad (\text{B-6})$$

$$\beta_k = - \frac{(\mathbf{r}_k)^T \mathbf{r}_k}{(\mathbf{r}_{k-1})^T \mathbf{r}_{k-1}} \quad (\text{Fletcher and Reeves, 1964}), \quad (\text{B-7})$$

$$\beta_k = -\frac{(\mathbf{r}_k - \mathbf{r}_{k-1})^T \mathbf{r}_k}{(\mathbf{r}_{k-1})^T \mathbf{r}_{k-1}} \quad (\text{Polak and Ribiere, 1969}) . \quad (\text{B-8})$$

Following Nocedal and Wright (1999), for nonlinear optimization problem, the coefficient calculated following the study of Polak and Ribiere (1969) seems to be the most robust and efficient, compared to the others.

To accelerate the convergence of CG method, preconditioner matrix that reduces the number of distinct eigenvalues of original linear system in eq. (B-1) is used. This is because the total number of iterations required to solve the linear system is related to the number of eigenvalues of matrix \mathbf{A} . Here, the preconditioner matrix is denoted as $\mathbf{M} = \mathbf{C}\mathbf{C}^T$ and then, the linear system of equation is rewritten as:

$$(\mathbf{C}^T \mathbf{A} \mathbf{C})(\mathbf{C}^{-1} \mathbf{x}) = \tilde{\mathbf{A}} \tilde{\mathbf{x}} = \tilde{\mathbf{b}} = \mathbf{C}^T \mathbf{b} . \quad (\text{B-9})$$

For this rearranged linear system, the CG method is implemented as follows:

$$\begin{aligned} \tilde{\mathbf{r}}_0 &= \tilde{\mathbf{b}} - \tilde{\mathbf{A}} \tilde{\mathbf{x}}_0 = \tilde{\mathbf{p}}_0 \\ \tilde{\mathbf{x}}_k &= \tilde{\mathbf{x}}_{k-1} + \alpha_{k-1} \tilde{\mathbf{p}}_{k-1} \\ \tilde{\mathbf{r}}_k &= \tilde{\mathbf{b}} - \tilde{\mathbf{A}} \tilde{\mathbf{x}}_k \quad , \\ \tilde{\mathbf{p}}_k &= \tilde{\mathbf{r}}_k + \beta_k \tilde{\mathbf{p}}_{k-1} \\ \beta_k &= -\frac{\left(\tilde{\mathbf{r}}_k - \tilde{\mathbf{r}}_{k-1} \right)^T \tilde{\mathbf{r}}_k}{\left(\tilde{\mathbf{r}}_{k-1} \right)^T \tilde{\mathbf{r}}_{k-1}} \end{aligned} \quad (\text{B-10})$$

and rearranged with respect to the original solution \mathbf{x} as:

$$\begin{aligned}
\mathbf{p}_0 &= \mathbf{M}\mathbf{r}_0 \\
\mathbf{x}_k &= \mathbf{x}_{k-1} + \alpha_{k-1}\mathbf{p}_{k-1} \\
\mathbf{p}_k &= \mathbf{M}\mathbf{r}_k + \beta_k\mathbf{p}_{k-1} \quad , \\
\beta_k &= -\frac{(\mathbf{M}\mathbf{r}_k - \mathbf{M}\mathbf{r}_{k-1})^T \mathbf{r}_k}{(\mathbf{M}\mathbf{r}_{k-1})^T \mathbf{r}_{k-1}}
\end{aligned}
\tag{B-11}$$

due to the following relationships:

$$\begin{aligned}
\tilde{\mathbf{r}}_k &= \mathbf{C}^T \mathbf{r}_k \\
\tilde{\mathbf{x}}_k &= \mathbf{C}^{-1} \mathbf{x}_k \quad . \\
\tilde{\mathbf{p}}_k &= \mathbf{C}\mathbf{p}_k
\end{aligned}
\tag{B-12}$$

Note that in case of $\mathbf{M}=\mathbf{I}$, the PCG method is the same as the CG method and in case of $\mathbf{M}=\mathbf{A}^{-1}$, the linear system is solved with a single iteration due to a single eigenvalue of $\mathbf{M}\mathbf{A}=\mathbf{I}$.

Appendix C. Seismic reciprocity theorem

The seismic reciprocity theorem is easily demonstrated with the second-order acoustic wave equation that is represented in the frequency domain as:

$$-\frac{\omega^2}{K} \tilde{P}(\mathbf{x}, \omega; \mathbf{x}_s) - \nabla \cdot \frac{1}{\rho} \nabla \tilde{P}(\mathbf{x}, \omega; \mathbf{x}_{src}) = \tilde{f}_p \delta(\mathbf{x} - \mathbf{x}_s) \quad , \quad (\text{C-1})$$

where $K = \rho v_p^2$ is the bulk modulus and \mathbf{x}_s represents the source location vector. Following Ikelle and Amundsen (2005), two different states denoted as A and B are assumed, whose pressure wavefields are obtained from each source location and model parameter vectors. Then, for a domain D whose surface boundary is denoted as ∂D , the surface integral of $\tilde{P}^A \frac{1}{\rho^B} \nabla \tilde{P}^B - \tilde{P}^B \frac{1}{\rho^A} \nabla \tilde{P}^A$

is changed as follows by applying the Gauss theorem:

$$\begin{aligned} & \int_{\partial D} dS \mathbf{n} \cdot \left(\tilde{P}^A \frac{1}{\rho^B} \nabla \tilde{P}^B - \tilde{P}^B \frac{1}{\rho^A} \nabla \tilde{P}^A \right) \\ &= \int_D \left(\nabla \tilde{P}^A \cdot \frac{1}{\rho^B} \nabla \tilde{P}^B - \nabla \tilde{P}^B \cdot \frac{1}{\rho^A} \nabla \tilde{P}^A \right) dV \quad , \quad (\text{C-2}) \\ &+ \int_D \left(\tilde{P}^A \nabla \left(\frac{1}{\rho^B} \nabla \tilde{P}^B \right) - \tilde{P}^B \nabla \left(\frac{1}{\rho^A} \nabla \tilde{P}^A \right) \right) dV \end{aligned}$$

where the vector \mathbf{n} denotes the normal vector to the surface ∂D . With the radiation boundary condition, the surface integral at the left-hand side of the Eq.

(C-2) vanishes. Following eq. (C-1), the term $\nabla \left(\frac{1}{\rho} \nabla \tilde{P} \right)$ is replaced into

$\tilde{f}_p \delta(\mathbf{x} - \mathbf{x}_s) - \frac{\omega^2}{K} \tilde{P}$ and the integration over the domain D is rearranged as:

$$\begin{aligned}
0 = & \int_D \left(\frac{1}{\rho^B} - \frac{1}{\rho^A} \right) \nabla \tilde{P}^A \cdot \nabla \tilde{P}^B dV + \int_D \left(\frac{\omega^2}{K^A} - \frac{\omega^2}{K^B} \right) \tilde{P}^A \tilde{P}^B dV \\
& + \int_D \tilde{P}^A \tilde{f}_p^B \delta(\mathbf{x} - \mathbf{x}^B) dV - \int_D \tilde{P}^B \tilde{f}_p^A \delta(\mathbf{x} - \mathbf{x}^A) dV
\end{aligned} \quad . \quad (\text{C-3})$$

Therefore, if the wave propagates through the same media with the same source signature, then the first and second terms at the right-hand side of eq. (C-3) vanish and following equation is derived:

$$\tilde{P}(\mathbf{x}^B, \omega; \mathbf{x}^A) = \tilde{P}(\mathbf{x}^A, \omega; \mathbf{x}^B) \quad . \quad (\text{C-4})$$

Eq. (C-4) means that the pressure wavefield generated at the location of \mathbf{x}^A and recorded at the location of \mathbf{x}^B is the same as the pressure wavefield generated at the location of \mathbf{x}^B and recorded at the location of \mathbf{x}^A .

Appendix D. Local wavenumber of model update

The wavenumber of calculated gradients is derived to investigate the maximum spatial resolution of FWI. Following the derivation of gradients in Appendix A, it is noticed that the local gradients are calculated from the zero-lag cross-correlation of source and receiver wavefields. For plane waves of a single angular frequency (ω) the local wavenumber vector is written as:

$$\mathbf{k} = \omega \mathbf{s} \quad , \quad (\text{D-1})$$

where \mathbf{s} is the slowness vector. In a geometry as shown in Fig. D-1, the slowness vector at the perturbation point (\mathbf{s}_n) is the sum of source (\mathbf{s}_s) and receiver (\mathbf{s}_r) slowness vectors. Then, each slowness vector is written as:

$$\mathbf{s}_s = \left(-\frac{\cos(\phi_s)}{v}, -\frac{\sin(\phi_s)}{v} \right) \quad , \quad (\text{D-2})$$

$$\mathbf{s}_r = \left(-\frac{\cos(\phi_r)}{v}, -\frac{\sin(\phi_r)}{v} \right) \quad , \quad (\text{D-3})$$

$$\begin{aligned} \mathbf{s}_n &= \left(-\frac{\cos(\phi_s)}{v} - \frac{\cos(\phi_r)}{v}, -\frac{\sin(\phi_s)}{v} - \frac{\sin(\phi_r)}{v} \right) \\ &= \frac{2}{v} \left(-\cos\left(\frac{\phi_s + \phi_r}{2}\right) \cos\left(\frac{\phi_s - \phi_r}{2}\right), -\sin\left(\frac{\phi_s + \phi_r}{2}\right) \cos\left(\frac{\phi_s - \phi_r}{2}\right) \right) \quad , (\text{D-4}) \end{aligned}$$

where v is the velocity of the perturbation point. Assuming the unit directional vector of \mathbf{s}_n as \mathbf{n} ;

$$\mathbf{s}_n = \frac{2}{v} \cos\left(\frac{\phi_s - \phi_r}{2}\right) \mathbf{n} \quad , \quad (\text{D-5})$$

where $\phi_s - \phi_r$ is an opening angle between the source and receiver wavefields.

Following eqs. (D-1) and (D-5), the maximum spatial resolution obtained from FWI is half the local wavelength when the aperture angle becomes zero. Additionally, it is noticed that the wavelength of model update is closely related to the frequency of wavefields and the opening angle between the source and receiver wavefields. To reconstruct long-wavelength features of the model, smaller frequency and larger opening angle are needed.

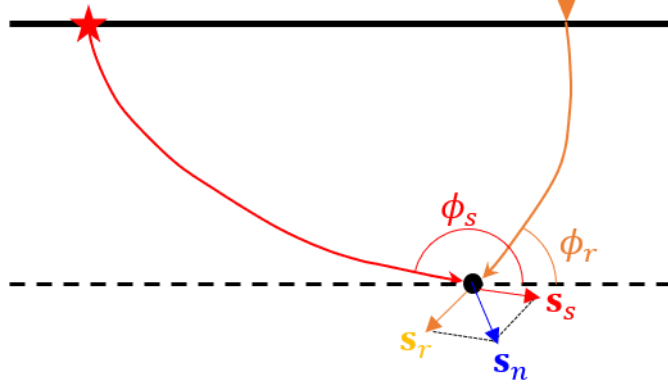


Fig. D-1. Schematic diagram showing the geometry of source and receiver wavefields: The red arrows are related to the source wavefields and the orange arrows are related to the receiver wavefields; the blue arrow shows the slowness vector of the gradient.

Appendix E. Utilization of pseudo-Ax data in pressure-based FWI

The acoustic wave equation represented in eqs. (1) and (2) can be rewritten in the frequency domain with respect to pressure wavefields as:

$$\left(-\frac{\omega^2}{\rho v_p^2} - \nabla \cdot \frac{1}{\rho} \nabla \right) \tilde{P}(\mathbf{x}, \omega) = \tilde{f}_p, \quad (\text{E-1})$$

and with respect to particle acceleration wavefields as:

$$\left(-\omega^2 - \frac{1}{\rho} \nabla \rho v_p^2 \nabla \cdot \right) \tilde{\mathbf{a}}(\mathbf{x}, \omega) = \tilde{\mathbf{f}}_a, \quad (\text{E-2})$$

where $\tilde{\mathbf{a}} = \begin{pmatrix} \tilde{a}_x \\ \tilde{a}_z \end{pmatrix}$ and tilde notation indicates wavefields in the frequency domain. These equations are then represented in matrix form as follows:

$$\mathbf{S}_p \mathbf{u}_p = \mathbf{f}_p, \quad (\text{E-3})$$

$$\mathbf{S}_a \mathbf{u}_a = \mathbf{f}_a, \quad (\text{E-4})$$

where \mathbf{S}_p and \mathbf{S}_a are the modeling operator matrices representing the left-hand side of eqs. (E-1) and (E-2), respectively; \mathbf{f} is the source function vector and \mathbf{u} is the modeled wavefield vector defined at the whole nodal points.

Following the equation of motion in eq. (2), the pressure and particle acceleration wavefields have a linear relationship, which is written as:

$$\mathbf{D} \mathbf{u}_p = \mathbf{u}_a, \quad (\text{E-5})$$

where \mathbf{D} represents the divergence operator with density parameter whose

dimension is $2N \times N$; N is the total number of nodal points. Objective functions can be defined based on either the pressure wavefields or particle acceleration wavefields and the gradients due to the perturbation at k^{th} model parameter are respectively written as:

$$\nabla_{m_k} E = \sum_{\omega} \sum_{src} \sum_{rec} \left(\frac{\partial \mathbf{u}_p}{\partial m_k} \right)^T (\mathbf{u}_p - \mathbf{d}_p)^* , \quad (\text{E-6})$$

$$\nabla_{m_k} E = \sum_{\omega} \sum_{src} \sum_{rec} \left(\frac{\partial \mathbf{u}_a}{\partial m_k} \right)^T (\mathbf{u}_a - \mathbf{d}_a)^* , \quad (\text{E-7})$$

where \mathbf{d} is the observed wavefields. From eq. (E-5),

$$\mathbf{u}_p = (\mathbf{D}^T \mathbf{D})^{-1} \mathbf{D}^T \mathbf{u}_a , \quad (\text{E-8})$$

$$\mathbf{S}_p (\mathbf{D}^T \mathbf{D})^{-1} \mathbf{D}^T \mathbf{u}_a = \mathbf{f}_p . \quad (\text{E-9})$$

Taking the partial derivative with respect to the velocity parameter, following equation is obtained:

$$\frac{\partial \mathbf{u}_a}{\partial m_k} = \left(\mathbf{S}_p (\mathbf{D}^T \mathbf{D})^{-1} \mathbf{D}^T \right)^{-1} \left(-\frac{\partial \mathbf{S}_p}{\partial m_k} (\mathbf{D}^T \mathbf{D})^{-1} \mathbf{D}^T \mathbf{u}_a \right) , \quad (\text{E-10})$$

and eq. (E-7) is rearranged as:

$$\begin{aligned} \nabla_{m_k} E &= \sum_{\omega} \sum_{src} \sum_{rec} \left(\left(\mathbf{S}_p (\mathbf{D}^T \mathbf{D})^{-1} \mathbf{D}^T \right)^{-1} \left(-\frac{\partial \mathbf{S}_p}{\partial m_k} (\mathbf{D}^T \mathbf{D})^{-1} \mathbf{D}^T \mathbf{u}_a \right) \right)^T (\mathbf{u}_a - \mathbf{d}_a)^* \\ &= \sum_{\omega} \sum_{src} \sum_{rec} \left(\left(\mathbf{S}_p \right)^{-1} \left(-\frac{\partial \mathbf{S}_p}{\partial m_k} \mathbf{u}_p \right) \right)^T (\mathbf{D}^T \mathbf{D}) (\mathbf{u}_p - \mathbf{d}_p)^* \quad .(\text{E-11}) \\ &= \sum_{\omega} \sum_{src} \sum_{rec} \left(\frac{\partial \mathbf{u}_p}{\partial m_k} \right)^T (\mathbf{D}^T \mathbf{D}) (\mathbf{u}_p - \mathbf{d}_p)^* \end{aligned}$$

Eq. (E-11) means that the FWI with particle acceleration wavefields can be

conducted just by changing the pressure data residuals. Additionally, when the objective function is defined with only the horizontal particle acceleration data (as the case of pseudo-Ax data inversion), $\mathbf{D}^T \mathbf{D}$ indicates the second-order horizontal differentiation. Therefore, the pseudo-Ax data inversion is implemented along with pressure-based algorithm, just by taking $\partial^2/\partial x^2$ to pressure data residuals.

초 록

해저면 공통 수신기 모음의 압력 수평 차분을 활용한 음향파형역산 전략

황 종 하

에너지시스템공학부

서울대학교 대학원

완전파형역산(full waveform inversion)은 지하 지질구조를 규명하는데 가장 효과적인 탄성파탐사 자료처리기법 중 하나이다. 완전파형역산은 탐사자료와 모델링자료를 맞추는 국부 최적화 문제를 반복적으로 풀어냄으로써 지하의 물성모델을 정량적으로 구축할 수 있다. 최근에는 탄화수소 저류층을 찾는 데 완전파형역산이 활용된다. 그러나 아직도 파형역산에 있어 비선형성 문제와 과도한 계산량과 같은 해결되어야 할 과제들이 있다.

이 논문에서는 관측된 유사 수평입자가속도 공통 수신기 모음(Common-receiver gather) 자료를 송신원-수진기의 위치가 뒤바뀐 환경에서의 공통 송신원 모음 자료와 맞추는 음향파 완전파형역산 전략을 제시한다. 기존의 공통 송신원 모음 기반 파형역산에서는 매 반복수마다 송신원 개수 두 배에 해당되는 횡수의 순차모델링이 필요하지만, 제시된 공통 수신기 모음

기반 파형역산에서는 수진기 개수의 두 배에 해당되는 횡수의 순차모델링이 필요하다. 이에 따라 송신원의 개수가 수진기의 개수에 비해 상당히 많은 해저면 탐사자료에 있어 파형역산의 계산비용을 획기적으로 줄일 수 있다. 또한, 좁은 벌림(offset)에서 PP와 PS 반사파가 압력 및 수평입자가속도 자료보다 약한 진폭으로 나타나는 유사 수평입자가속도 자료를 역산에 활용함으로써 장파장속도구조를 우세하게 구축할 수 있으며 이를 통해 파형역산이 갖는 비선형성 문제를 완화할 수 있다.

제시된 파형역산 전략을 합성자료 및 북해 Volve 유전에서의 현장자료에 대해 적용해 보았으며, 이 시험을 통해 제시된 공통 수진기 모음 이용 전략이 유사한 역산 결과를 적은 계산량으로 얻을 수 있다는 것을, 또 압력 자료를 이용하는 경우보다 유사 수평입자가속도 자료를 파형역산에 이용하는 것이 속도모델의 단파장 구조의 구축을 제한하여 의미있는 지하 P파 속도모델에 수렴할 수 있다는 것을 보였다.

주요어: 완전파형역산, 음향파, 해저면 탄성파, 공통-수진기모음, 수평 입자가속도

학번: 2016-21314